LAWRENCE
LIVERMORE
NATIONAL
LABORATORY

LLNL-TR-468271

FY10 Engineering Innovations, Research and Technology Report

M. A. Lane, S. M. Aceves, C. N. Paulson, J. V. Candy, C. V. Bennett, K. Carlisle, D. C. Chen, D. A. White, J. V. Bernier, M. A. Puso, T. H. Weisgraber, B. Corey, J. I. Lin, E. K. Wheeler, A. M. Conway, J. D. Kuntz, C. M. Spadaccini, D. A. Dehlinger, J. Kotovsky, R. Nikolic, R. P. Mariella, A. M. K. Foudray, V. Tang, B. L. Guidry, B. M. Ng, T. D. Lemmond, B. Y. Chen, C. A. Meyers, T. L. Houck

January 31, 2011

Disclaimer

This work performed under the auspices of the U.S. Department of Energy by Lawrence Livermore National Laboratory under Contract DE-AC52-07NA27344.

FY10

Engineering Innovations, Research & Technology Report

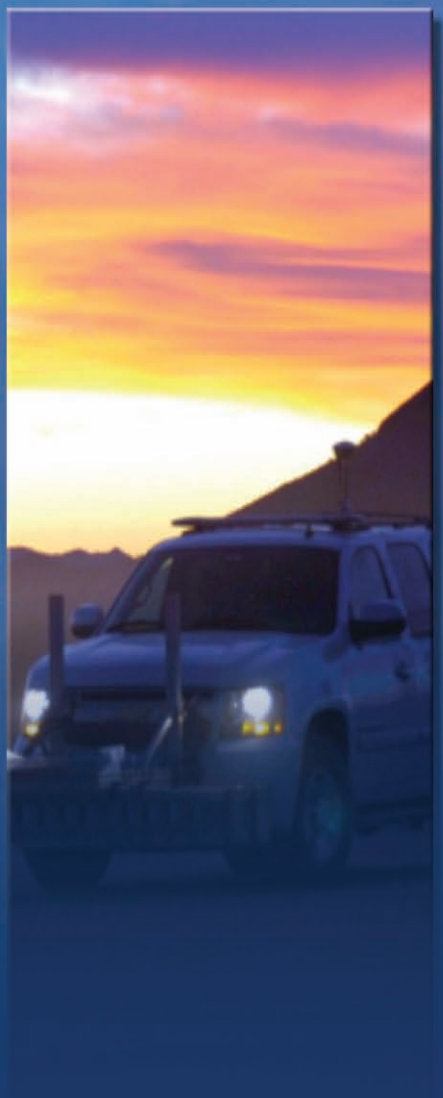

April 2011

Lawrence Livermore National Laboratory

LLNL-TR-468271

Acknowledgments

Scientific Editors
Don McNichols
Camille Minichino

Graphic Designers
Jeffrey B. Bonivert
Lucy C. Dobson
Debbie A. Ortega
Kathy J. Seibert

FY10

Engineering Innovations, Research & Technology Report

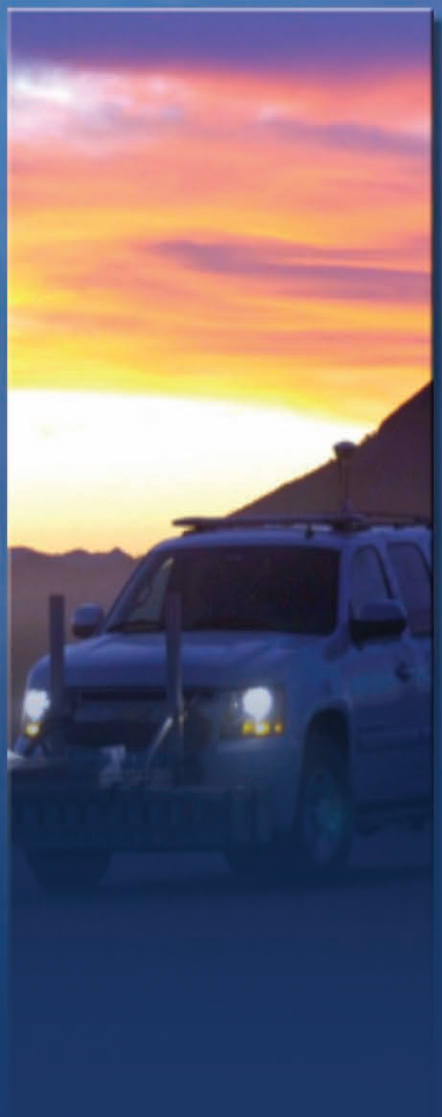

April 2011

Lawrence Livermore National Laboratory

LLNL-TR-468271

A Message From

Monya A. Lane
Associate Director for Engineering

This report summarizes key research, development, and technology advancements in Lawrence Livermore National Laboratory's Engineering Directorate for FY2010. These efforts exemplify Engineering's nearly 60-year history of developing and applying the technology innovations needed for the Laboratory's national security missions, and embody Engineering's mission to "Enable program success today and ensure the Laboratory's vitality tomorrow."

Leading off the report is a section featuring compelling engineering innovations. These innovations range from advanced hydrogen storage that enables clean vehicles, to new nuclear material detection technologies, to a landmine detection system using ultra-wideband ground-penetrating radar. Many have been recognized with R&D Magazine's prestigious R&D 100 Award; all are examples of the forward-looking application of innovative engineering to pressing national problems and challenging customer requirements.

Engineering's capability development strategy includes both fundamental research and technology development. Engineering research creates the competencies of the future where discovery-class groundwork is required. Our technology development (or reduction to practice) efforts enable many of the research breakthroughs across the Laboratory to translate from the world of basic research to the national security missions of the Laboratory. This portfolio approach produces new and advanced technological capabilities, and is a unique component of the value proposition of the Lawrence Livermore Laboratory. The balance of the report highlights this work in research and technology, organized into thematic technical areas: Computational Engineering; Micro/Nano-Devices and Structures; Measurement Technologies; Engineering Systems for Knowledge Discovery; and Energy Manipulation. Our investments in these areas serve not only known programmatic requirements of today and tomorrow, but also anticipate the breakthrough engineering innovations that will be needed in the future.

Computational Engineering

Computational Engineering efforts focus on the research, development, and deployment of computational engineering technologies that provide the foundational capabilities to address most facets of Engineering's mission, ranging from fundamental advances to enable accurate modeling of full-scale DOE and DoD systems performing at their limits, to advances for treating photonic and micro-fluidic systems.

FY2010 research projects encompassed *in situ* observations of twinning and phase transformations at the crystal scale; work on developing a new Lagrange embedded mesh technique for multiphysics simulations; and adding improvements to our existing lattice-Boltzmann polymer code to enable fully turbulent, multiscale simulations of drag reduction. Technology projects included maintaining and adding new capabilities to vital engineering simulation tools such as DYNA3D and NIKE3D.

Micro/Nano-Devices & Structures

Micro/Nano-Scale Manufacturing encompasses technology efforts that fuel the commercial growth of microelectronics and sensors, while simultaneously customizing these technologies for unique, noncommercial applications that are mission-specific to the Laboratory and DOE. The Laboratory's R&D talent and unique fabrication facilities have enabled highly innovative and custom solutions to technology needs in Stockpile Stewardship, Homeland Security, and Intelligence.

FY2010 research projects included characterizing phenomena of DNA microarray hybridization, regeneration, and selective release; improving the performance of cadmium–zinc–telluride gamma radiation detectors; creating transparent ceramic optics with unique properties based on tailored nanostructures; and advancing 3-D micro- and nanofabrication using Projection Micro-Stereolithography (PμSL). Technology projects included introducing a process to fabricate polydimethylsiloxane (PDMS) multilayer soft lithography chips; developing read-out electronics for our pillar thermal neutron detector; and using acoustic focusing in a microfluidic device to separate white blood cells from whole blood.

Measurement Technologies

Measurement Technologies comprise activities in nondestructive characterization, metrology, sensor systems, and ultrafast technologies for advanced diagnostics. The advances in this area are essential for the future experimental needs in Inertial Confinement Fusion, High-Energy-Density Physics, Weapons, and Department of Homeland Security programs.

FY2010 research featured advanced Bayesian model-based statistical processing algorithms for illicit radionuclide detection; and optimized, volumetric scanning for x-ray array sources for nondestructive evaluation. Technology projects included feasibility studies for using low-energy, fast-pulsed, power-driven dense plasma focus for experiments; applying our Statistical Radiation Detection System (SRaDS) processing to data collected from NaI detectors; and establishing a flexible testbed for 95-GHz impulse imaging radar.

Engineering Systems for Knowledge & Inference

Knowledge Discovery encompasses a wide variety of technologies with the goal to broadly generate new understanding or knowledge of relevant situations, thereby allowing anticipation or prediction of possible outcomes. With this understanding, a more comprehensive solution may be possible for problems as complex as the prediction of disease outbreaks or advance warning of terrorist threats.

FY2010 research efforts were centered on better understanding of higher-adaptive systems, especially in adversarial relationships; event extraction from text using error-driven aggregation methodologies; and developing new, dynamic classifier algorithms for detecting problems with unequal and evolving error costs. Technology efforts included improvements to an entity extractor aggregation system, and improving optimization capabilities for electric grid energy modeling by using high-performance computing.

Energy Manipulation

Energy Manipulation encompasses the fundamental understanding and technology deployment for many modern pulsed-power applications. This area has broad applications for magnetic flux compression generators, components for modern accelerators, and high-performance apparatus for high-energy-density physics experiments.

FY2010 research focused on developing a computer model of electrical breakdown at the dielectric/vacuum interface, leading to a computational methodology for designing high-voltage vacuum insulators for pulsed-power devices.

Contents

Introduction

Engineering Innovations

Computational Engineering

Micro/Nano-Devices and Structures

Measurement Technologies

Engineering Systems for Knowledge and Inference

Energy Manipulation

Engineering Innovations

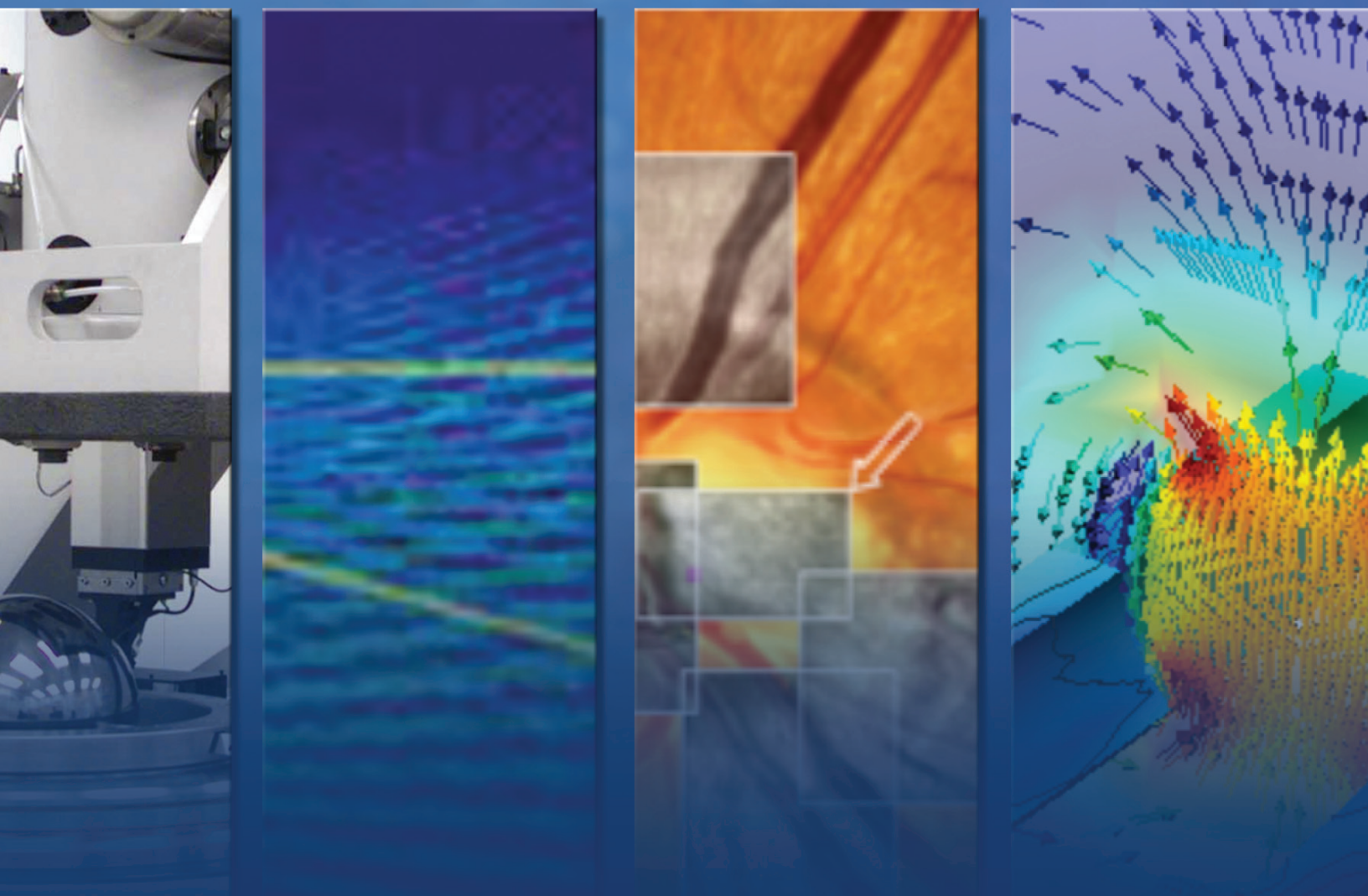

Advanced Fuel Storage for Tomorrow's Clean Hydrogen Vehicles

Insulated cryogenic fuel tanks could be used in mass-produced, hydrogen-powered vehicles.

For more information contact:

Salvador M. Aceves
(925) 422-0864
aceves6@llnl.gov

The U.S. transportation sector is almost 100 percent dependent on fossil fuels, and the results of that dependency are evident all around us, from the effects of global warming to rising prices at the gas pump. Hydrogen (H_2) is a leading candidate to supplant petroleum as a universal transportation fuel. It has the highest combustion energy by weight of any fuel. Burning 1 kilogram of hydrogen produces 2.6 times more energy than 1 kilogram of gasoline. Additionally, hydrogen can be generated from water and any energy source, and has the potential to ultimately eliminate petroleum dependence, associated air pollutants, and greenhouse gases. When burning hydrogen, vehicles generate zero greenhouse gases and only small amounts of nitrogen oxides. Water vapor is the only emission.

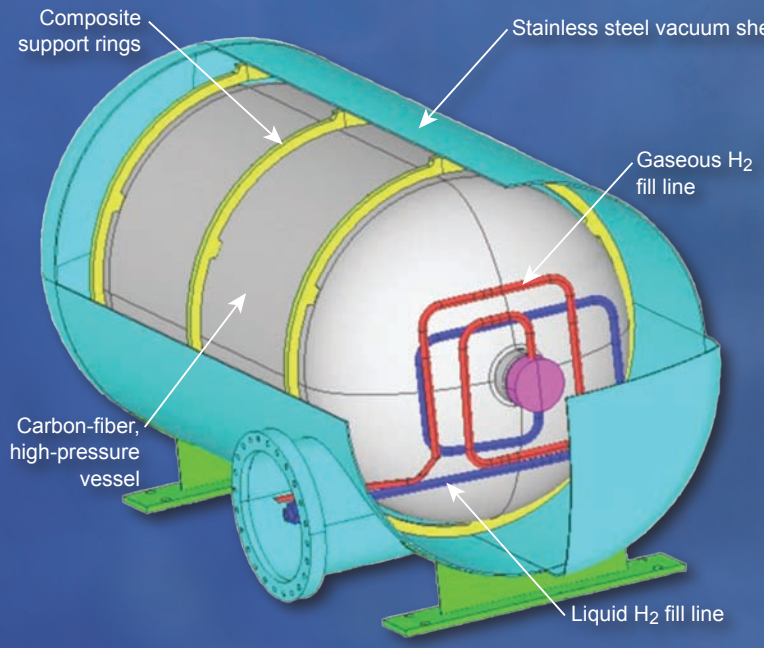

Figure 1. Design of cryogenic pressure vessel installed in a Prius hydrogen hybrid vehicle. The inner vessel is an aluminum-wound, carbon fiber-wrapped pressure vessel typically used for storage of compressed gases. This vessel is surrounded by a vacuum space filled with numerous sheets of highly reflective plastic (minimizing heat transfer into the vessel), and an outer jacket of stainless steel. The outer tank measures 47 inches long with an outer diameter of 23 inches.

Limitations of Current Hydrogen Storage Systems

Despite hydrogen's stellar fuel efficiency, it is difficult to store compressed hydrogen in the large quantities needed to provide the driving range achieved by gasoline- and diesel-powered vehicles. Most prototype hydrogen vehicles use compressed hydrogen stored at room temperature and high pressure (35 to 70 megapascals, or 350 to 700 atmospheres). The energy density of compressed hydrogen at 35 megapascals is only about one-twelfth that of gasoline. As a result, hydrogen cars must use large, high-pressure tanks, which are often located in the trunk. Thus, the predominant technical barrier limiting widespread use of hydrogen automobiles is storing enough hydrogen fuel onboard to achieve an acceptable driving range (500+ kilometers) in a compact, lightweight, rapidly refuelable, and cost-effective system. Current hydrogen storage systems present fundamental limitations:

- Low-pressure liquid hydrogen storage systems have high density and reasonably low cost, however a major drawback is the significant electricity required to liquefy the hydrogen (about equal to 30 percent of the heating value of the hydrogen molecule). In addition, liquid hydrogen is extremely sensitive to

Figure 2. Technicians Vern Switzer and Tim Ross prepare to fuel the hydrogen-powered test car with liquid hydrogen for the first time.

heat; it expands significantly when warmed only a few degrees. As a result, vehicles that use low-pressure tanks are usually not filled to maximum capacity and must have a system to release some of the hydrogen vapor that accumulates in the tank when the car is not driven for several days. Evaporative losses after longer periods of inactivity (1–2 weeks) can leave the driver without fuel.

- Compressed hydrogen gas is bulky and difficult to package within a vehicle. The large storage vessels necessary to achieve a 500-km (300-mile) range are expensive because of the amount of material needed for current carbon-fiber tanks. Additionally, the size of such tanks limits the passenger and cargo capacity of the vehicles in which they are installed.
- Storage systems based on metal hydrides and sorbents can be heavy and may suffer from slow refueling (about 15 minutes, considerably longer than the approximately 3 minutes required to refuel a gasoline vehicle).

Advantages of a Cryogenic System

Over the last decade, LLNL has pioneered an approach that combines existing storage technologies to capture the advantages of both cryogenic and high-pressure storage: cryogenic high-pressure vessels. The team had earlier focused on liquid hydrogen (–253 °C) because it does not require a high-pressure tank, and it takes up one-third the volume of compressed hydrogen at room temperature. Like all gases, compressed hydrogen can be stored more compactly at colder temperatures. Pressurized hydrogen at 35 megapascals becomes twice as dense when cooled from ambient temperature to –150 °C. Cooling it further to –210 °C (close to the temperature of liquid nitrogen) triples the energy density. Cooling hydrogen also lowers the hydrogen expansion energy during a sudden tank rupture, potentially mitigating the consequences of vessel failure.

The cryogenic pressure vessel developed by the LLNL team comprises a high-pressure inner vessel made of carbon-fiber-coated aluminum similar to those used for storage of compressed gas, a vacuum space filled with numerous sheets of highly reflective plastic (for high-performance thermal insulation), and an outer jacket of stainless steel (see Figure 1). The vacuum minimizes the conduction of heat between the outer steel jacket and the inner pressure vessel, which would cause liquid hydrogen to evaporate quickly. In addition, the multiple layers of reflective material almost eliminate heat transfer from radiation, much like a Thermos bottle. The outer steel jacket has cutouts for thermocouples and sensors to measure pressure, temperature, and the fuel level within the inner vessel. In addition, the system is equipped with two safety devices to prevent catastrophic failure in case of overpressure.

For a pressure vessel of given size and cost, a cryogenic vessel stores substantially more hydrogen than a vessel at ambient temperature, doing so without the additional weight and cost of hydrogen-absorbent materials but with far greater thermal endurance than conventional (*i.e.*, low-pressure) cryogenic liquid H_2 tanks. Cryogenic pressure vessels present key advantages:

- High density, superior to liquid hydrogen vessels, but with reduced evaporative losses. A driver will have a limited reserve and range regardless of evaporative losses as compared to liquid hydrogen vessels.
- More compact, and therefore smaller and less expensive, than compressed hydrogen systems.
- Light weight and capable of fast refueling—about 3 minutes (see Figure 2).

Figure 3. The cryogenic pressure vessel installed onboard a Toyota Prius hydrogen hybrid vehicle, which set a world record for the longest distance driven on one tank of hydrogen fuel.

Record-Setting Technology

The LLNL group put their cryogenic tank design to the test in 2007 and set a world record for the longest distance driven on one tank of hydrogen fuel, albeit at reduced speeds and utilizing the trunk for storage space. The group drove a Toyota Prius hybrid vehicle, modified to run on hydrogen, 1050 kilometers (653 miles) on one tank of liquid hydrogen (150 liters, or almost 40 gallons). The overall fuel economy was about 105 kilometers per kilogram of hydrogen—equivalent to about 65 miles per gallon of gasoline—when driven at 40 to 56 kilometers (25 to 35 miles) per hour (see Figure 3).

A subsequent cryogenic pressure vessel design uses LLNL proprietary technology to shrink the insulation thickness considerably (to about 1.5 cm versus about 3 cm in the previous design) while still maintaining adequate dormancy (see Figure 4). The resulting cryogenic pressure vessel is the most compact automotive hydrogen storage vessel ever built, and is the only system that meets DOE's very challenging 2015 targets for weight and volume performance at higher storage capacities (10 kg versus 5 kg).

Hydrogen Vehicles in Our Future?

Although cryogenic pressure vessels demonstrate superior performance for storing hydrogen, LLNL researchers envision further potential for lighter, more compact, and lower-cost designs. In collaboration with automobile manufacturer BMW and a major pressure vessel manufacturer (SCI), LLNL continues to advance the technology toward near-term demonstration and commercialization.

The Livermore team is playing an important role in making possible both clean and sustainable transportation fueled by the simplest element in the universe.

Figure 4. The latest cryogenic pressure vessel prototype (right) is 23% more compact than the previous (left), a feat achieved through reduced insulation thickness (1.5 cm versus 3 cm). This reduction in external volume suffices for meeting the very challenging 2015 DOE weight and volume targets.

Landmine Detection Using Ultrawideband Ground-Penetrating Radar Technology

Advances in several technology areas could soon yield a ruggedized, fieldable system for safely detecting buried explosive devices.

For more information contact:

Christine N. Paulson
(925) 423-7362
paulson4@llnl.gov

Decades after armed conflicts end, hidden landmines continue to maim and kill thousands of innocent civilians. Today, minefields plague 79 countries, and most of these nations have limited resources to remove them. Metal detectors and manual prodding of soil remain amongst the most reliable and trusted demining techniques. As a result, humanitarian mine detection efforts are time-consuming, costly, and dangerous.

Figure 1. Three examples of antipersonnel landmines. These mines commonly use the pressure of a person's foot as a trigger, but tripwires also are frequently employed. Often, mines can be set to detonate if someone attempts to lift, shift, or disarm them.

Detecting buried landmines and improvised explosive devices (IEDs) also presents a daunting challenge for U.S. forces, a challenge that remains inadequately addressed by today's technology. Buried roadbed and roadside bombs continue to pose a significant threat to U.S. forces in the Afghan and Iraqi theaters. Route clearance patrols often must rely on their sense of intuition and familiarity with the terrain to detect surface abnormalities that may indicate a potential buried or concealed threat.

Whether it be cleaning up the explosive remnants of previous wars or protecting our in-theater troops from surprise attack, better tools are needed to detect and identify buried explosive threats. To address this technology gap, LLNL is developing ultrawideband (UWB) impulse radar (iRadar) platforms that are combined with sophisticated subsurface image reconstruction algorithms.

A Lasting, Widespread, and Insidious Threat

Landmines are explosive devices placed in the ground and triggered by mechanical or electronic proximity sensors (Figure 1). After conflicts cease, unexploded landmines can remain intact for decades, killing and maiming civilians, impeding reconstruction efforts, and rendering agricultural lands useless. The *Landmine Monitor Report 2008* assesses that many thousands of square kilometers of land are contaminated by up to 100 million mines and other explosives. In 2007, about 1400 people were killed and 4000 injured by mines or other explosive remnants of war.

An estimated 100,000 mines are removed each year. At that rate, clearing 40 to 50 million mines would require

450 to 500 years, assuming no new mines are laid. However, the pace of mine removal is far slower than the rate at which new mines are being placed. Current demining methods are decades old and are extremely tedious because metal detectors cannot discriminate metallic mines from innocuous metallic clutter. Some antipersonnel mines are mostly plastic except for small metal parts. Detecting these metal parts requires turning up the metal detector's sensitivity. As a result, most "mines" turn out to be harmless objects such as bottle caps, bullet casings, nails, or tin cans. Demining teams typically uncover 100 to 1000 innocuous metal objects for each mine found.

Figure 2. The Landmine Detection Advanced Radar Concept showed the feasibility of discriminating buried landmines from innocuous clutter.

In 2009, the Joint Improvised Explosive Device Defeat Organization (JIEDDO) sponsored a large, multiyear effort at LLNL to develop a route-clearance, vehicle-mounted IED detection system capable of detecting buried IEDs in real time. In the JIEDDO project, LLNL is transitioning the archetype ultrawideband iRadar technology into an integrated, rugged, and automated system ready for forward operational assessment. In collaboration with two industrial partners, we have developed a landmine locator system, which in 2009 was recognized with an R&D 100 Award.

Evolution of iRadar

For more than a decade, Livermore researchers have been working on applying their patented ultrawideband technology to the worldwide problem of demining. In 1993, LLNL invented the micropower impulse radar (MIR), a technology that could be leveraged to build low-cost, low-power, and compact radar devices based on advances in transient digitizing circuits needed for LLNL laser programs. Two years later, LLNL began two separate multiyear efforts to develop ground-penetrating radar (GPR) systems using ultrawideband radar technology: the High-performance Electromagnetic Roadway Mapping and Evaluation System (HERMES), designed to identify structural deterioration in bridge decks, and the Landmine Detection Advanced Radar Concept (LANDMARC) funded by the Department of Defense. These efforts helped to accelerate MIR development to where it is today.

The LANDMARC system was developed as a small array system mounted on a cart, as shown in Figure 2. This portable system collected data at a

Figure 3. The landmine locator employed a high-speed, multistatic array of 16 iRadar elements.

slower rate than the truck-mounted HERMES array but was capable of collecting data at much higher resolution. Traditional GPR systems face difficulties detecting mines buried at or near the surface of the ground. This is because the strong radar reflection from the surface, combined with stray reflections from innocuous surface clutter, tends to obscure the return signal from the hidden landmine. One of the key innovations in using micropower impulse radar for this application was the ability to remove the effects of surface reflections through time-gating and better discrimination of rocks, roots, voids, and other subsurface clutter from mines.

While both efforts yielded promising results, the prototype UWB GPR technology was not yet ready for operational use. One of the most significant hurdles was that collected data had to be processed offline, due to limitations on data acquisition speed, data storage capacity, and processing speed. HERMES and LANDMARC data were captured and stored on hard drives for post-processing, which could take several hours to produce a result and required human adjustment of model parameters to match the dielectric conditions and thicknesses of subsurface soil layers.

Over the next several years, subsequent developments in other related technology projects significantly improved LLNL core capabilities in the area of ultrawideband radar imaging. These developments included a super-resolution imaging technique, advanced time reversal reconstruction algorithms, model-based tomography schemes, a self-contained digital synthetic aperture radar imaging system that enabled electronic beam-forming and beam-steering of the UWB signal, and advances in parallel computation technology to create a dedicated real-time image reconstruction circuit. This series of technology projects enabled LLNL to advance the ultrawideband radar imaging capability from a monostatic array with post-processing, to a digitally controlled, multistatic array with real-time image reconstruction processing. This ability attracted several externally funded efforts, which further advanced the GPR effort.

Today's iRadar GPR Technology

In 2008, First Alliance Technologies, LLC, entered into a cooperative research and development agreement (CRADA) with LLNL to develop an iRadar landmine detection system designed for deployment on an aerial platform. To achieve rapid ground coverage, sufficient resolution, and superior imaging quality, a 16-element linear multistatic array was developed, as shown in Figure 3. This technology formed the initial technological basis of what would later become the JIEDDO vehicle-mounted iRadar IED detection platform.

The 2010 JIEDDO system, whose precursor is shown in Figure 4, consists of a ruggedized multistatic iRadar array with military standard (MIL-SPEC) components and sophisticated positioning sensors. The JIEDDO project had similar imaging requirements to previous

efforts and could leverage existing hardware technology, but unlike previous efforts its results needed to be calculated and presented to the operator in real-time. Computation of iRadar image reconstruction and detection algorithms are performed on the vehicle platform, and automated detection results are displayed to the user in real-time. The system is currently being readied for an operational assessment.

The iRadar sensor is compact, low power, inexpensive, and unusually versatile. The sensor can send out extremely short electromagnetic pulses over an exceptionally wide range of frequencies, permitting much finer resolution of materials than other sensing systems. The JIEDDO system represents the pinnacle of many years of LLNL array and imaging research and will likely serve as an important stepping-stone for the systems that will follow.

Opportunities for Future Development

There are opportunities to further improve the iRadar GPR capability in several areas, including radar hardware, antenna design, the use of optimal transmit waveform shapes, electromagnetic modeling, and algorithms.

- Immediate benefits could be achieved by using existing engineering capabilities to transition time-reversal analysis, migration imaging with refraction correction, and model-based layer estimation algorithms into real-time tools that can be deployed during data collection.
- Through the use of an arbitrary waveform generator system, studies on custom pulse shapes could be evaluated for their utility in the GPR application.
- Development of multiple frequency band systems could improve resolution and dynamic range.
- For route clearance applications, further research and development in automated change detection will help to better identify alterations in the environment and identify innocuous clutter objects, thereby reducing the false alarm rate.
- Enhanced sensor fusion using thermal or radiation detectors could enhance surface anomaly detection.
- The development of an optimal iRadar antenna for GPR applications could improve iRadar sensitivity, robustness, and form factor.

Once the landmine locator is in use, the world will at last have a safer method to detect mines. As a result, nations will be able to confidently reclaim millions of square kilometers from this long-lasting scourge of war.

Figure 4. An early prototype of the JIEDDO vehicle-mounted IED detection platform scans for buried targets in a desert environment.

Fast Detection of Illicit Radioactive Materials to Prevent Nuclear Terrorism

SRaDS provides a fast and reliable radionuclide detection and identification capability that can dramatically enhance the utility of existing detection systems.

For more information contact:

James V. Candy
(925) 422-8675
candy1@llnl.gov

Each year, some 48 million cargo containers move among the world's transportation portals with more than 16 million containers arriving in the U.S. by ship, truck, and rail. Illicit radioactive materials could be hidden in any one of these cargo-filled containers. Yet, physically searching every container would bring shipping to a halt. Improving security at U.S. transportation portals is thus one of the nation's most difficult technical and practical challenges because the systems developed for screening cargo must operate in real time without disrupting legitimate commercial shipping activities.

Working at this intersection of commerce and national security, a team of Livermore scientists and engineers led by principal investigator James Candy applied its expertise in radiation science and gamma detection to develop the statistical radiation detection system (SRaDS), an innovative software solution that nonexperts can use to rapidly and reliably detect radionuclides (Figure 1). The team, along with ICx® Technologies, Inc., in Arlington, Virginia, has won an R&D 100 Award for the technology. According to Candy, who derived early support from Livermore's Laboratory Directed Research and Development Program, "the team cross-fertilized the areas of statistical signal processing with radiation transport physics, enabling a unique and breakthrough solution to a long-troubling problem, especially in today's climate of terrorist threats."

Figure 1. The statistical radiation detection system (SRaDS) is an innovative software solution that can be integrated easily into any gamma-detection system to combat illicit trafficking of radioactive material through customs, border crossings, and limited-access areas. SRaDS identifies radionuclides in low-count situations when measurement time is short and demand for reliability is high. The processed data are displayed in intuitive plots showing results that a nontechnical user can interpret.

Rapid and Reliable Radionuclide Detection

Identifying radioactive material in a moving target is a difficult problem primarily because of the very low counts of gamma-ray signals that occur during the short time interval available for detection. In low-count situations such as these, conventional spectrometry techniques do not have enough time to collect the number of photons required to calculate the pulse-height spectra (PHS) that identify radioactive materials. For example, a vehicle moving through a gamma-detection system at a transportation portal is screened for less than 10 seconds. Accurate radionuclide detection is even more difficult when radioactive material is shielded by lead, packaging, or adjacent cargo.

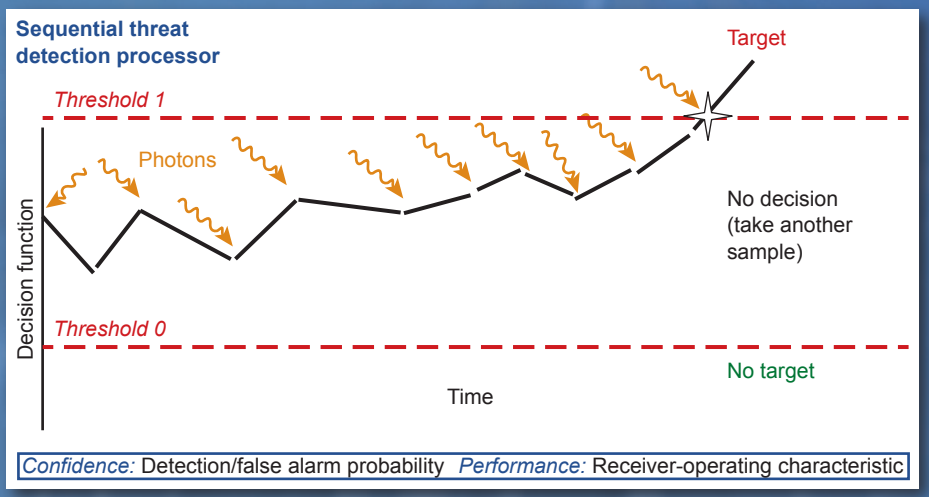

Figure 2. The graph shows a conceptual implementation of the sequential Bayesian radionuclide detection technique. As each individual photon is extracted, it is discriminated, estimated, and the decision function calculated and compared to thresholds to "decide" if the targeted radionuclide is present or not. Quantitative performance and sequential thresholds are determined from estimated receiver-operating characteristic (ROC) curves and the selected operating point (detection/false alarm probability).

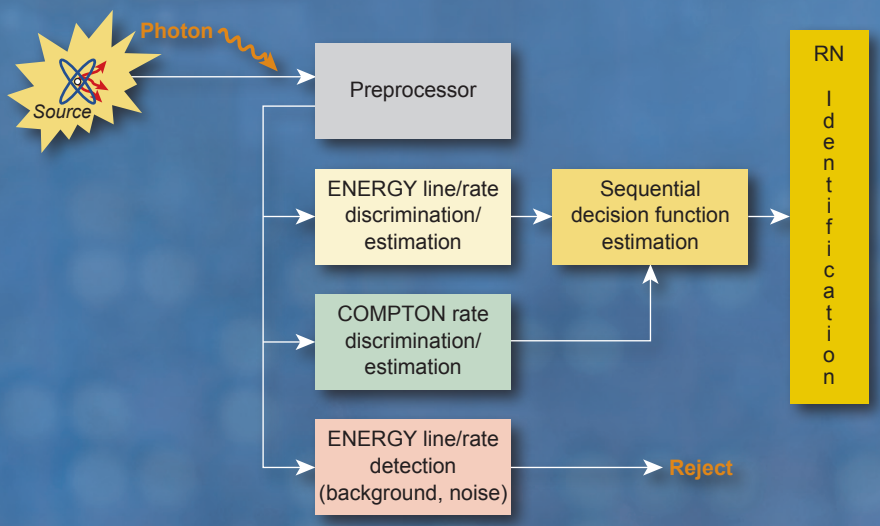

Figure 3. The basic SRaDS design paradigm, showing discrimination of both photoelectrons and downscatter (Compton) photons and estimation of the targeted radionuclide, which provides parameters for the sequential decision function leading to radionuclide identification. Background and extraneous photons are rejected.

SRaDS speeds up identification by automatically rejecting extraneous and nontargeted photons during the process. Exploiting Bayesian algorithms, the smart processor examines each photon—one by one—as it arrives and then "decides" whether a detected radionuclide is present based on selected parameters. This capability is not available in conventional detection systems, yet it is essential in the successful identification of radionuclides in low-count situations when measurement time is short and demand for reliability is high.

A Closer Look

The generic sequential detection technique is depicted conceptually in Figure 2, illustrating each photon arrival along with the corresponding decision function and thresholds. At each arrival the decision function is sequentially updated and compared to thresholds to perform the detection, photon-by-photon. The thresholds are selected from a receiver-operating characteristic (ROC) curve (detection versus false-alarm probability) for each individual radionuclide decision function. An operating point is selected from the ROC that corresponds to specific desired probabilities specifying the required thresholds that are calculated for each radionuclide.

Instead of accumulating a PHS or energy histogram as is usually done in current detection systems, each photon is processed individually upon arrival and then discarded. The structure of this processor is shown in Figure 3. After a photon is preprocessed by the acquisition system, the energy and arrival time measurements are passed to the energy/rate discriminators to determine the photon's status (accepted or rejected). If accepted, the parameter estimates are sequentially updated and provided as input to update the decision function for detection and eventual identification. If rejected, the photon is discarded. Detection is declared when such a decision is statistically justified based on estimated detection and false alarm probabilities specified by the ROC curve obtained during calibration. The result is a system that has improved

detection performance with high reliability and short decision times.

Each unique energy/arrival component of the target radionuclide is processed individually in a separate channel, resulting in the parallel/distributed processor structure. After the photon is acquired, the distributed processor

- discriminates the individual monoenergetic (single-energy) arrival identifying one of the parallel channels;
- discriminates the corresponding detection rate (interarrival) parameter for that particular channel;
- enhances the channel energy and rate (interarrival) parameters;
- updates the corresponding decision function; and
- detects/identifies the target radionuclide by thresholding the decision function.

As diagrammed in Figure 4, the SRaDS processor consists of a discriminator for both energy (amplitude) and rate (interarrival time). If the photon does not pass this test, it is sent to the Compton (downscatter) processor or rejected (photoelectron only). If accepted, it is processed further to improve the estimates of its energy, rate, and emission probability and then used to update the decision function.

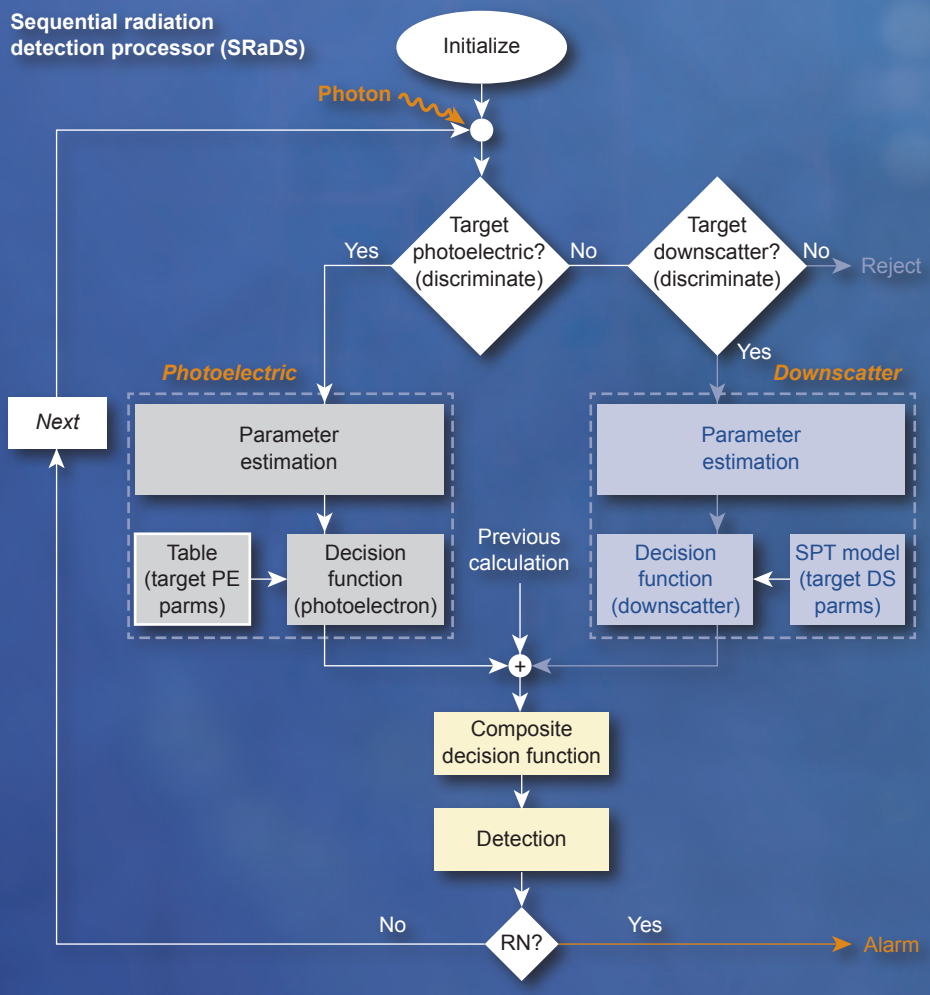

Figure 4. The statistical Bayesian design is shown (simply) as a photon-by-photon processor enhancing the raw detector measurement while rejecting instrumentation noise and estimating the photoelectrons and downscatter photons through energy/rate discrimination and parameter estimation. This information is input to a function used to detect which of the target radionuclides are present.

Results of this photon-by-photon processor with downscatter are shown in Figure 5. In this three-column figure, the first column is the composite PHS (which is not used). The second column shows the measured photon energies (arrivals) as red dots. Circles (green) represent the discriminator output photoelectrons, and squares (purple) represent the discriminated downscatter photons. Notice that these align with the PHS column's energy "lines." The third column shows the decision function for each of the targeted radionuclides. As each photon is processed, the decision function is sequentially updated until one of the thresholds, target or nontarget, is crossed (indicated by solid red boxes in the figure), declaring a threat or nonthreat.

When a cargo container arrives at an SRaDS detector, the decision function in the software is refreshed, updated, and refined based on the energies and arrival times of the accepted photons. Detection is declared only when statistically justified according to the three factors—the Bayesian algorithms, the updated decision function, and the conditions defined by the specific ROC curve obtained during initial calibration. In contrast, conventional techniques require manually setting a specific counting time in advance with the hope that the data acquired can justify the decision. By encompassing the statistical nature of radiation transport physics and sequential Bayesian processing techniques, SRaDS provides highly developed quantitative statistical analysis of the data received in real time.

What's more, basic and advanced processor options are available with SRaDS. Both processor options provide complete statistical analysis of radionuclide data obtained from any type of gamma detector. The basic and advanced processors gather information from unscattered photons that deposit full photon energy. The advanced processor also gathers information from Compton-scattered photons that exhibit

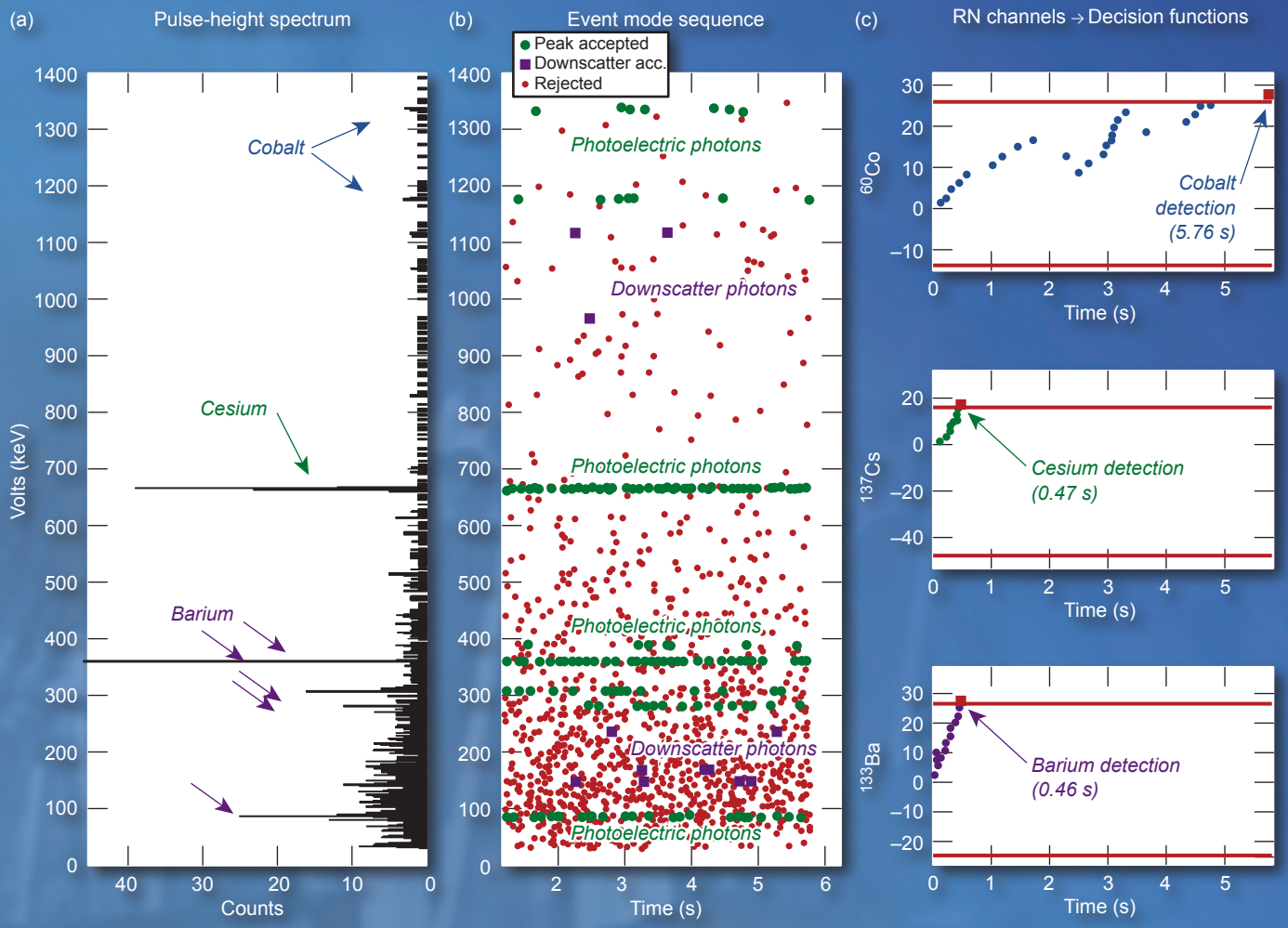

Figure 5. Results of sequential Bayesian detection and identification. (a) Pulse-height spectrum (after calibration). (b) Photon arrivals (red) with targeted photoelectron discrimination (green circles) and downscatter photons (purple squares). (c) Decision functions for ^{60}Co (detection time: 5.76 s), ^{137}Cs (detection time: 0.47 s) and ^{133}Ba (detection time: 0.46 s) with thresholds for radionuclide detection/identification.

diminished energy—a major breakthrough in time-domain, low-count detection technology.

Integrates into Any Gamma-Detector System

The Livermore team took special care to ensure that SRaDS can easily be integrated into any gamma-detection system, including large stationary detectors at transportation portals that help search for radioactive contraband material in moving vehicles, cargo containers, and railroad cars. SRaDS works equally well in pedestrian monitors used to combat illicit trafficking of radioactive material through customs, border crossings, and limited-access areas. The technology can also be installed in portable gamma detectors used by first responders to determine radiation risks associated with local nuclear emergencies. The algorithms are easily embedded in programmable gate arrays that users in the field can adjust to a location's specifications and detection requirements.

Depending on the hardware setup, the processed data can be graphically displayed on a computer monitor or portable unit. While conventional gamma-detection systems require a highly trained practitioner to analyze the results, refine the data, and guide the interpretation procedure, SRaDS displays data in intuitive plots, showing results that a nontechnical user can interpret. Alternatively, SRaDS can be configured to simply provide audio and visual alerts indicating the presence of targeted radionuclides at user-selected confidence levels. Users can also select false-alarm probabilities to reduce or eliminate the occurrence of false positives depending on the level of detection required for a given situation. SRaDS is a comprehensive software system that combines outstanding radionuclide-detection performance with high reliability and a short acquisition time. The system can be implemented easily in existing infrastructure to protect the nation from the insidious threat of illicit radioactive materials.

Capturing Waveforms in a Quadrillionth of a Second

The FemtoScope time microscope provides dramatic improvments in instruments' resolution and dynamic range.

For more information contact:

Corey V. Bennett
(925) 422-9394
bennett27@llnl.gov

HOW will scientists "see" what happens inside the National Ignition Facility (NIF), the world's largest laser, when it creates the extreme temperature and pressure conditions found in stars? Instruments such as oscilloscopes and streak cameras cannot capture all the details of fast-moving, complex events such as fusion burn. Their dynamic range (the ratio between the smallest and largest possible values) and their temporal resolution (the precision of a measurement with respect to time) are coupled. As a result, these conventional instruments lose dynamic range with faster temporal resolution or lose temporal resolution with more dynamic range.

To meet the emerging need for greater dynamic range and temporal resolution, scientists can turn to the new FemtoScope—a "time microscope" that is attached to the front end of a conventional recording instrument to dramatically improve its performance. Livermore researchers (see Figure 1), in collaboration with colleagues from Stanford University, the University of Southampton, and the University of California at Davis, won an R&D 100 Award for their invention of the FemtoScope. Initial efforts for this work were funded by Livermore's Laboratory Directed Research and the Engineering Directorate's Technology Development Program for single-shot,

Figure 1. Livermore development team for the FemtoScope (from left): Bryan Moran, Vincent Hernandez, Alex Drobshoff, and Corey Bennett.

high-dynamic-range applications. The Defense Advanced Research Projects Agency (DARPA) then funded development for advanced light detection and ranging (LIDAR) applications where high repetition rate frames containing sub-picosecond detail each needed to be recorded in a single shot. Today, with support from Livermore's Weapons and Complex Integration (WCI) organization, this time lens technology is again being applied to single-event, high-dynamic-range diagnostic applications on NIF.

Slowing Down the Signal

The FemtoScope (Figure 2) improves the performance of an oscilloscope or streak camera much in the same way that a high-performance lens improves a camera's output. It is not a recording instrument in itself. Rather, it dramatically enhances the performance of any conventional recording instrument to which it is connected by ultrafast processing of waveforms. The FemtoScope improves the dynamic range of these instruments and their time resolution from tens of picoseconds (trillionths of a second) to hundreds of femtoseconds (quadrillionths of a second).

"The temporal imaging technology on which the FemtoScope is based is fundamentally a time-scale transformation tool that can be configured to magnify, compress, reverse, and even Fourier-transform ultrafast waveforms," says Livermore scientist Corey Bennett. "We have concentrated our past efforts on developing a time-magnification system." Just as a scanning electron microscope's powers of magnification can reveal nanometer-size details of an object's structure not viewable with an ordinary light microscope, so the FemtoScope's powers of time magnification can reveal the peaks and valleys in a 1-picosecond signal not detectable by a standalone oscilloscope or streak camera.

Figure 2. FemtoScope equipment.

In the past, other instruments have obtained very high resolution by conducting repetitive waveform sampling and averaging with ultrashort time intervals. However, because NIF will be fired a maximum of four times a day, diagnostics must operate in a single-shot mode, and repetitive sampling approaches are not an option.

By slowing down or "magnifying" the time scale of the signal before it enters the recording instrument, the FemtoScope allows the capture of signals that otherwise would be too fast to record in any detail. This process not only improves the resolution of the recording system but also increases

the available dynamic range at a given speed. In Figure 3, a simulation shows how three optical pulses separated by 6 picoseconds (first to last) can be "time magnified" so that they occur over 18 picoseconds at the output.

The FemtoScope uses a single-shot process in real time to capture each window of time (or frame) of interest and stretches out the waveform so that greater detail is revealed. Furthermore, this process can be repeated at a rate of more than 100 million frames per second to record the real-time evolution of a signal. With ultrafast resolution and nearly endless recording length, this instrument can uncover waveform data with peaks and valleys never before detectable.

When combined with a 20-GHz real-time oscilloscope, the FemtoScope produces an instrument capable of recording 850-GHz waveforms in 100-picosecond frames at 155 million frames per second until its memory is full. When combined with an optical streak camera, the FemtoScope produces an instrument with a 20-times increase in temporal resolution and a 30-times increase in dynamic range, resulting in an overall improvement of 600 times compared with the performance of the streak camera alone. The same time-lens technology can also be configured to Fourier-transform an input waveform. This produces an output spectrum that looks like the input temporal profile and which can be recorded in a single shot with a conventional imaging spectrometer.

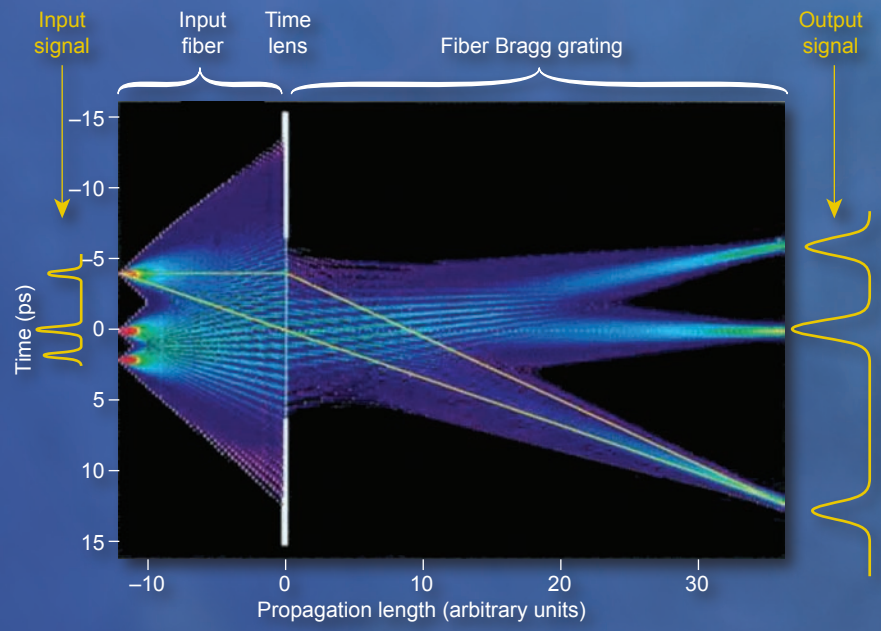

Figure 3. A false-color image shows three pulses propagating through a temporal imaging system with a magnification of three times. Color here represents intensity or brightness, with red being the brightest. The simulation shows how three optical pulses occurring in a 6-picosecond time frame can be "time magnified" so that, at the output, they occur over 18 picoseconds. The angle of propagation in this figure also represents the path of a particular color of light relative to the carrier frequency. The time lens not only magnifies waveforms in time but it can be used to Fourier-transform the waveform, converting the temporal profile to a scaled spectral profile.

Emerging Needs

The FemtoScope represents a fundamental paradigm shift in high-speed imaging technology. As researchers improve their understanding of physical phenomena, they will need to examine processes on shorter and shorter time scales. The FemtoScope will be an invaluable tool for collecting detailed dynamic data at faster temporal resolution.

The Laboratory plans to use the FemtoScope on NIF experiments, which will need diagnostics with time resolutions on the scale of 1 picosecond or less to determine when high-energy photons first appear and what happens from their first appearance to their peak production. The FemtoScope will also be useful for detecting and recording a broad range of signal strengths—from very weak signal intensities to very strong.

The time-lens technology is fundamentally an optical signal manipulation tool. NIF has applications in which the fundamental measurement desired is that of an x-ray signal. We have been developing picosecond-resolution x-ray sensors, which are fundamentally optical modulators driven by the x-ray signal being recorded. A continuous wave or long pulse optical probe is reflected off these sensors with its amplitude modulated by the incident x-ray flux, thereby performing an x-ray-to-optical conversion of the waveform we wish to record. These sensors are being integrated with the time-lens based recording system. In the past the output was time-magnified using fiber Bragg gratings at the output to stretch the waveform in time. In this case, the incident x-ray signal is mapped to a magnified time trace, which can be recorded with higher fidelity on a streak camera or oscilloscope than without

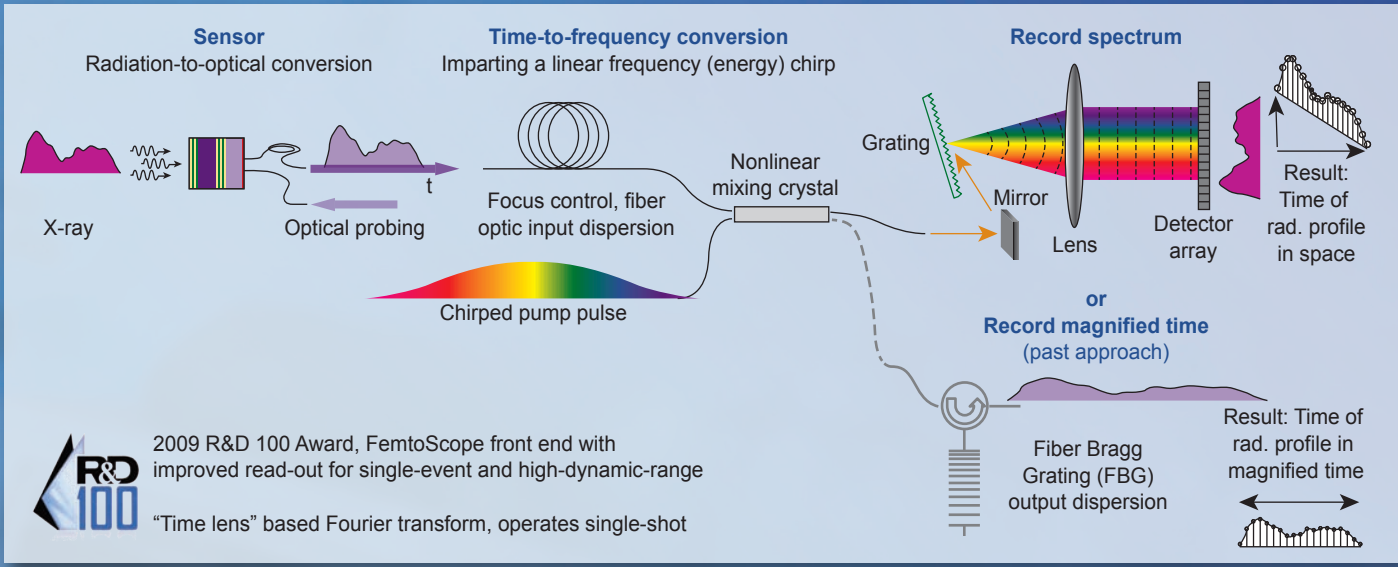

Figure 4. System conceptual diagram integrating an ultrafast x-ray sensor that produces a modulated optical response with a time-lens based processor. Past work focused on time magnification using fiber Bragg gratings at the output to create a magnified waveform recorded in time with streak cameras or oscilloscopes. Today, our system utilizes a conventional grating-based spectrometer to map the waveform to space where it can be recorded on a conventional high-performance CCD camera.

the magnification. Today we are using a conventional grating-based spectrometer to map the waveform out in space, and record it with a charge coupled device (CCD) camera (Figure 4).

The true potential of temporal imaging is just beginning to be explored. The FemtoScope could also be applied to several other research facilities and experiments with diagnostic needs similar to those of the NIF. The Defense Advanced Research Projects Agency co-funded Livermore to develop the technology for LIDAR, which measures the properties of scattered light to gather information about a distant target. The same high repetition rate system has applications in particle counting and sub-picosecond resolution time-of-flight measurements at the Large Hadron Collider at CERN, where scientists are recreating in the lab conditions just after the Big Bang and studying the basic nature of subatomic particles.

The FemtoScope will also be a valuable tool for Livermore researchers who are beginning development of a new energy concept known as the Laser Inertial Fusion Engine, or LIFE, which is based on physics and technology developed for NIF. LIFE has the potential to meet future worldwide energy needs in an inherently safe, sustainable manner without carbon dioxide emissions, while dramatically shrinking the planet's stockpile of spent nuclear fuel.

Related References

1. Hernandez, V. J., C. V. Bennett, B. D. Moran, A. D. Drobshoff, C. Langrock, D. Chang, M. M. Fejer, and M. Ibsen, "745 fs Resolution Single-shot Recording at 2.1 TSample/s and 104 Mframes/s Using Temporal Imaging," *OSA Nonlinear Optics Conference*, PDNFA2, Honolulu, HI, July 17, 2009.
2. Bennett, C. V., B. D. Moran, C. Langrock, M. M. Fejer, and M. Ibsen, "640 GHz Real-Time Recording Using Temporal Imaging," *OSA Conference on Lasers and Electro-Optics* CTuA6, San Jose, CA, May 6, 2008.
3. Lowry, M. E., C. V. Bennett, S. P. Vernon, R. Stewart, R. Welty, J. Heebner, O. Landen, and P. M. Bell, "X-ray Detection by Direct Modulation of an Optical Probe Beam–RadSensor: Progress on Development for Imaging Applications," *Rev. Scientific Instruments*, **75**, 10, pp. 3995–3997, 2004.
4. Bennett, C. V., and B. H. Kolner, "Principles of Parametric Temporal Imaging—Part I: System Configurations," *IEEE J. Quantum Electronics,* **36**, 6, pp. 430–437, 2000.
5. Bennett, C. V., and B. H. Kolner, "Principles of Parametric Temporal Imaging—Part II: System Performance," *IEEE J. Quantum Electronics,* **36**, 6, pp. 649–655, 2000.
6. Bennett, C. V., and B. H. Kolner, "Upconversion Time Microscope Demonstrating 103 x Magnification of Femtosecond Waveforms," *Optics Letters*, **24**, 11, pp. 783–785, 1999.

Transforming the Weapons Complex Through a Modern Manufacturing Infrastructure

Collaboration between LLNL, other Nuclear Weapons Complex labs, and private industry yields a modern, flexible pit manufacturing capability.

For more information contact:

Keith Carlisle
(925) 424-3495
carlisle4@llnl.gov

In December 2001, the government released the comprehensive Nuclear Posture Review, a report that recommends overall U.S. nuclear policy and strategy and the capabilities and forces needed to ensure that the nation's nuclear weapons remain safe, secure, and effective far into the future. While the report recommends strategies for retaining the smallest possible nuclear stockpile consistent with our need to deter adversaries and reassure our allies, it also calls for substantial investments to rebuild America's aging nuclear infrastructure.

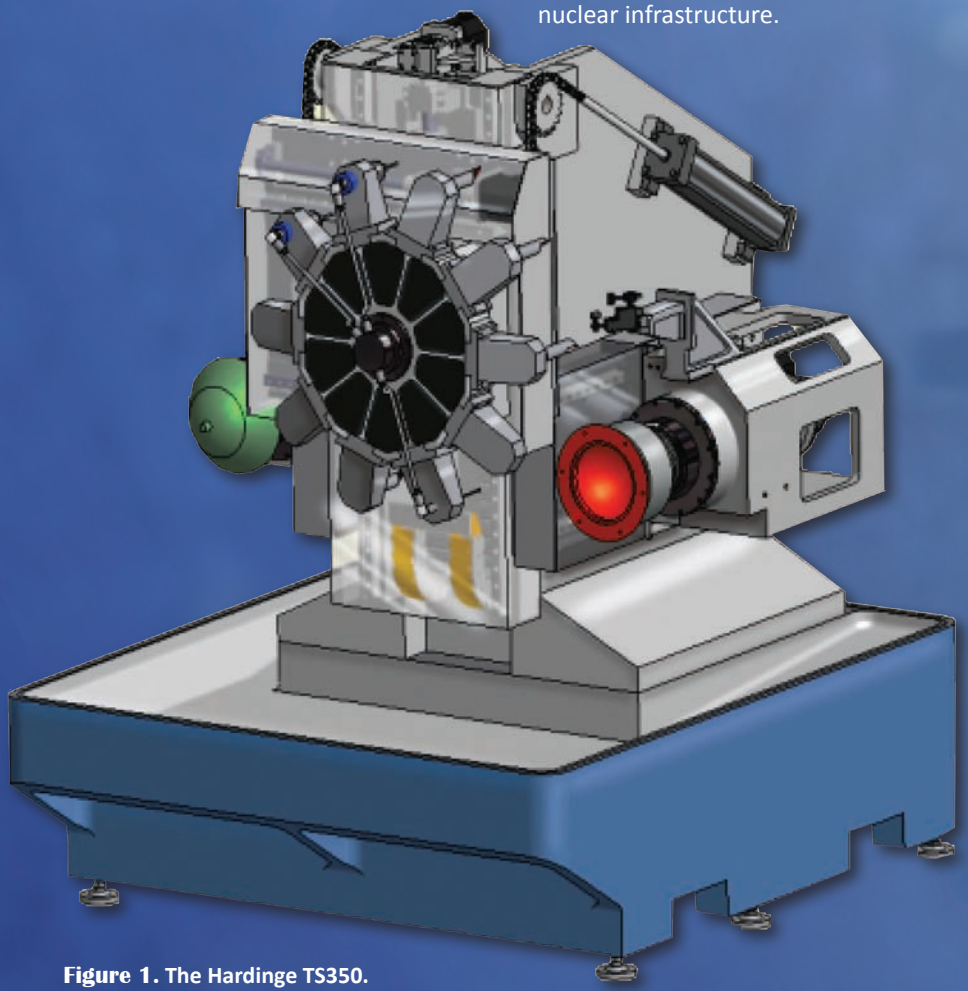

Figure 1. The Hardinge TS350.

One area identified as requiring modernization is the manufacture of weapon pits (plutonium shells). Current pit manufacturing processes depend on an unreliable infrastructure that is becoming costly to maintain and will not meet the future needs of the Nuclear Weapons Complex (NWC). The required machines and equipment were custom-designed in the 1950s when the U.S. had a strong machine tool supply chain. This has changed as the manufacturing has moved off shore, leading to the demise of our special purpose machine suppliers, and their support in maintaining production equipment. Fortunately, advances in manufacturing technology have led to development of commercial machines that can now meet the fabrication tolerances and operational flexibility required for pit manufacture.

Recognizing the significant cost advantages commercial machine supply could offer over a custom design, the National Nuclear Security Administration (NNSA) directed the Plutonium Sustainment Enterprise to identify, develop, and deploy a commercial machining center for future pit manufacture. LANL was directed to manage the project as they were the potential customer. To ensure success, the entire NWC collaborated and converged on a machine requirements specification that would meet their future needs. All participants agreed that the new machining center must:

- Consolidate and reduce the number of machines into one machining center.
- Have the required capacity, precision, and flexibility.
- Have a small footprint.
- Enable flexibility through multiple tooling, turning, drilling, and milling.

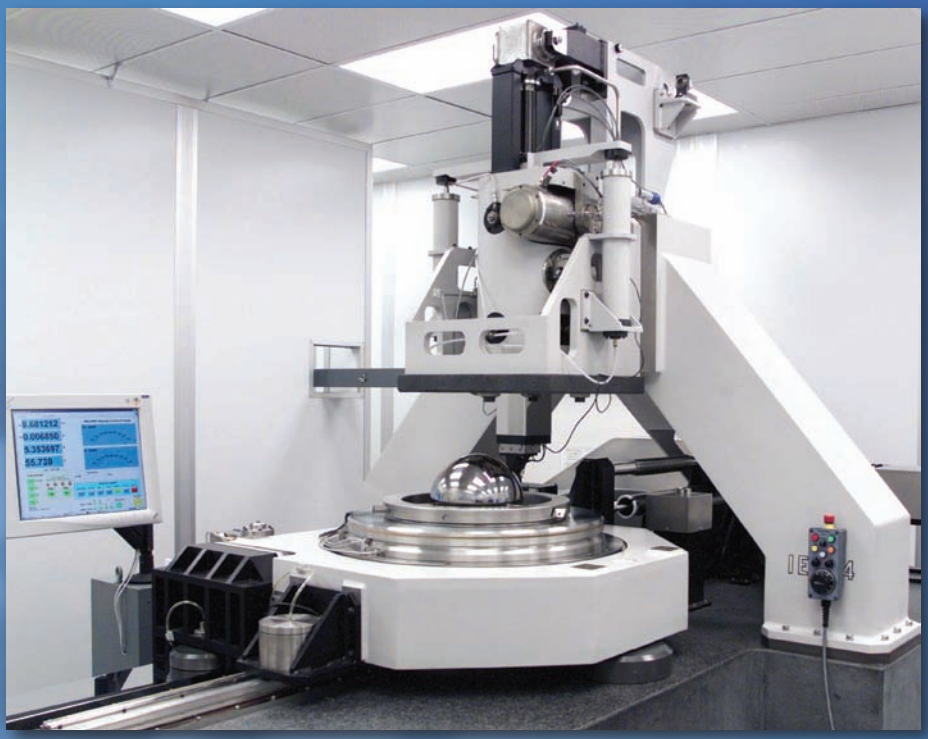

Figure 2. PrISMM.

- Support radiation-safe glove-box operation.
- Have an ergonomic design for loading and unloading, material management, ease of cleaning, and maintenance.

After an exhaustive search involving over 100 companies, the NWC concluded that a standard commercial machine would not meet the demanding requirements for glove-box operation. A combined approach was required, which would use commercial hardware configured for glove-box operation. Experts from across the NWC generated designs for a machine selection process to meet the pit requirements specification. An important aspect of this process was working with commercial machine manufacturing companies to take advantage of their existing commodity subsystems (spindles, slides, turrets, controllers, etc.) that could be configured to meet NWC needs.

At the conclusion of the selection process, six designs were submitted and evaluated against the requirements specification. From these six, the Hardinge TS350, designed by Keith Carlisle, Director of LLNL's Center for Precision Engineering, was selected (Figure 1).

Livermore's Precision Engineering group has been designing and building special-purpose machines since the 1970s, including the Large Optics Diamond Turning Machine (LODTM), the world's most accurate machine for fabricating meter-sized optics. Today, the group provides a range of machines for the manufacture and inspection of large, meter-sized laser optics for the National Ignition Facility (NIF) and the French Laser Mégajoule (LMJ). Precision Engineering also supports the Stockpile Stewardship program, having designed and built the Precision Inspection Shell Measuring Machine (PrISMM) shown in Figure 2, the primary shell-measuring machine at LLNL and potentially the entire NWC.

LLNL's unique special-purpose machine design and build capability was a major factor in the design of the TS350 and the partnership with Hardinge, a company recognized as a world leader in the supply of precision lathes. This combination optimized the design to meet the operational requirements for a glove-box machine and had all the advantages of a commercial build.

The design configuration for the TS350 was based on two basic machining operations for pit manufacture: external and internal profile forming. Each operation requires special work-holding fixtures that are both heavy and time-consuming to change. Swapping out work-holding fixtures can expose the machine operator to radiation and risk of injury, so a major design consideration for the TS350 was to eliminate or minimize those risks. This was achieved by incorporating two work spindles in the design. Each work spindle is dedicated to either internal or external work, thus eliminating the constant need for work-holding change-out. Hardinge high-precision lathe spindles met the machine requirements and had proven and reliable lifetimes.

Another factor in the design process was facilitating the handling of multiple cutting tools, including fixed tools for turning and boring, live tooling for drilling and milling, and part probing. To reduce the need for manual tool change, modern commercial machines use automated tool changing units, which are flexible and robust. However, these units can be a risk when used in a glove-box environment because of maintainability and the difficulty of maintaining cleanliness for criticality management. An indexing tool turret offered a more suitable alternative, and Hardinge had considerable experience in their use for this type of machining operation.

A major design constraint was minimizing the overall size of the machine to achieve a small footprint to reduce facility space requirements in a radiation zone. The cost of decontamination and eventual disposal of a machine at the end of its life was also a major concern, requiring design for ease of cleaning and disassembly.

Many configurations were reviewed before reaching the final design of the TS350. The vertical column design provided the smallest footprint. The

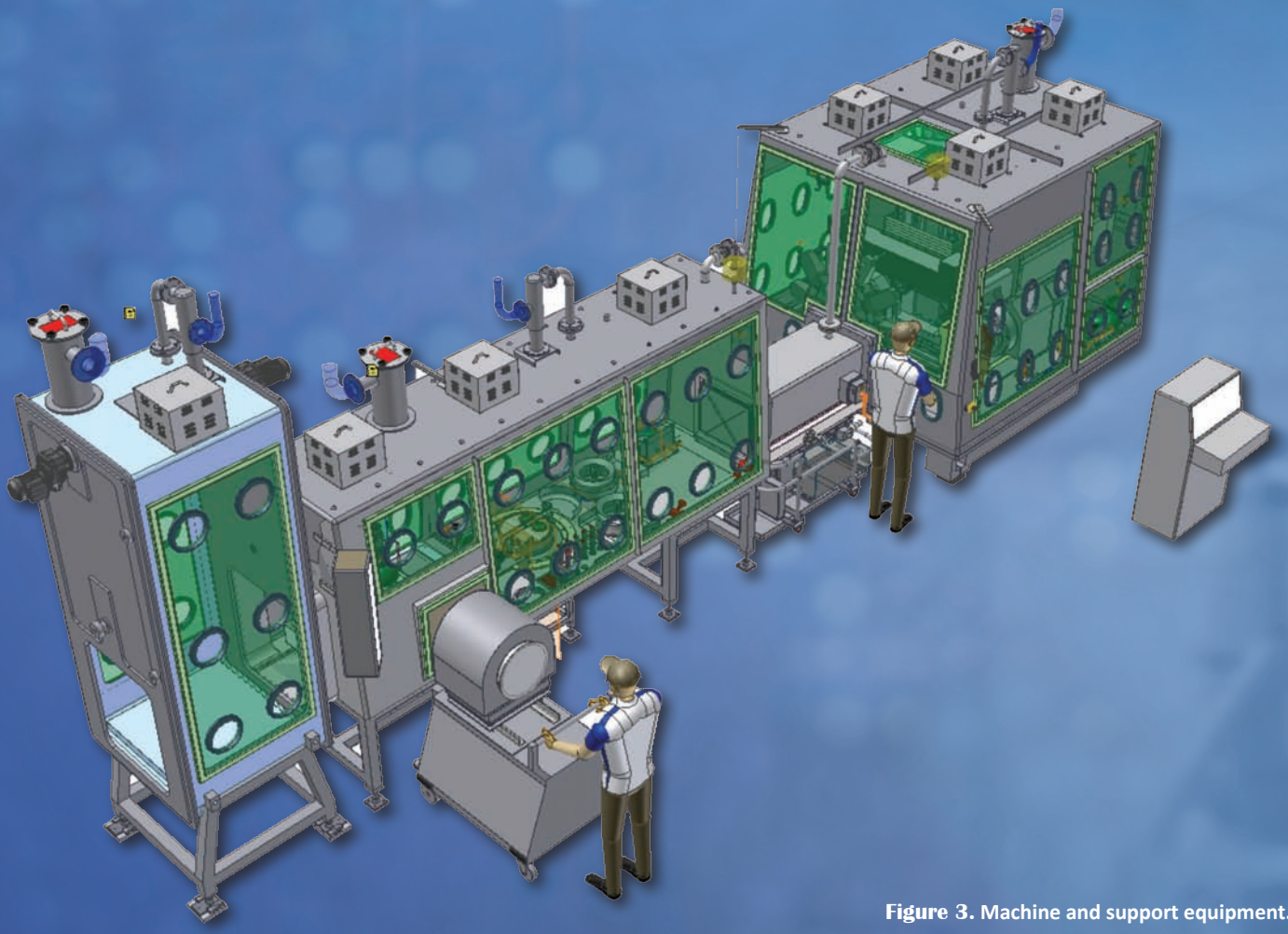

Figure 3. Machine and support equipment.

work-head spindles and turret are positioned at an operational height determined by glove-box ergonomics. Mounting these units on horizontal slide-ways maintained the required operational height for all machining operations. Good operator access is also achieved by keeping the glove-box profile parallel and close to the machine axis.

To maximize machine flexibility, a vertical servo axis was incorporated to allow raising and lowering the turret. This provided greater flexibility for the live tooling (drilling and milling), use of a three-axis "tool-setting station," tool-setting after indexing (which eliminated turret indexing errors), and a parking zone for better access for cleaning and work fixture change-out.

An important aspect of the machine design is its integration with the glove-box design, which is essential for the machine operation including loading, unloading, part transfer, tool change, machining, chip management, cleaning, and maintenance. All operations are performed through glove ports, so positioning of these ports relative to the machine was important, as was positioning of windows. Arm reach through the glove port has a critical effective length: if too short or long to carry out an operation, operator strain and injury could result. Awkward reach is also the main cause of a glove breach. Reducing operator injury and glove port breaches was a major objective of the system design, so the design team comprised engineers, machine operators, maintenance technicians, and an occupational physiotherapist with knowledge of glove-box injuries. Experts in the glove-box industry, the NWC, and the UK Atomic Weapons Establishment (AWE) also were consulted.

Proposed designs were reviewed and optimized using Delmia VNC (a software package that allowed combination of both the machine and glove-box design models), which allowed simulation of the machine's kinematics and its controller, including part program simulation for part fabrication. The same software was used to model operator ergonomics. The designs were also evaluated by AWE using their own specially developed 3-D simulation package. Using computer-aided design models of the machine and glove box, a full-size, three-dimensional image of the machine was generated. Figure 3 shows a typical model of the machine and support equipment.

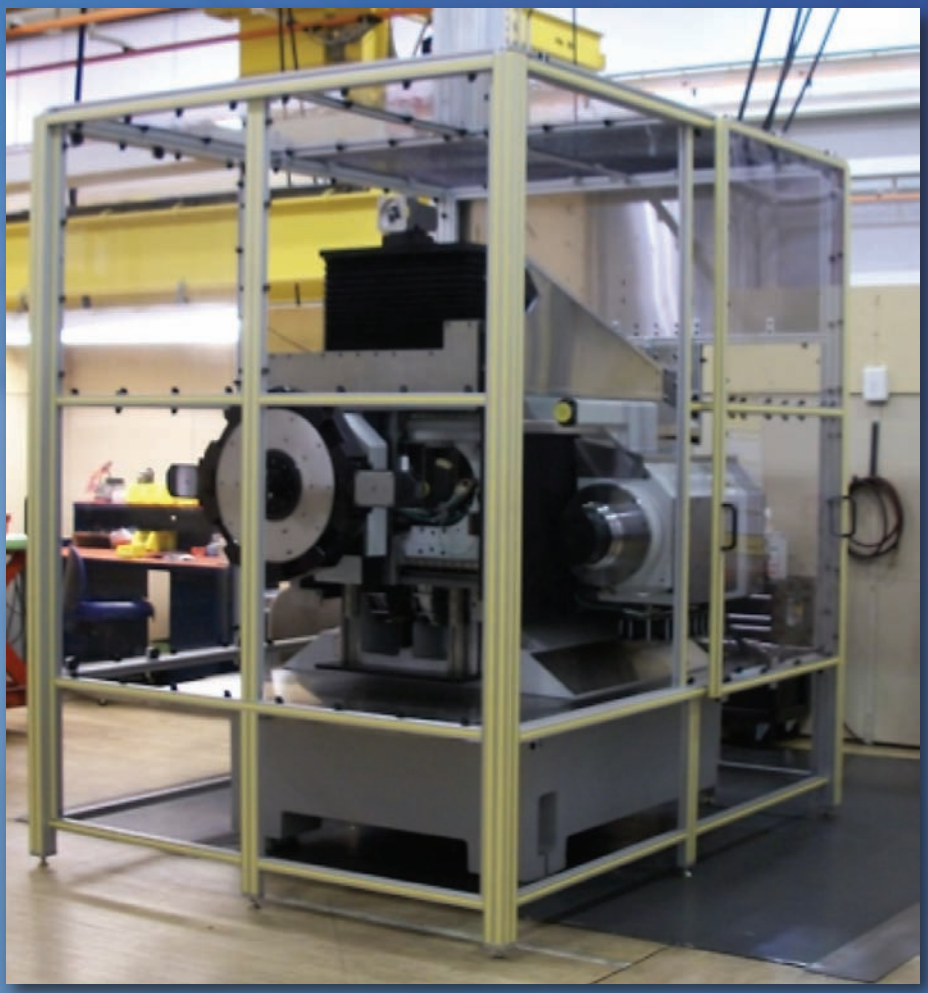

Figure 4. TS350 undergoing machining trials.

Using only a head-mounted vision system, the operators and designers were able to move 360° around the virtual machine. This enabled glove ports to be evaluated for position and reach, and ensured window placement was optimal for visibility. Machine operability was also tested, providing essential feedback to the machine design without the need for building a full-scale model. This system provided instant operational feedback for design changes, greatly reducing the risk of discovering design problems after manufacture and avoiding cost and schedule overruns.

In parallel with the TS350 machine design, LLNL worked within the Plutonium Sustainability program to develop a casting process for plutonium shells that achieved near net-shape. This work resulted in major reductions in both unit cost and waste material and also eliminated a thermal process that removed a production bottleneck. The near-net-shape casting enabled a 50% reduction in material to be removed by the TS350 machine and a potential 50% reduction in machining time and collection of waste material, which in turn greatly reduced operator radiation exposure. The reduction in mass reduces the potential for operator injuries during part handling and transfer within the glove box.

With the award of the manufacturing contract to Hardinge, the TS350 is now undergoing trials at their site (Figure 4) where the machine is meeting all expectations.

This project owes its success to the collaboration of many engineers across the NWC and AWE. The machine tool builder has been an integral part of the process, selecting and integrating their proven products into the design and producing a cost-effective solution they can maintain and support in the future. The TS350 provides NNSA with a robust, modern manufacturing center that is fully capable and sufficiently flexible to resolve technical problems in the stockpile, and able to respond to adverse geopolitical change. AWE indicated they intend to purchase the TS350 to meet their future needs, and the machine tool builder may offer a commercial version of the machine. Keith Carlisle received an Award of Excellence for the planning, managing, and execution of the modern turning center evaluation and selection process and for significant contributions to the Stockpile Stewardship Program.

Ultrahigh-Resolution Adaptive Optics Optical Coherence Tomography

Enabling early diagnosis and treatment of blinding eye disease.

For more information contact:

Diana C. Chen
(925) 423-5664
chen47@llnl.gov

Around the world, millions of people suffer from eye diseases that degrade the retina, the light-processing component of the eye, causing blindness. Ophthalmologists observe the retina to diagnose and monitor a wide variety of blinding diseases; however, conventional instrumentation does not provide sufficient resolution to reveal the cellular-level details that would allow detection and monitoring of ocular diseases at their earliest stages. Funded by the National Eye Institute, Livermore scientists and engineers, in collaboration with the University of California at Davis, Indiana University, and Boston Micromachines Corporation in Cambridge, Massachusetts, have created an optical coherence tomography (OCT) system that incorporates microelectromechanical systems (MEMS) and adaptive optics (AO) to noninvasively observe and record ultrahigh-resolution, three-dimensional (3-D) retinal images in real time. MEMS-AO-OCT allows precise, *in vivo* visualization and characterization of all the cellular layers in the human retina. It also provides a permanent, digitized record of clinical observations for monitoring disease progression and the effectiveness of therapeutic treatments.

The optical structures in the eye, particularly the cornea and lens, can produce ocular conditions such as myopia, hypermetropia, and astigmatism that many of us encounter in our natural vision. As a result of these aberrations, we see blurred images. During retinal scans, these aberrations also degrade the image quality obtained from traditional OCT or ophthalmoscopes.

MEMS-AO-OCT incorporates an AO system similar to the one pioneered at Livermore, with initial support from the Laboratory Directed Research and Development Program, for use in large, high-powered telescopes, such as those at W. M. Keck Observatory in Hawaii. In this capacity, AO systems correct wavefront aberrations caused by atmospheric distortion, which blur our view from Earth of stars, galaxies, and other celestial objects. The same principle is applied to MEMS-AO-OCT, except that the optics correct and compensate for aberrations from ocular conditions. AO compensates for optical aberrations by controlling the phase of the lightwaves, or wavefronts. It continuously samples optical aberrations and then automatically corrects them.

As shown schematically in Figure 1, the MEMS-AO-OCT uses an AO system to automatically measure the optical aberrations in the eye with a wavefront sensor and rapidly compensate for these aberrations with a wavefront

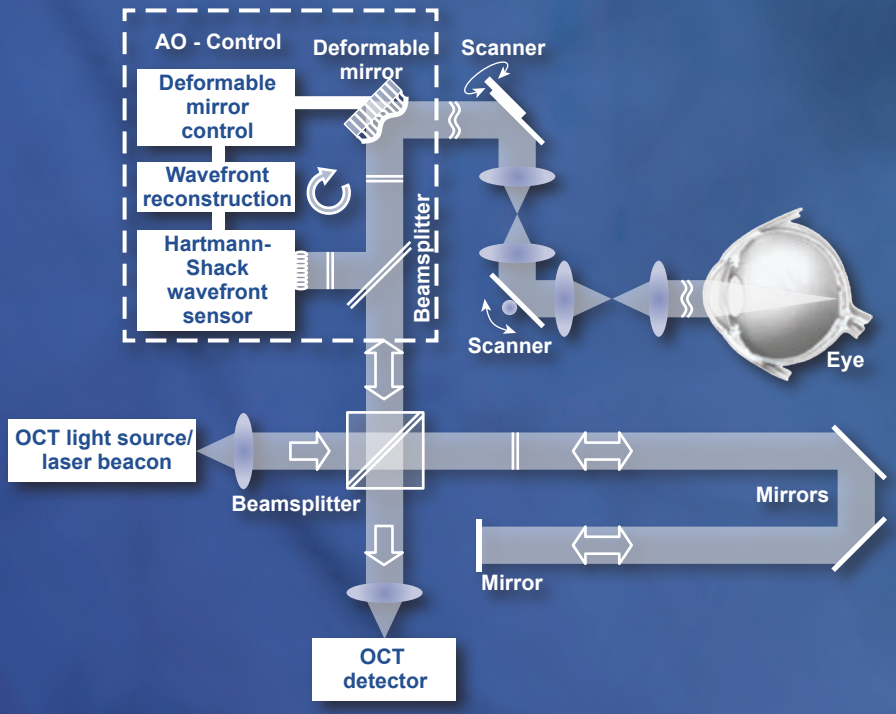

Figure 1. Schematic of a MEMS-AO-OCT system.

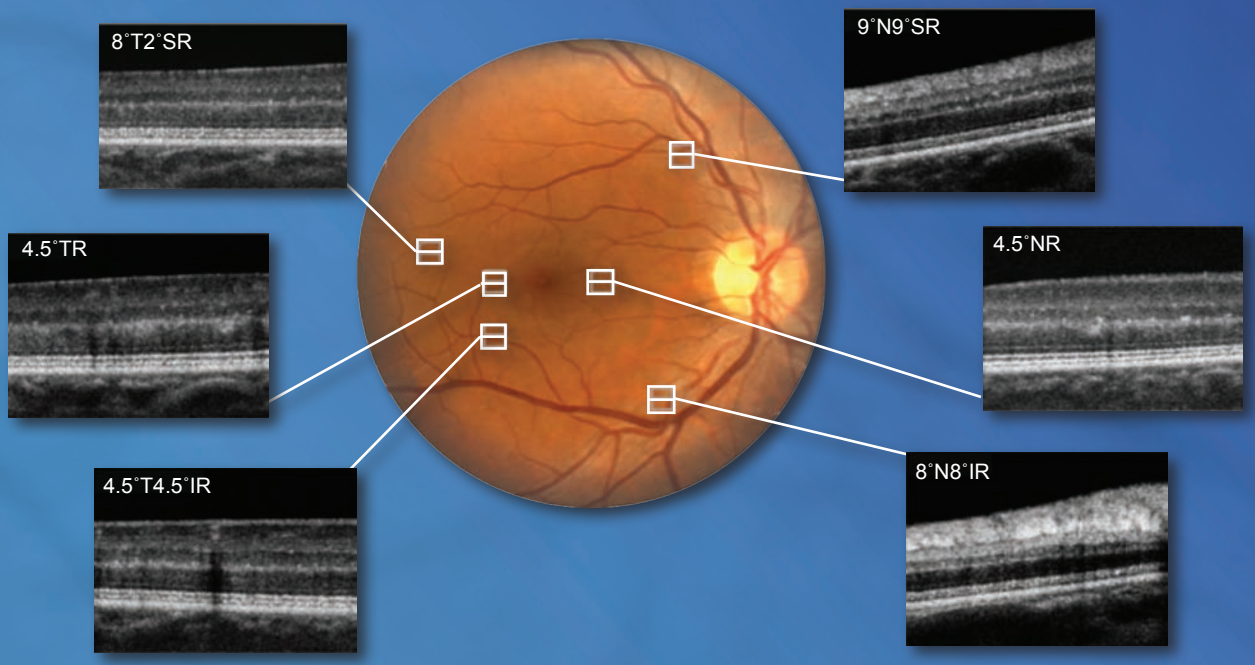

Figure 2. Example of the AO-OCT application for clinical imaging.

corrector. The aberration-free signals are then integrated with the OCT for 3-D image acquisition. Implementing AO in the system increases lateral resolution by approximately an order of magnitude. Without aberration correction from the AO, the lateral resolution of a clinical OCT system is not sufficient for imaging individual cellular structure.

The wavefront corrector is a critical component in the system. In traditional AO systems, the wavefront corrector can be both large and expensive. The MEMS-AO-OCT was designed using a MEMS-deformable mirror to reduce the size and cost of the system without sacrificing speed or accuracy. Using this state-of-the-art AO technology enables the implementation of an instrument suitable for clinical practice. The MEMS-AO-OCT constructed at LLNL is the first instrument that has been optimized for clinical use. This optimization involved a number of critical features including compact design and automating several components to enable the instrument to be operated efficiently by a clinician.

OCT systems are based on interferometry, where light from a single source is split into a sample and a reference beam. These two separate beams travel along different paths until they ultimately reunite in a detector that measures their interference. In MEMS-AO-OCT, an ultrabroadband light is generated using a superluminescent diode, and the sample beam propagates through a series of telescopes, mirrors, and horizontal and vertical scanners before reaching the patient's eye. The light beam is focused onto the patient's retina in a raster, or uniform, pattern, creating individual "snapshots" of each layer. A wavefront sensor automatically measures the patient's optical aberrations. A MEMS deformable mirror working in conjunction with a Badal optometer and a pair of rotating cylinders then compensates for the distortions. These components make the device effective even for patients who have large refractive errors, obviating the need to fit patients with trial lenses. The light reflected off the retina is then relayed back through the system to the detector. The reference beam, whose path length matches that of the sample beam, reflects off a pair of mirrors into the detector.

Compact afocal telescopes align the system components with the patient's pupil to achieve precise measurements. Inside the detector, a spectrometer and a charge-coupled-device camera record the sample and reference signatures. Custom computer software interprets the recorded signals and produces high-resolution, 3-D, digital images. The device has a total footprint of approximately 0.5 cubic meters and can be easily placed and moved within a physician's office. In addition, its commercial components make the system a financially feasible option for practices, and its cost is competitive with existing instruments that have much lower resolution.

Clinical Results

To date, more than 100 individuals have been clinically tested with AO-OCTs built and operated at the University of California, Davis and Indiana University. These instruments have been used to image both healthy and diseased eyes with different amounts of ocular aberration.

The AO-OCT system can acquire data at different retinal eccentricities to allow high-resolution sampling of retinal features of interest that are not resolvable by other methods. Figure 2 shows results of an AO-OCT imaging

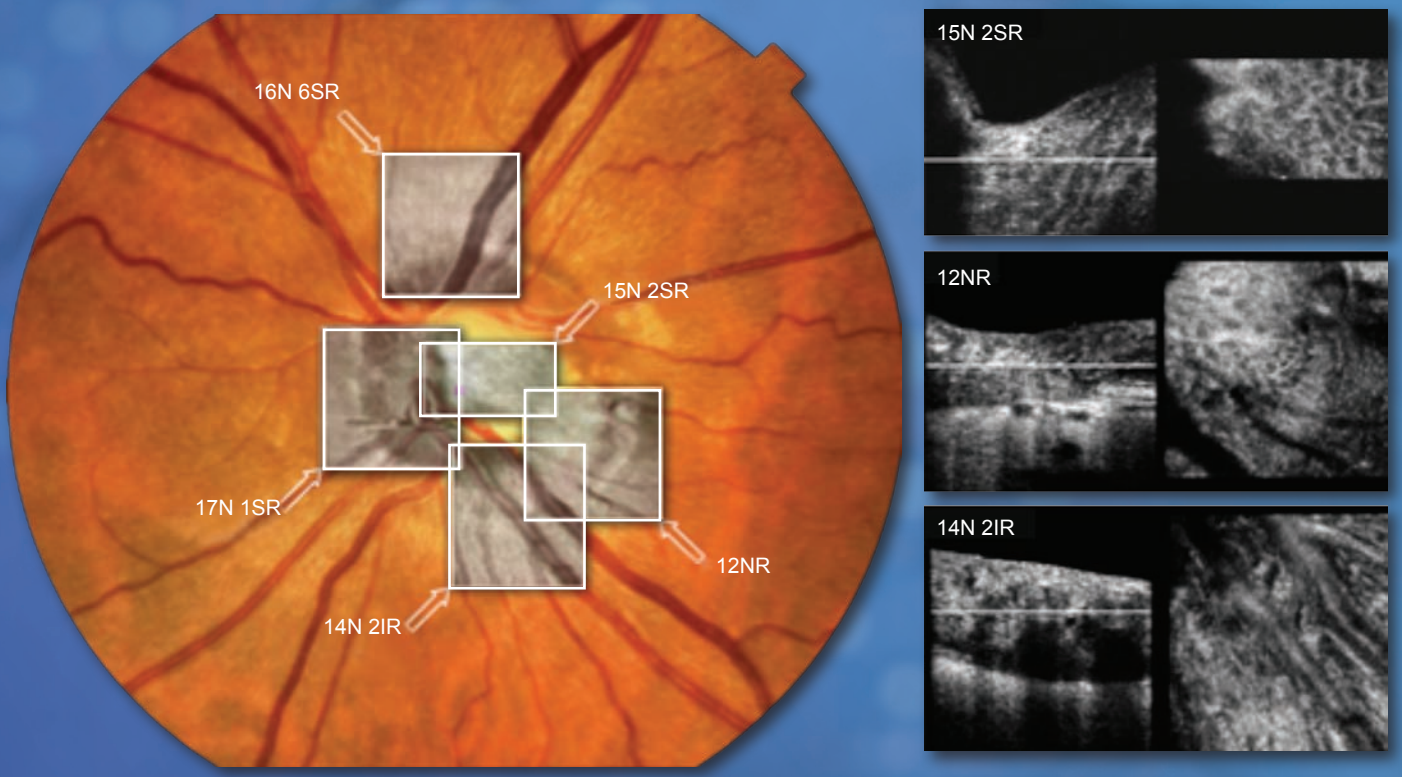

Figure 3. Example of AO-OCT imaging of the optic nerve head. (Left) Fundus photo with superimposed OCT-fundus reconstructed from the AO-OCT volumes. (Right) Representative B-scans and C-scans.

session during which several retinal eccentricities were imaged with 1 × 1 mm sampling volumes at the fovea (dark region) and optical nerve head (ONH, bright region).

Chromatic aberration effects increase with retinal eccentricity, which makes the imaging of eccentric locations such as the ONH more difficult. We find that retinal structures are resolved and revealed using AO-OCT that were not visible using OCT without AO correction. Imaging these microscopic ONH structures is critical for diagnosing and monitoring the progression of ONH diseases. Figure 3 shows results of ONH imaging with AO-OCT.

Figure 4 shows micro-traction in the center of the fovea. Because of its small size, it was misdiagnosed using other image modalities including commercial

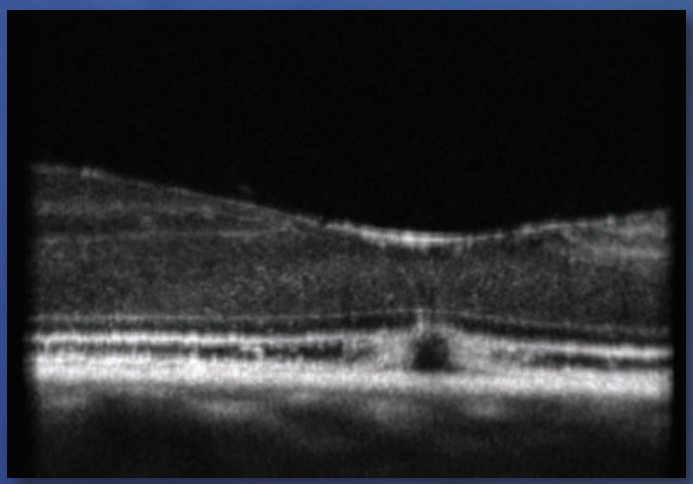

Figure 4. Micro-traction was not detected with other imaging modalities.

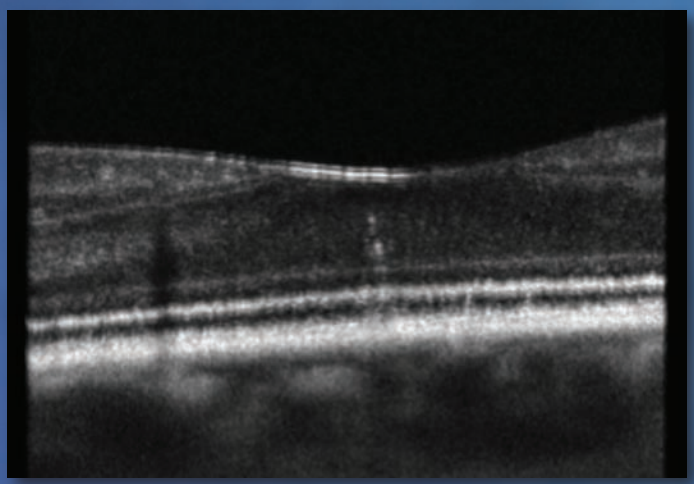

Figure 5. Microscotoma cannot be detected with other imaging modalities.

Fourier domain OCT and fundus photography. Because AO-OCT has a much higher resolution, it clearly reveals the problematic structures and provides ophthalmologists with an effective imaging tool for diagnoses.

Figure 5 represents a case of microscotoma (a small blind spot close to the fovea) that could not be detected by any standard imaging instrument. However, AO-OCT indicates that structural disruptions in the outer nuclear layer extending to the photoreceptor layers are good candidates to account for the reduction in vision reported by the patient.

The AO-OCT system can acquire 3-D, ultrahigh-resolution images over small retinal areas (approximately 300 × 250 × 600 µm), which reveal cellular structures within the retina, as shown in Figure 6. Volumetric rendering allows detailed insight into microscopic structures not possible with 2-D scans. For instance, an abnormal appearance of the photoreceptor cell layer is indicative of numerous blinding diseases—such as macular degeneration, diabetic retinopathy, and retinitis pigmentosa—while abnormalities in the retinal nerve fiber layer can be an indicator of glaucoma.

Impact of Innovation

The MEMS-AO-OCT combines AO technology, OCT, and confocal scanning laser ophthalmoscopy to resolve features that cannot be detected by conventional imaging tools. MEMS-AO-OCT provides real-time, high-resolution, cellular-level images of the living human retina, and the technology could be adapted for use in other medical fields. Because biological tissues absorb and reflect light differently, the intensity and wavelength of the light source must be gauged to specific tissues to optimize image resolution. MEMS-AO-OCT can be easily adjusted to accommodate these varying light parameters, making it a valuable tool for diagnosing and treating many health conditions, including cardiovascular disease. In addition, dentists could image both hard (teeth) and soft (gums) tissues, and oncologists could identify cancer cells well before they develop into tumors. The system could ultimately help medical professionals accurately diagnose diseases, dramatically reducing the cost of medical treatment and improving the quality of life for millions of people.

Related References

1. Chen, D. C., S. Oliver, S. Jones, R. J. Zawadzki, J. Evans, S. Choi, and J. Werner, "Compact MEMS-Based Adaptive Optics: Optical Coherence Tomography for Clinical Use," *SPIE*, **6888-OF**, 2008.
2. Zawadzki, R. J., Y. Zhang, S. M. Jones, R. Ferguson, S. S. Choi, B. Cense, J. Evans, D. C. Chen, D. Miller, S. Olivier, and J. Werner, "Ultrahigh-Resolution Adaptive Optics—Optical Coherence Tomography: Towards Isotropic 3 µm Resolution for *In Vivo* Retinal Imaging," *SPIE*, **6429–09**, 2007.
3. Zawadzki, R. J., S. Jones, S. Olivier, M. Zhao, B. Bower, J. Izatt, S. Choi, S. Laut, and J. Werner "Adaptive-Optics Optical Coherence Tomography for High-Resolution and High-Speed 3D Retinal *In Vivo* Imaging," *Optics Express,* **13**, 21, pp. 8532-8546, 2005.
4. Zawadzki, R. J., S. Choi, A. Fuller, J. Evans, B. Hamann, and J. Werner, "Cellular Resolution Volumetric *In Vivo* Retinal Imaging with Adaptive Optics–Optical Coherence Tomography," *Optics Express,* **17**, 5, pp. 4084–4094, 2009.

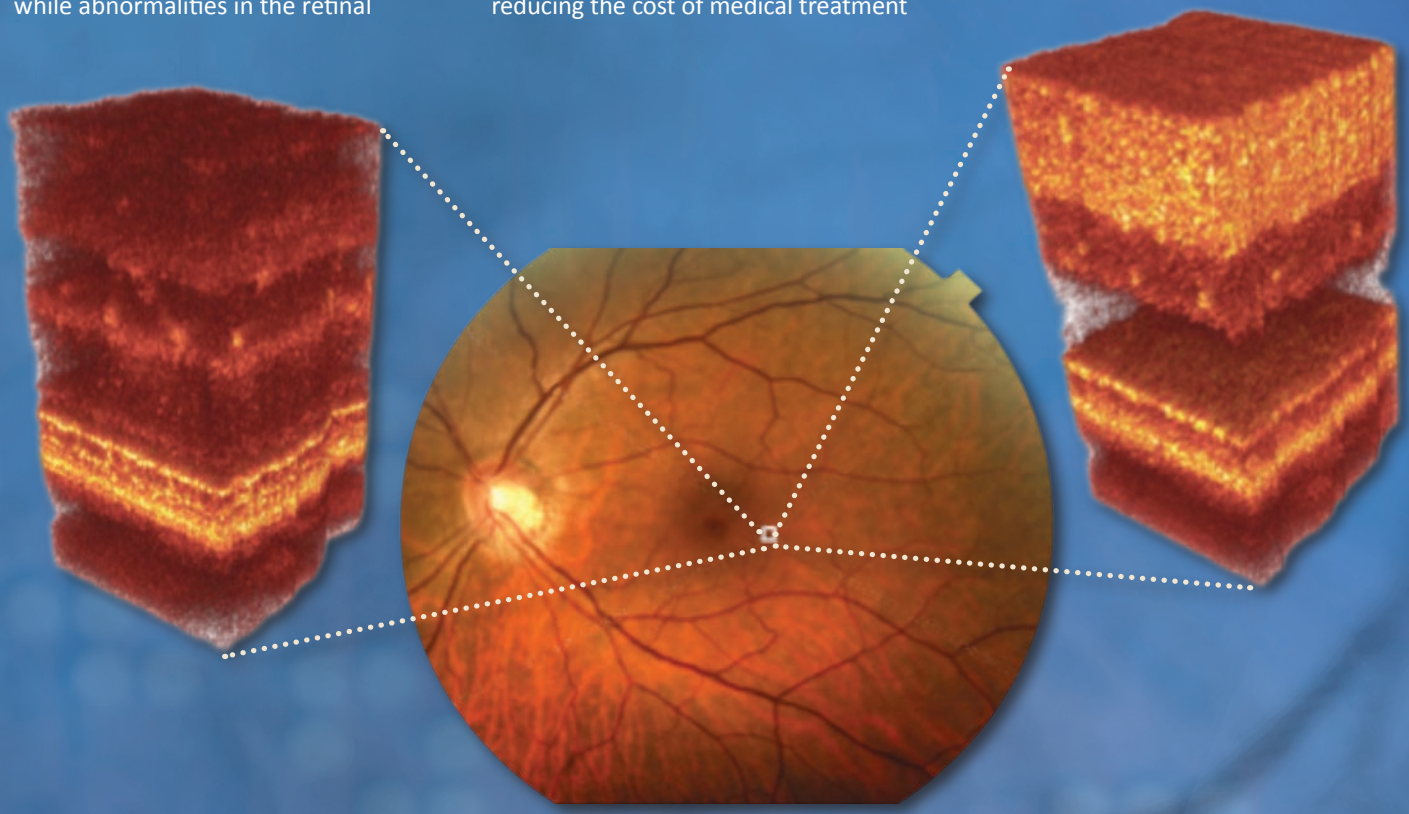

Figure 6. Example of ultrahigh-resolution volume acquisition with AO-OCT.

Multiphysics Engineering Simulations with ALE3D

Implementation of magnetohydrodynamics in ALE3D provides new and exciting capabilities for pulse power, microfluidics, and other applications.

For more information contact:

Daniel A. White
(925) 422-9870
white37@llnl.gov

Simulation is a key element of modern engineering, complementing experimentation and "back-of-the-envelope" calculations. We define simulation as the solution of a mathematical model of a system using numerical methods, with those numerical methods being implemented and executed on a computer. Simulation, therefore, is not just visualization or animation; it is a quantitatively correct approximation of reality. Engineers have long used single-physics simulations, which employ computer codes optimized for a single area. For example, an electrical engineer would use a computer to solve the equations of electromagnetics when designing an antenna, a structural engineer would use a computer to solve the equations of elasticity when designing a bridge, or a mechanical engineer would use a computer to solve the equations of heat transfer when designing a cooling system. There are many engineering problems, however, whose complexity requires fully coupled multiphysics simulations. A multiphysics simulation incorporates multiple, disparate mathematical models, which are coupled, and solves these models self-consistently. Developing a multiphysics simulation code requires a close collaboration between physicists, engineers, mathematicians, and computer scientists, and is a large undertaking. The effort to develop a three-dimensional, massively parallel, multiphysics code can exceed 100 man-years. However, the end result is the ability to gain insight into complex phenomena, the ability to "see" quantities like electric fields and thermal fluxes that cannot be measured experimentally, and the ability to predict and optimize the performance of next-generation devices.

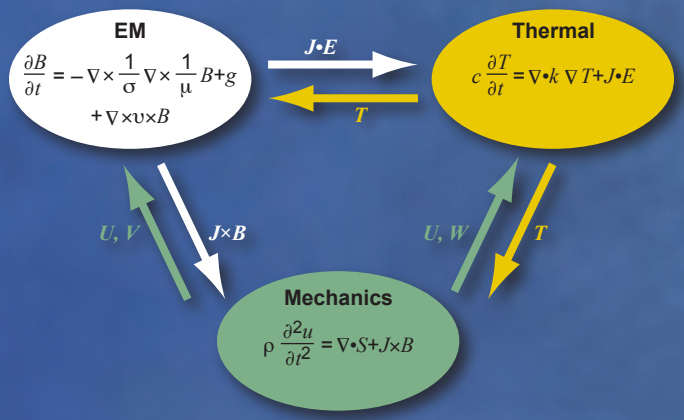

Figure 1. Electromagnetics is represented by the white module, heat transfer is represented by the yellow module, and hydrodynamics is represented by the green module. The arrows show the physical quantities that are the input and the output of each module. For example, the electromagnetics module produces Joule heating, *J•E*, which is input to the heat transfer module, and the heat transfer module produces temperature, *T*, which is input to both the electromagnetics and hydrodynamics modules.

ALE3D is an acronym for Arbitrary Lagrangian Eulerian in 3 Dimensions. This LLNL-developed multiphysics simulation code incorporates hydrodynamics, heat transfer, chemistry, incompressible flow, and electromagnetics. This article focuses on recently implemented magnetohydrodynamics applications; these are applications that require a fully coupled solution of hydrodynamics, heat transfer, and electromagnetics. Magnetohydrodynamic phenomena are most commonly associated with the study of electrically conducting gases (i.e., plasmas) such as those that are studied in the realms of astrophysics or magnetic fusion energy.

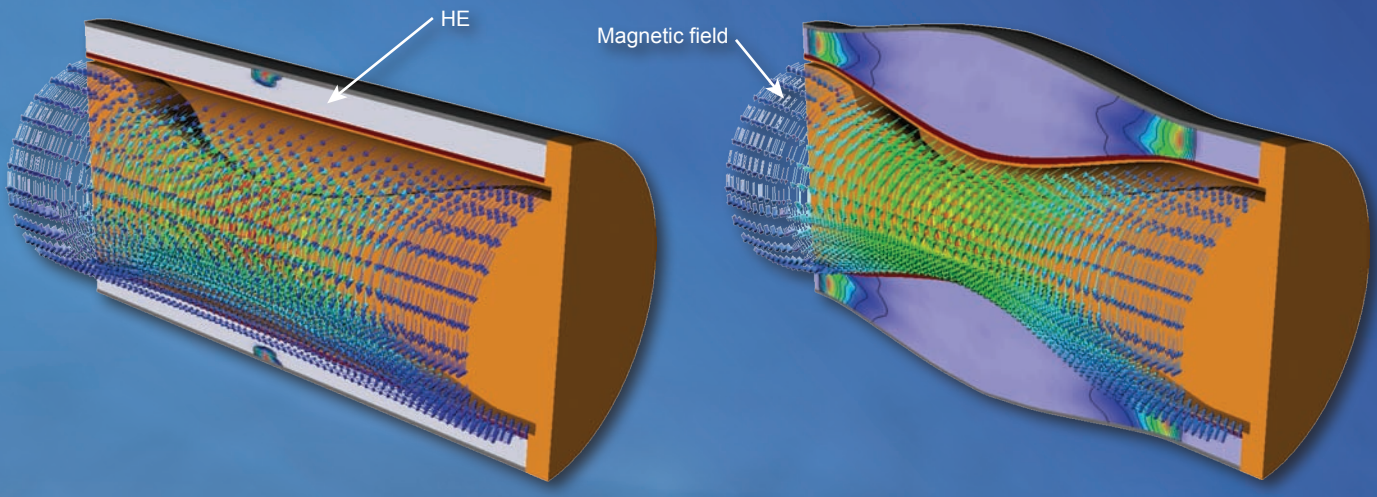

Figure 2. Simulation of an explosive magnetic flux compression generator. The graphic on the left is a snapshot just as the high explosive (HE) is detonated; the graphic on the right is at a later time when the magnetic field has been compressed. The vectors represent the magnetic field; the contours represent pressure.

Computer codes for simulating this class of magnetohydrodynamics problems have existed for some time. The important feature of our magnetohydrodynamic implementation in ALE3D is that it excels for problems that involve solid materials that undergo gross deformation, melting, and transition to plasma. The mutiphysics nature of such problems is illustrated in Figure 1, where electromagnetics is represented by a white module, heat transfer is represented by yellow, and hydrodynamics is represented by green. The arrows show the physical quantities that are the input and the output of each module. The coupled equations are solved using an operator-splitting algorithm, and within each module the equations are solved using the finite element method. The illustration in Figure 1 is deceptive; it looks simple, but the development of this magnetohydrodynamics capability required hundreds of thousands of lines of software. Simulations using magnetohydrodynamics often require large-scale computing—a typical problem will require a week of processing time using 256 processors, while the largest problems require thousands of processors.

Opening New Horizons in Pulse Power Research

The primary motivation for developing an ALE3D magnetohydrodynamics capability was to simulate explosive magnetic flux compression generators. These generators are energy conversion devices, in that they convert the chemical energy in a high explosive to mechanical energy, and the mechanical energy is in turn converted to electrical energy. The purpose of the device is to generate a large pulse of electric current with a faster rise time than can be achieved using other means (such as capacitor banks). To function, the device is seeded with an electric current, generating a magnetic field in a cavity; the high explosive is then detonated, compressing the cavity, and as the cavity is compressed, the initial seed current is amplified in order to maintain the magnetic flux in the cavity (in accordance with Lenz's law). An example simulation of this process is shown in Figure 2. Such simulations have enabled engineers to visualize fields and currents that are difficult to measure in experiments, thus giving insight into the operation of the device. As a specific example, the device shown in Figure 2 is designed to be axially symmetric, but the effect of deviations from perfect symmetry (due to manufacturing tolerances, material imperfections, etc.) can be investigated via full three-dimensional simulation by incorporating imperfections into the simulation. The ability of ALE3D to simulate the detonation of a high explosive, combined with material motion, electromagnetic fields and currents, and heating and melting of conductors, is a very powerful and unique capability that is having a tremendous impact on the design of explosive magnetic flux compression generators.

A railgun is another energy conversion device, in some sense the opposite of a magnetic flux compression generator. In a railgun, electric current is input into the device, and the output is mechanical energy in the form of a high-velocity projectile. A railgun is essentially a linear electric motor, and the projectile is the armature of the motor. Railguns have application in defense as an alternative to traditional explosive-based guns. One advantage of a railgun is the very high velocity that can be

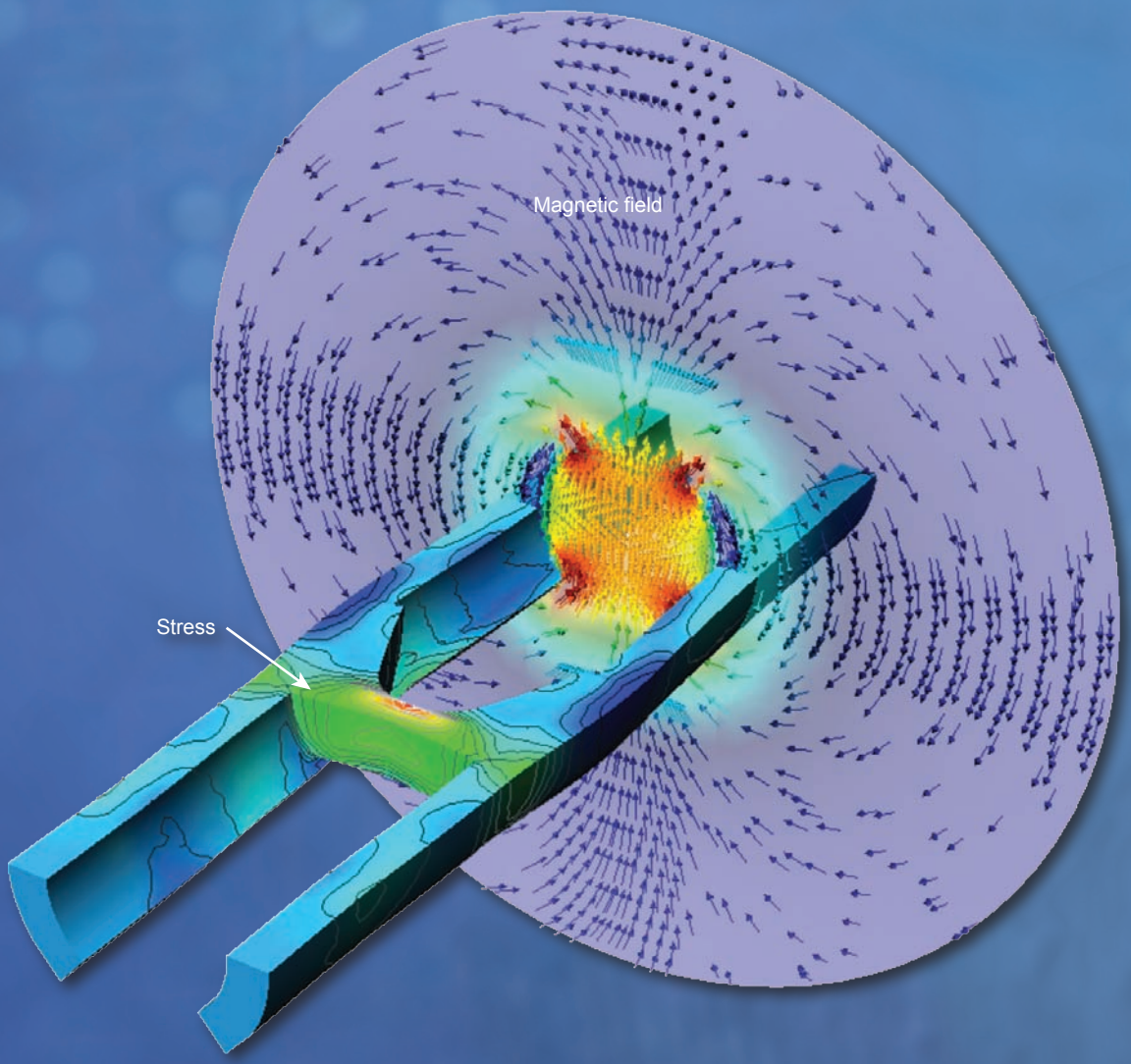

Figure 3. Simulation of a generic railgun. The armature is between two rails; current flows into one rail, through the armature, and out the other rail. This graphic shows only one-half of the geometry so that the stress within the rails can be seen.

achieved by the projectile compared to that of a traditional gun. A second advantage is that the velocity can be "dialed" by the electrical power supply. Figure 3 is a simulation of a generic railgun, with the graphic showing a cross-section of the gun. The purpose of this particular simulation was to investigate stress in the rails, which is caused by the enormous magnetic pressure in the gun. A high magnetic field is required to achieve high acceleration of the armature, but a high magnetic field also causes stress in the rails. If the gun is not properly designed (*i.e.*, if the stress is too high) it can explode, hence accurate estimation of stress via full three-dimensional simulation is essential. A novel capability of ALE3D is its ability, via an algorithm, to correctly simulate a sliding electromagnetic contact. This algorithm allows two materials to slide past each other while allowing electric current to flow across the material interface. The sliding electrical contact algorithm is quite sophisticated, involving advanced mortar finite element methods with implicit constraints to satisfy conservation of current and continuity of the magnetic field across the interface. Currently, LLNL is using the ALE3D code to assist the Office of Naval Research in their goal to design a naval railgun. ALE3D simulations are being used to investigate alternative rail geometries, alternative rail materials, and the effect of Joule heating and viscous heating on armature erosion.

Simulation Enables Virtual Prototyping

The two previous examples of magnetohydrodynamic simulation were pulse power applications involving possibly millions of amperes of current. A third example, simulating a microfluidic pump (Figure 4), is quite different and illustrates the broad utility of

multiphysics codes such as ALE3D. The key element of the pump is a magnetoelastic membrane that is manufactured by dispersing iron particles in silicone. In a traditional membrane pump, the membrane is flexed via a mechanical crank or gear system or by hydraulics. The unique feature of this pump is that it is driven by an external magnetic field: an applied magnetic field deforms the membrane, and as the membrane is deformed fluid is pulled into one side of the pump and ejected out the other side. The advantage of this magnetoelastic pump is that it does not require any external connections. This pump may have applications in microfluidics chemistry-lab-on-a-chip and in *in vivo* medical equipment. Simulations are being used to optimize the geometry of the device and to determine the required magnetic field strength. This application highlights a key payoff of LLNL's investment in multiphysics simulation: novel ideas can be virtually prototyped via simulation prior to manufacturing.

There are numerous other applications for the ALE3D magnetohydrodynamics capability. The code is currently being used to investigate the effects of aging on the performance of detonators and the effect of lightning on detonators, an important component of LLNL's Stockpile Stewardship mission. As another example, ALE3D was used successfully to investigate magnetic steering of injected fuel pellets for the Laser Inertial Fusion Energy (LIFE) project. Research and development of the ALE3D magnetohydrodynamic module continues. Current development efforts include incorporation of a model for arcing and development of models for boundary layer effects.

Related References

1. White, D., R. Rieben, and B. Wallin, "Coupling Magnetic Fields and ALE Hydrodynamics for 3D Simulations of MFCG's," Proceedings of the 2006 IEEE International Conference on Megagauss Magnetic Field Generation, pp. 371–376, Santa Fe, NM, November 5–10, 2006.
2. Rieben, R., D. White, B. Wallin, and J. Solberg, "An Arbitrary Langrangian-Eulerian Discretization of MHD on 3D Unstructured Grids," *J. Comp. Phys.*, **226**, pp. 534–570, 2007.
3. Barham, M., and D. White, "Finite Element Modeling of the Deformation of a Thin Magnetoelastic Film Compared to a Membrane Model," *IEEE Transactions on Magnetics*, **45**, 10, pp. 4124–4127, 2009.
4. Barham, M., D. White, and D. Steigmann, "Finite Element Modeling of the Deformation of Magnetoelastic Film, " *J. Comp. Phys*, **229**, pp. 6193–6207, 2010.

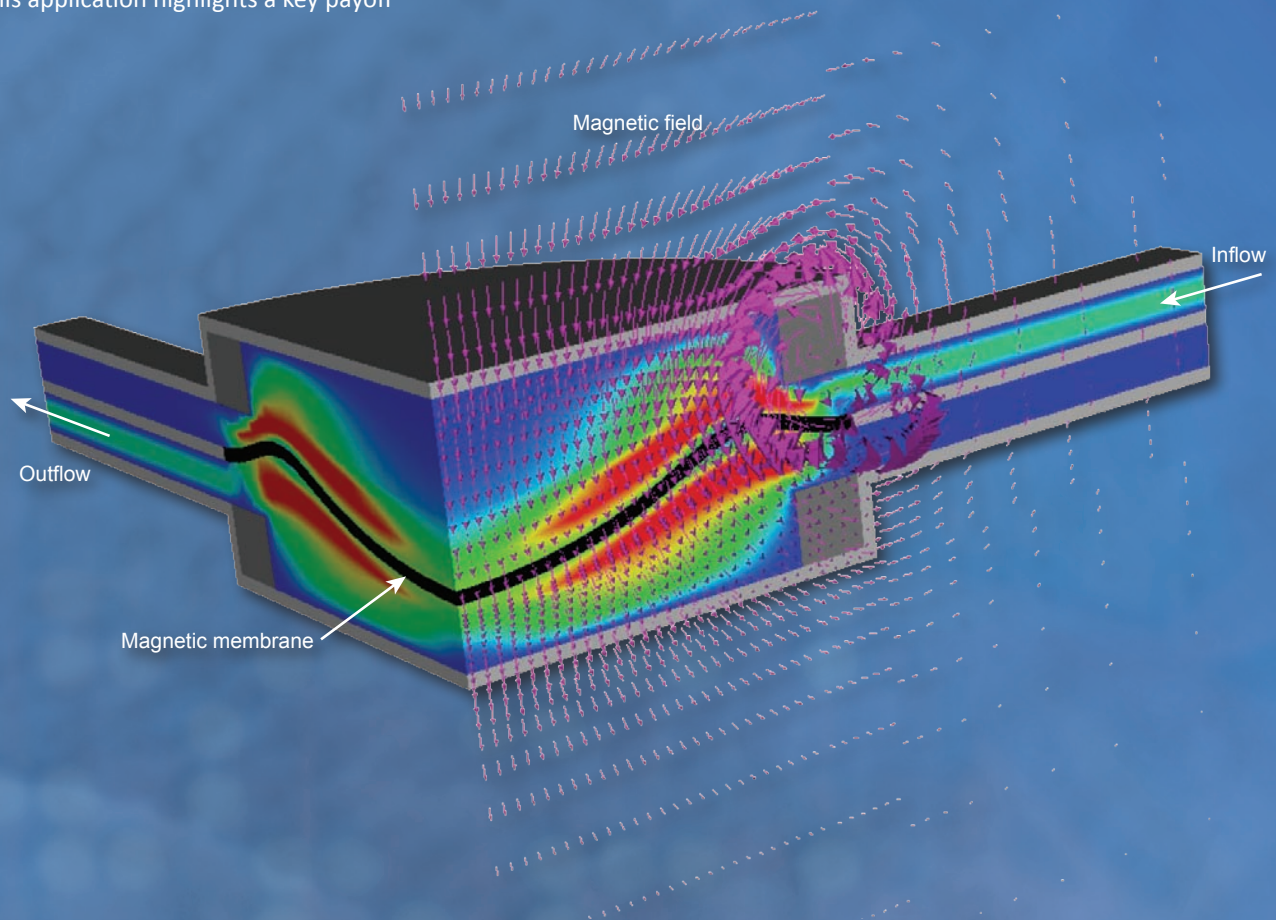

Figure 4. Simulation of a magnetoelastic-based microfluidic pump. The applied magnetic field (magenta vectors) deforms a magnetoelastic membrane (solid black), which pulls fluid into one side of the pump and expels fluid out the other side of the pump. The pseudocolor scalar field is the speed of the fluid, blue being slow and red being fast.

Computational Engineering

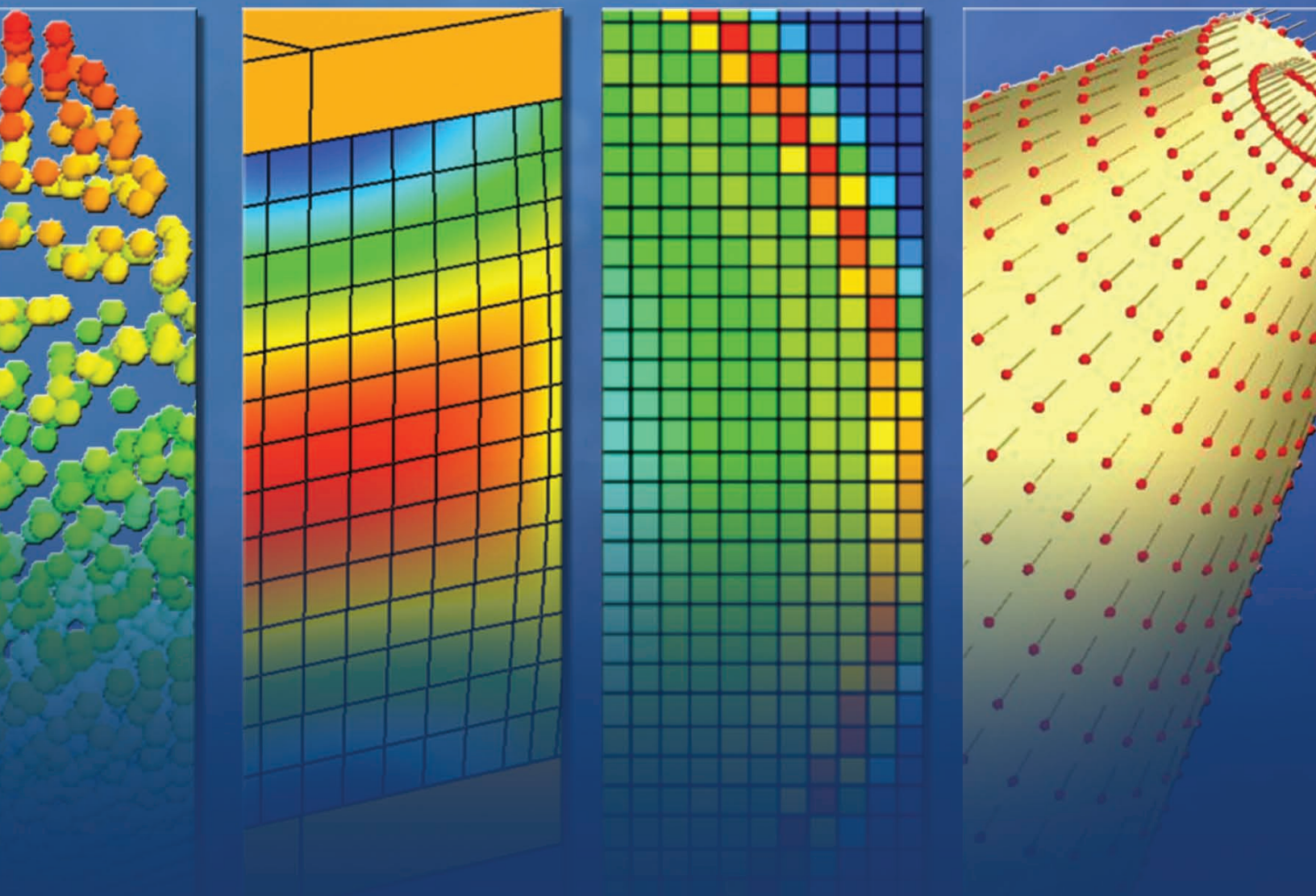

Direct Observation of Phase Transformations and Twinning Under Extreme Conditions: *In Situ* Measurements at the Crystal Scale

For more information contact:

Joel V. Bernier
(925) 423-3708
bernier2@llnl.gov

Mechanical twinning (MT) and displacive phase transformations (DPT) are complex deformation-driven mechanisms observed in polycrystalline materials including metals, ceramics, minerals, and high explosives. Both MT and DPT can have a significant effect on equation-of-state and critical mechanical properties such as strength and stiffness. *In situ* observations of MT and DPT at the crystal scale are essential for motivating, validating, and verifying advanced constitutive models. The recent availability of large, fast flat-panel detectors at synchrotron x-ray sources, such as the Advanced Photon Source (APS), has enabled the development of novel experimental techniques. We are leveraging these capabilities and developing a fully 3-D, *in situ* characterization technique having unprecedented resolutions that will accommodate quasistatic thermomechanical loading *in situ* using a uniaxial loadframe as well as a diamond anvil cell (DAC).

Project Goals

We propose to develop a novel x-ray diffraction-based experimental capability for making direct observations of MT and DPT mechanisms in individual grains embedded in polycrystalline samples subject to high pressure and temperature *in situ*. A schematic of the experimental setup is shown in Fig. 1. As a sample case, the α↔ε DPT in iron will be thoroughly characterized at the crystal scale, including the non-ambient material properties of the high-pressure ε-iron phase, which will in turn yield a calibrated crystal-scale constitutive model. Additional materials of programmatic interest, such as zirconium cerium, will subsequently be studied. We propose to extend the method to heavily deformed/higher defect content materials, and to develop a combined angular (strain) resolved and spatially (grain/domain boundary) resolved technique that forms the basis for a dedicated 3-D x-ray microscopy instrument at the APS 1-ID beamline. This includes development of algorithms and software for data analysis, including graphical user interfaces, to make the technique available to the DOE user community.

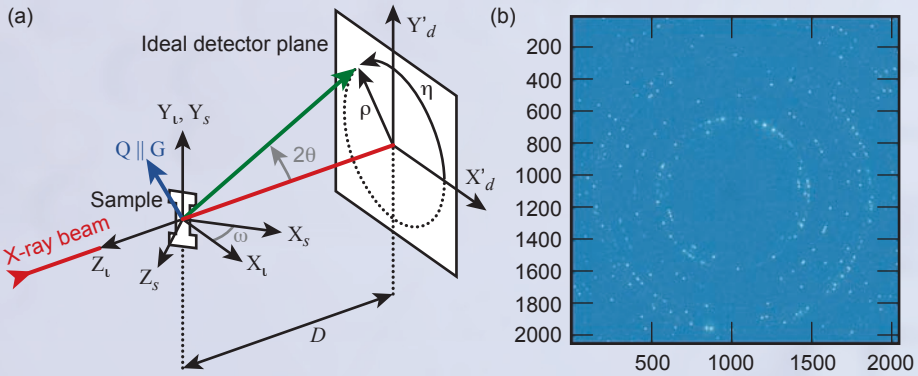

Figure 1. **(a) Schematic of the diffraction instrument geometry, showing the specimen position on the rotation stage, transmitted x-ray beam (red), a diffracted x-ray beam (green), the associated scattering vector (blue), and the flat panel detector. (b) Sample diffraction image from a magnesium AZ31 specimen rotated over Δω = 1°.**

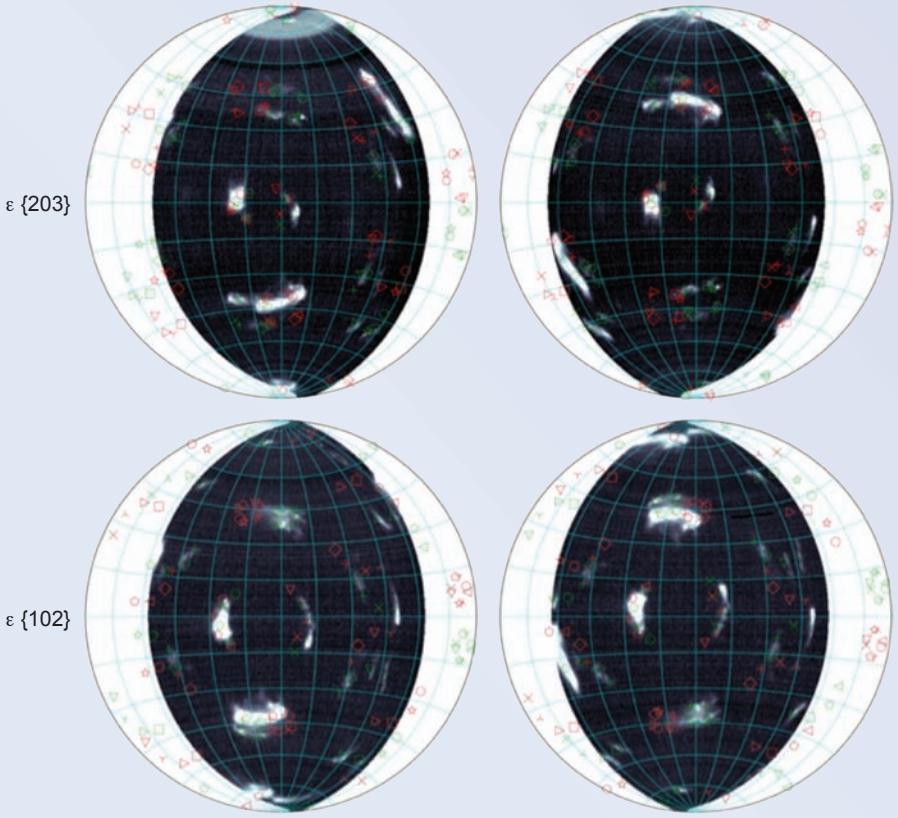

Figure 2. Results from experiment in which the α↔ε phase transformation was observed *in situ*. The location of Bragg reflections for the two indicated types of ε-phase lattice planes are plotted as pole figures in an equal area projection. The different glyphs denote the predicted locations of reflections from each variant under the Burgers path. The red and green colors correspond to the extrema of the orientation spread of the parent α phase (~15° misorientation). The correspondence of the strongest variants is quite good, even in this cursory analysis, and all variants are observed.

Relevance to LLNL Mission

This work strengthens our Science, Technology, and Engineering pillars, encompassing Materials on Demand and Measurement Science and Technology. High-fidelity material models also comprise a critical piece of the multiphysics simulation codes employed at LLNL in support of Stockpile Stewardship Science goals. This work will enable rigorous verification and validation of cutting-edge constitutive models at the relevant, crystal length scale.

FY2010 Accomplishments and Results

A successful experiment was performed at APS 1-ID in which the α↔ε phase transformation was observed *in situ* using DACs. Figure 2 shows pole figures for two ε-phase reflections, calculated post transformation at ~17 GPa. The variant selection corresponds well with the Burgers path, which corroborates reported findings. These are unique data: first-of-kind 3-D *in situ* observations of this phase transformation. It was also shown that in addition to directly observing the parent/daughter orientation relationships, it is possible to separate the hydrostatic and deviatoric strain responses throughout the loading history. This has incredible potential for providing higher-fidelity equation-of-state measurements on a wide range of materials.

Building on fundamental tools produced under Institutional funding in FY2008 and FY2009, a complete software package has been developed that facilitates:

- angular calibration of flat-panel detectors;
- diffraction image segmentation;
- grain identification through orientation indexing; and
- precise centroid/orientation/strain determination for indexed grains, including parent/daughter association under specified transformation pathways.

Related References

1. Lee, J. H., C. C. Aydiner, J. Almer, J. V. Bernier, K. W. Chapman, P. J. Chupas, D. Haeffner, K. Kump, P. L. Lee, U. Lienert, A. Miceli, and G. Vera, "Synchrotron Applications of an Amorphous Silicon Flat-Panel Detector," *J. Synchrotron Rad.,* **15**, 5, pp. 477–488, 2008.
2. Lienert, U., J. Almer, B. Jakobsen, W. Pantleon, H. F. Poulsen, D. Hennessy, C. Xiao, and R. M. Suter, "3-Dimensional Characterization of Polycrystalline Bulk Materials Using High-Energy Synchrotron Radiation," *Mater. Sci. Forum,* **539–543**, pp. 2353–2358, 2007.
3. Aydiner, C. C., J. V. Bernier, B. Clausen, U. Lienert, C. N. Tomé, and D. W. Brown, "Evolution of Stress in Individual Grains and Twins in a Magnesium Alloy Aggregate," *Phys. Rev. B,* **80**, 2, 024113, 6, 2009.
4. Merkel, S., H. R. Wenk, P. Gillet, H. K. Mao, and R. J. Hemly, "Deformation of Polycrystalline Iron Up To 30 GPa and 1000 K," *Phys. Earth Planet. Inter.,* **145**, pp. 239–251, 2004.

FY2011 Proposed Work

The experimental program of FY2011 involves applications of this technique to additional materials of interest, including phase transformation zirconium and cerium. In both cases, the specific orientation relationships and strain/stress at transformation (full tensors) are desired.

Continued development of the software includes exploration of more sophisticated segmentation algorithms, addition of basic crystallography routines for calculating structure factors, optimization of the most computationally intensive functions, and enhancement of the user interface based on feedback from users at APS.

Lagrange Multiplier Embedded Mesh Method

For more information contact:

Michael A. Puso
(925) 422-8198
puso1@llnl.gov

Multiphysics simulations are in growing demand as LLNL's Engineering addresses challenging issues for internal and external customers. One broad class from our national security customers is the effect of blast loadings on structures. Developing appropriate computational technologies continues as an area of active research. Needs exist both to simplify the model generation for the user and to increase the robustness and accuracy of the numerical techniques. Furthermore, we wish to leverage the breadth of LLNL's simulation codes and seek approaches that will effectively combine multiple codes' strengths to work in concert on a single, overall problem.

Project Goals

The objective is to develop a new embedded mesh technique for using superposed meshes within a common simulation. Figure 1 shows a simple example where a fluid is flowing past, or through, a moving, deforming solid. The two meshes could be processed by distinct simulation codes. The method can drastically simplify the meshing process as the fluid mesh need not smoothly mate with the surface of a complex structure. Separate meshes for the two physics subdomains can help avoid mesh tangling: simulation termination arising from excess deformation.

We are developing a software tool to accurately interface embedded finite element meshes. This goes beyond most published research that has focused on finite volume techniques common to fluid dynamics. The formulation will have robust numerical stability and as implemented should attain the computational speed expected of an explicitly time integrated program. It should also be extensible to handle different physics and finite element discretizations including Arbitrary Lagrangian-Eulerian (ALE) representations. Two model problems are the focus of this work: fluid-structure interaction and electromagnetics in moving, deforming solids.

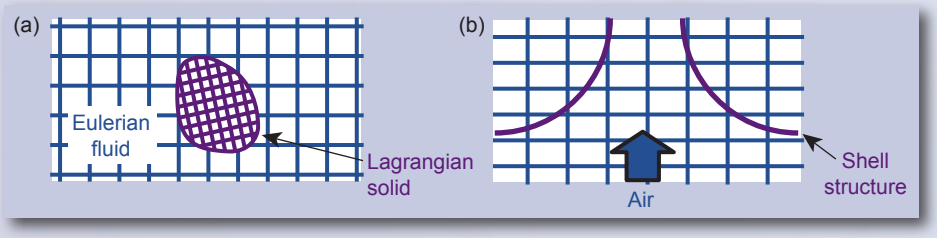

Figure 1. Typical application of the embedded mesh method. (a) A Lagrange solid mesh is moving in an Eulerian fluid mesh. Our software couples the fluid and solid physics across their common boundary. This is particularly helpful when the solid is undergoing large deformations due to loadings from the surrounding fluid (b).

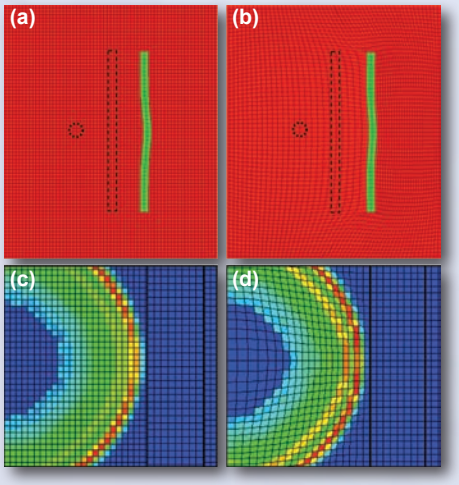

Figure 2. Circular charge placed next to submerged plate. Meshes shown are coarsest used in convergence study. (a) Embedded mesh model with initial plate and charge shown in dotted line. (b) ALE model requiring conformal, common mesh of fluid and solid domains. (c–d) Pressure field arriving at surface of plate for (c) embedded mesh and (d) ALE methods.

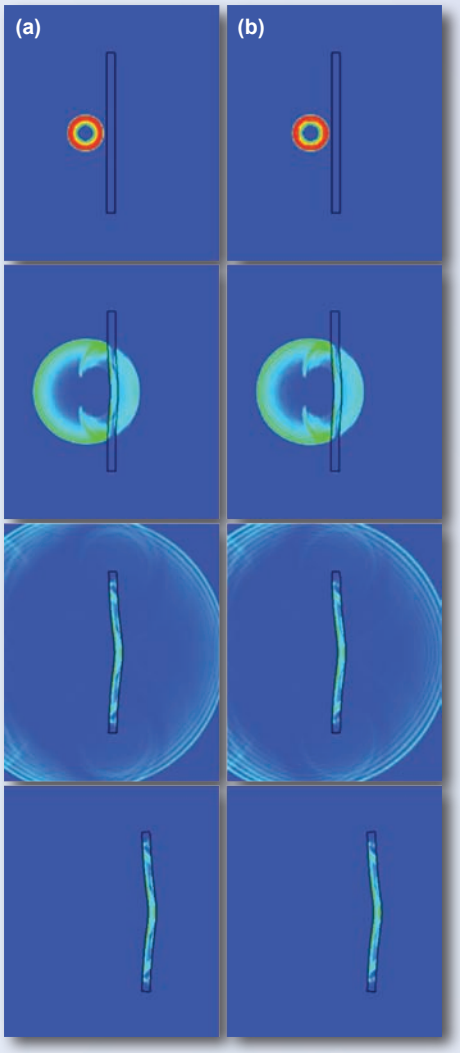

Figure 3. Pressure field in fluid and effective plastic strain in plate for the (a)embedded mesh and (b) ALE simulations at successive, identical times.

Relevance to LLNL Mission

The technologies being developed can support a variety of multiphysics simulations for the Laboratory. The initial focus on blast effects upon structures is consistent with many LLNL national security missions. Its generality will be demonstrated by extension to include fluid-structural-electromagnetic coupling for moving solid conductors such as flux compression generation and rail guns.

FY2010 Accomplishments and Results

We completed the first version of the FEusion software library that identifies the overlap of foreground and background meshes and generates constraints between the solid and fluid regions. The library was ported to three codes: DYNA3D, ALE3D and NIKE3D. In this process we identified and implemented modifications to the ALE3D advection routines for transporting material response quantities between elements. Initial computational results with multiple model problems across all three codes are highly encouraging.

The ALE3D implementation is demonstrated in Fig. 2 where its standard discretization is used as a benchmark for the embedded mesh method. A two-inch-thick steel plate is exposed to an underwater blast and an analysis using the new embedded mesh method (Fig. 2a) is compared to the basic ALE approach (Fig. 2b). Figure 2 shows the coarsest mesh in the study; two additional mesh refinements were made to establish convergence. The embedded mesh exploits an Eulerian mesh of the fluid and a Lagrangian mesh of the plate. The ALE model uses the default ALE3D relaxation with advection in the fluid and a Lagrangian mesh of the plate. The blast bends the plate and forces the plate to flow through the fluid a significant distance (Figs. 2 and 3). While the Eulerian fluid background mesh is stationary, the ALE fluid mesh advects with the moving plate. Figure 4a compares the pressure at the plate surface on the centerline, and Fig. 4b compares the velocity at the center and ends of the plate for embedded mesh and ALE models. Both pressure and displacements match well for long times (10 ms). Figure 4c shows the difference in plate center displacement for different element sizes h and demonstrates that the results appear to converge.

FY2011 Proposed Work

In FY2011, we plan to 1) improve the advection scheme; 2) incorporate a new method for handling potential locking; 3) add a shell element capability; and 4) extend our work to electromagnetic analysis.

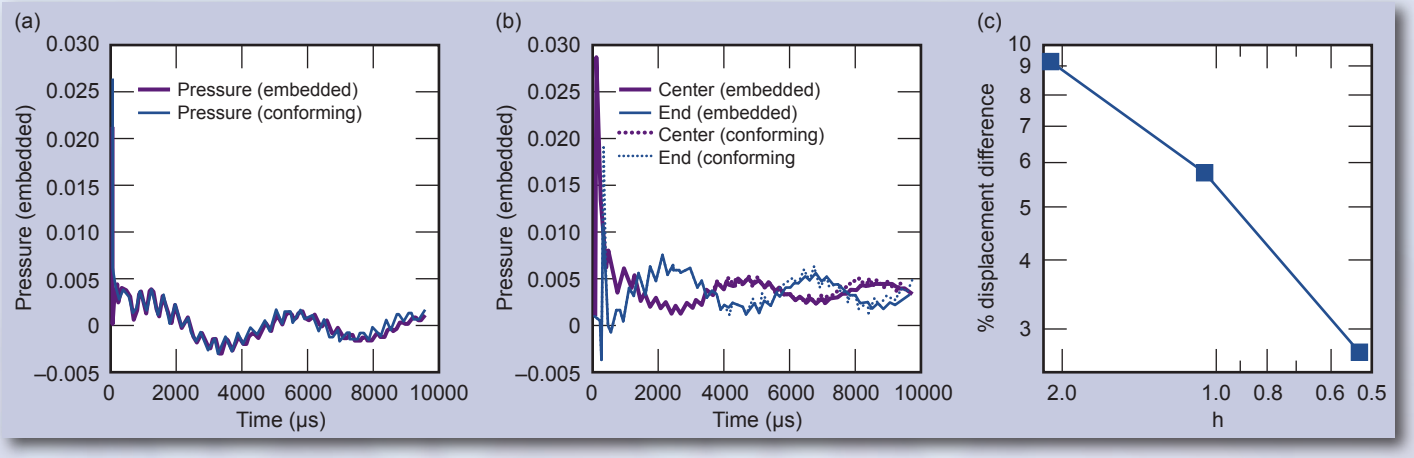

Figure 4. (a) Comparison of centerline pressure in plates. (b) Comparison of displacement at center and ends. (c) Difference in center of mass displacement for three mesh sizes. Results (a–b) are in good agreement and (c) demonstrates some convergence.

Multiscale Polymer Flows and Drag Reduction

For more information contact:

Todd H. Weisgraber
(925) 423-6349
weisgraber2@llnl.gov

Suspensions and polymer solutions exhibit a variety of complex physical phenomena and have applications across multiple disciplines, including blood flow and materials processing. In particular, drag reduction in bounded turbulent flows by the addition of long-chain polymers is a well-established phenomenon. However, despite decades of research, there is still a lack of understanding of the fundamental mechanisms. We believe that a complete description must incorporate wall roughness, a coarse-grained molecular representation of the polymer, and hydrodynamic fluctuations at the polymer length scale.

We are developing new algorithms, including an unconditionally stable, fluctuating lattice-Boltzmann (LB) solver coupled with molecular dynamics (MD), to enable fully turbulent, multiscale simulations of drag reduction.

Project Goals

Our ultimate goal is to perform a series of large-scale simulations of dilute polymer solutions in turbulent flows with a detailed model of the polymer chains and the hydrodynamic interactions. To resolve the relevant scales we are incorporating the following improvements to our existing LB polymer code: 1) enhanced numerical stability; 2) accurate hydrodynamic fluctuations; and 3) integration of the solver with an adaptive mesh refinement (AMR) framework.

Relevance to LLNL Mission

Our research aligns with LLNL's focus on high-performance computing and simulation. Specifically, we seek to address fundamental scientific questions in hydrodynamics. The interaction between flow and suspended macromolecules is also relevant to the development of the next generation of emerging pathogen detection and analysis systems, an important component for the Laboratory's biosecurity strategic mission thrust.

FY2010 Accomplishments and Results

The emphasis during this first year was code development and initial

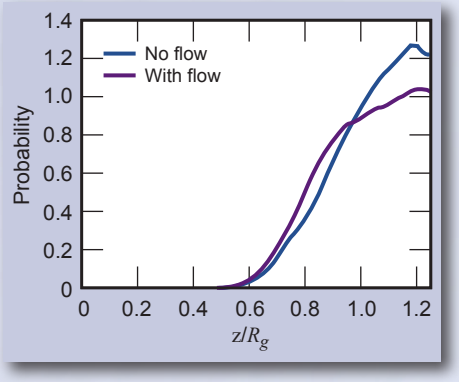

Figure 1. Polymer center of mass distribution in a confined channel with height, h = 2.5R_g, as a function of distance (z) from the lower wall. R_g is the polymer radius of gyration, which is a measure of the average size of the chain. Note the curves are symmetric so only half the channel is shown.

validation. One of the main drawbacks of the LB method is that it becomes unstable for high Reynolds number flows relevant to drag reduction. Fortunately, a new generation of methods, known as entropic LB has overcome this stability issue and we have developed an algorithm for fluctuating hydrodynamics that incorporates these entropic solvers. We have successfully run simulations of turbulent channel flow for Reynolds numbers up to 12,000 using our new solver. These calculations are not realizable with traditional LB methods.

In addition, we performed benchmarking laminar-flow simulations of a single polymer migration in a microchannel using the new entropic code. We want to understand how the polymer will migrate relative to the wall in different flow conditions. In a narrow channel the chain will migrate toward the wall if the flow rate is high enough. Our simulations reproduced this behavior as the shift in the distribution curves of the polymer center of mass in Fig. 1 demonstrates. The blue line is the probability of finding the polymer at a certain height, z, above the lower wall for the case without any flow in the channel. With a flow present, the polymer can stretch and sample regions closer to the wall, as is indicated by the purple line. These results provided additional validation for our algorithm.

One of the key challenges was incorporating mesh refinement for the LB method, which required developing the methodology to transfer information between coarse and fine grids, as shown in Fig. 2. We chose the Chombo library developed at LBNL for the AMR framework. Since LB evolves a discrete velocity distribution function and not the macroscopic hydrodynamic variables (*i.e.*, mass and momentum) the standard finite difference flux conservation approach at grid interfaces was not appropriate. Instead we developed a novel algorithm that minimizes the numerical error associated with refinement. The plot in Fig. 3 compares the errors from both our method and a popular state-of-the-art refinement scheme for a uniformly accelerating flow parallel to the coarse–fine interface. Our error is orders of magnitude lower.

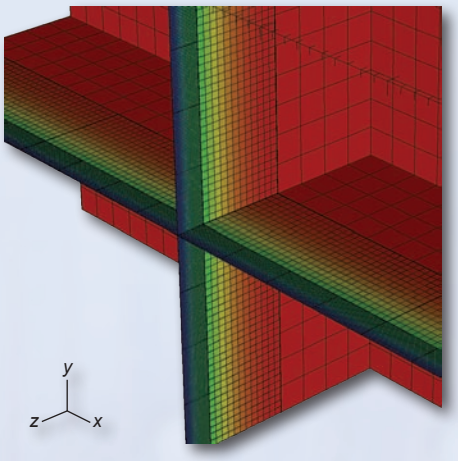

Figure 2. **Example mesh for flow in a channel with grid refinement near the walls.**

Related References

1. Toms, B. A., "Some Observations on the Flow of Linear Polymer Solutions Through Straight Tubes at Large Reynolds Numbers," *Proc. 1st Int. Cong. Rheol.* N. Holland, Amsterdam, **2**, pp. 135–141, 1948.
2. Zhang, Y., A. Donev, T. Weisgraber, B. J. Alder, M. D. Graham, and J. J. de Pablo, "Tethered DNA Dynamics in Shear Flow," *J. Chem. Phys.*, **130**, 23, pp. 234902–234913, 2009.
3. Usta, O. B., A. J. C. Ladd, and J. E. Butler, "Lattice-Boltzmann Simulations of the Dynamics of Polymer Solutions in Periodic and Confined Geometries," *J. Chem. Phys.*, **122**, 2005.
4. Ansumali, S., I. V. Karlin, and H. C. Ottinger, "Minimal Entropic Kinetic Models for Hydrodynamics," *Europhys. Lett.*, **63**, 6, pp. 798–804, 2003.
5. Rohde, M., D. Kandhai, J. J. Derksen, and H. E. A. van den Akker, "A Generic, Mass Conservative Local Grid Refinement Technique for Lattice-Boltzmann Schemes," *Int. J. Numer. Methods Fluids*, **51**, 4, pp. 439–468, 2006.

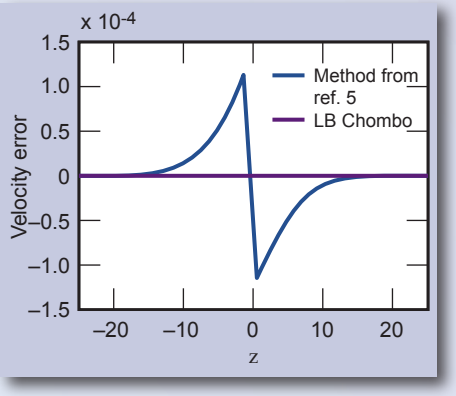

Figure 3. **Mesh refinement error near coarse–fine interface (z=0) for uniformly accelerating flow parallel to the interface. The fine mesh is located at negative z values and the coarse at positive z.**

FY2011 Proposed Work

In FY2011 we plan to: 1) complete the adaptive mesh refinement development; 2) begin Newtonian turbulent channel simulations to validate the AMR code; 3) continue the laminar flow migration simulations with wall roughness; and 4) investigate how many-core graphics processors could accelerate our hybrid LB/MD computations.

Finite Element Analysis Visualization and Data Management

For more information contact:

Bob Corey
(925) 423-3271
ircorey@llnl.gov

Support for and enhancement of several visualization and postprocessing tools is a key component of LLNL's efforts. These tools include the Griz finite element visualization postprocessor, the Mili data management library, and a data file manipulation tool called XmiliCS. These tools are used by engineering analysts and other modelers across the Laboratory to interpret data from a variety of simulation codes such as DYNA, ParaDyn, Nike and Diablo. We also provided support in the area of data translation tools and processes for performing intracode calculations.

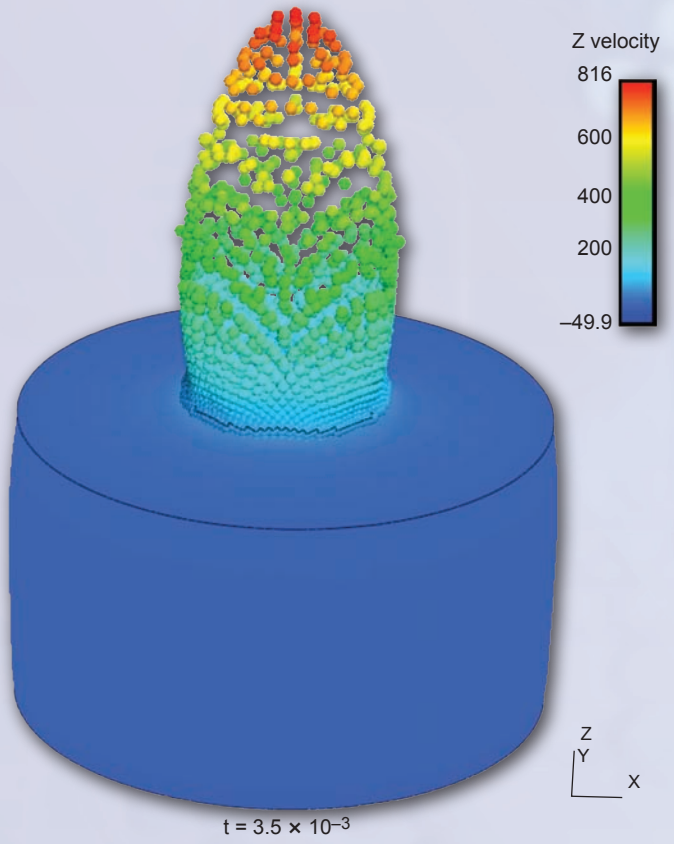

Figure 1. **"Mesh-less" particle representation of soil being ejected by a buried explosive charge, as simulated by ParaDyn. Griz is being extended to support additional types of discretization technologies.**

Griz is our primary tool for visualizing finite element analysis results on 2- and 3-D unstructured grids. Griz provides advanced 3-D visualization techniques such as isocontours and isosurfaces, cutting planes, vector field display. Functionality is expanding for Smooth Particle Hydrodynamics (SPH) and other "mesh-less" modeling entities. Mili is a high-level mesh I/O library intended to support computational analysis and post-processing on unstructured meshes. It provides the primary data path between analysis codes and visualization tools such as Griz. Mili databases are also viewable with the LLNL VisIt postprocessor. XmiliCS is a utility used to combine results from multiple processors that are generated by our large parallel computing platforms.

Project Goals

The project provides ongoing user support and software maintenance for LLNL's visualization and postprocessing tools and adds new capabilities to these tools to support evolving, multiprogrammatic requirements.

Relevance to LLNL Mission

These postprocessing tools provide important user interfaces for LLNL's engineering simulation capabilities and are critical elements in our tool suite. Analysts would be severely limited in their ability to interpret the vast amounts of data generated by simulation and to synthesize key results without graphical representations providing interactive feedback.

FY2010 Accomplishments and Results

Our baseline commitment to LLNL users, the annual release of updated production software, was achieved with the issue of Version 10.1 of Griz, Mili, and XmiliCS. This is a necessary complement to annual releases of the DYNA3D and ParaDyn simulation tools. The growing "mesh-less" capability in those codes for representing highly deforming material creates new needs for support from the visualization and data management tools. Figure 1 provides an example of how Griz provides color contour plots of basic solution quantities over the ensemble of material points used in a "mesh-less" scheme. Efforts are now underway to robustly extend Griz's capabilities for standard continuum elements, *e.g.*, cutting planes to expose the interior of a body, to this added simulation option.

We are halfway through an effort to re-architect and re-implement the XmiliCS utility for consolidating the very large results databases created with ParaDyn. This is being used as an opportunity to redefine the boundary between Mili and XmiliCS so that common operations are consolidated in the Mili interface and better leveraged (re-used) by XmiliCS. This major evolution of the products also provides an opportunity to incorporate a dedicated "particle" data type to more specifically support definition of the particle sets arising from the new "mesh-less" simulations.

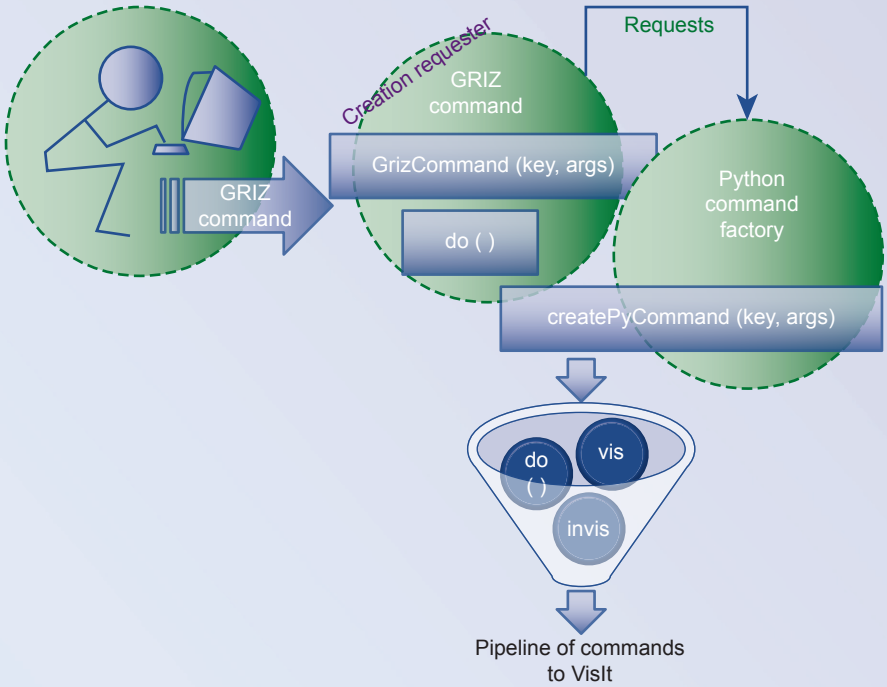

Figure 2. GrizIt Command Line Interface. The common "factory design pattern" software construct provides engineering users with familiar, highly productive ways of accessing and investigating their simulation results while leveraging the high-performance visualization capabilities of the VisIt tool and the flexibility of its Python command interface.

The Laboratory's VisIt data analysis tool is a world-class tool for rendering extremely large scientific data sets. This capability is of interest to engineering analysts as our own models grow, but adoption has been slow because the operational flow of VisIt is so different from that of Griz. We are now creating a capability so users can type the concise commands familiar to them from Griz while the computer automatically issues the more complex stream of multiple instructions required to have VisIt generate the specific image the user desires. We have named this lightweight add-on *GrizIt*. A modern object-oriented design (Fig. 2) allowing for flexible class manipulation and reusable code will permit the set of commands supported to smoothly expand. Proof of concept has been demonstrated and a number of specific commands have been implemented.

FY2011 Proposed Work

Targets for next year include 1) delivering the new XmiliCS combiner tool; 2) having a user-testable ("beta") version of GrizIt exercised sufficiently to support a decision on delivery with Version 11.1 of the ParaDyn Suite; and 3) initial operational capability for end-to-end regression testing of the ParaDyn Suite workflow.

Modeling Enhancements in DYNA3D

For more information contact:

Jerry I. Lin
(925) 423-0907
lin5@llnl.gov

The explicit finite element code DYNA3D is a main Engineering tool for simulation of the transient response of structures to fast, impulsive loadings. Its use has extended beyond our historical core mission to broader applications, such as infrastructure vulnerability and protection analysis, vehicle impact simulation, and integrity assessment for various structures. The code also serves as the mechanics foundation of the highly parallel ParaDyn simulation tool. This project represents an institutional investment in the continued usability and vitality of DYNA3D.

Project Goals

This project funds the ongoing implementation of user-requested features, general technical support, documentation updates, and Software Quality Assurance (SQA) compliance for DYNA3D. It also supports Collaborator Program activities. The Collaborator Program grants selected users licensed access to LLNL's computational mechanics/thermal codes in exchange for their results and acknowledgement. These collaborative members include our sister laboratories, U.S. government agencies, and other education/research institutions.

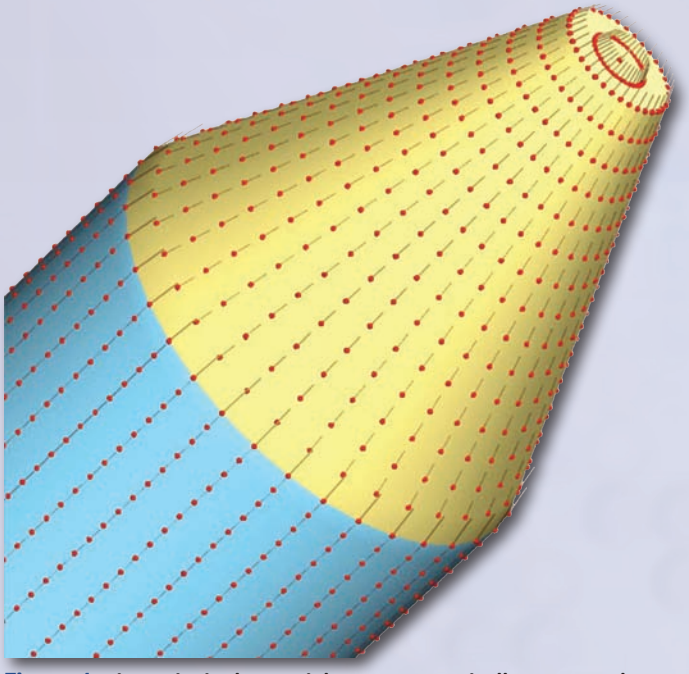

Figure 1. First principal material axes automatically generated at points of a generic conical/cylindrical structure. The dots represent mesh points and the line segment the orientation of the local material axis.

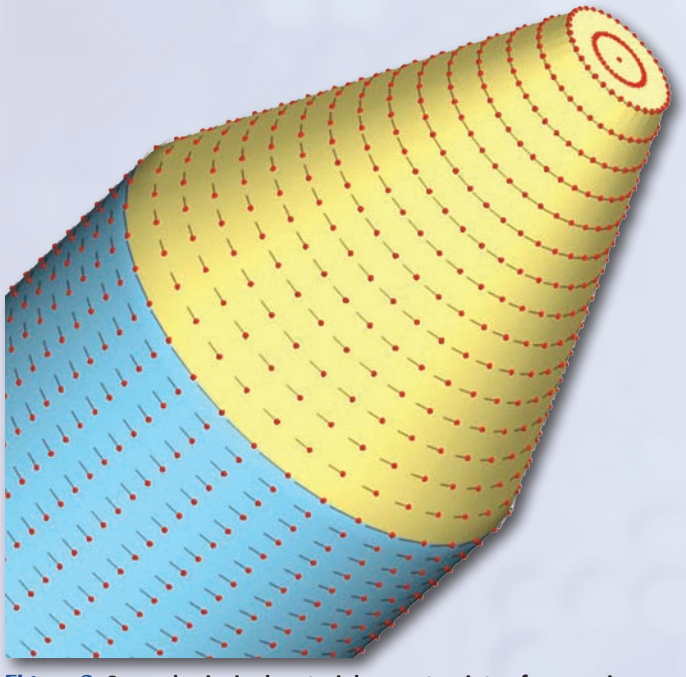

Figure 2. Second principal material axes at points of a generic conical/cylindrical structure, locally orthogonal to the axes shown in Fig. 1.

Relevance to LLNL Mission

Engineering analysts supporting a variety of programs require new structural modeling functionalities and technical support to complete their missions. Some of these programs and projects involve the Laboratory's collaboration with other institutions and federal agencies, including the Los Alamos National Laboratory (LANL), the Missile Defense Agency, the Naval Surface Warfare Center, the U.S. Army Corps of Engineers, and the Department of Homeland Security.

FY2010 Accomplishments and Results

The use of composite materials such as graphite-epoxy has risen significantly in structures and protective gear. Fiber-reinforced materials are typically anisotropic, having non-uniform mechanical and thermal behaviors in different directions. For model preparation involving these materials, one of the great hindrances is assigning local material directions at the various locations throughout the material. For parts of special geometric shapes that align with the material directions, computational algorithms can be created to automatically calculate the material orientations.

Two such geometric configurations, conical and ellipsoidal, were added to the existing choices for all anisotropic continuum materials in DYNA3D. Figures 1 and 2 depict the automatically generated two principal material axes, the first one along the structure longitudinal direction and the second along the transverse direction, at points of a merged conical/cylindrical part.

The drive to model more extreme structural deformations requires sustained investment in additional numerical representations in DYNA3D. One option mechanical analysts have found useful for high-speed impacts is Smooth Particle Hydrodynamics (SPH). This technique approximates material behavior by tracking a set of discrete points and assessing the local stress state in the body via their relative motions.

Figure 3 shows a simple example of two bars striking end-on-end. We are leveraging an SPH capability originally created as a standalone code at LLNL. During its prove-in phase, the module remained nearly a separate code as it used an independent (small) input file and output a separate visualization database. The capability is now more seamlessly integrated from a user perspective as the SPH input parameters are defined within the DYNA3D input file. Similarly, the response quantities computed within the SPH region are now written as part of the standard DYNA3D output database. This both simplifies the collection of files the analyst must manage and facilitates visualization and interpretation of the simulation results.

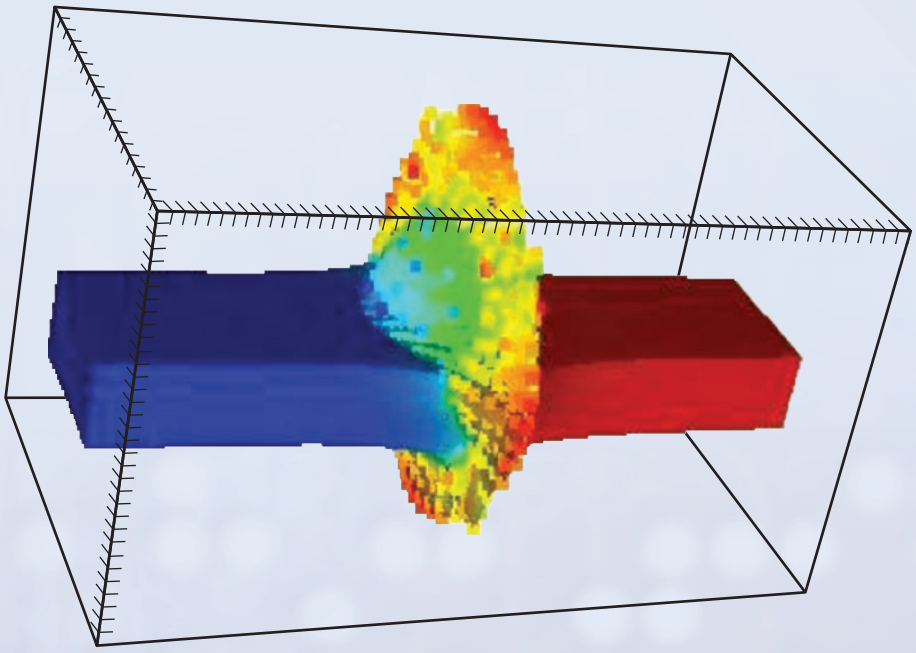

Figure 3. Hopkinson bar high-speed impact modeled with the SPH option now integrated with DYNA3D.

FY2011 Proposed Work

General technical support for DYNA3D users, the addition of user-requested capabilities, and SQA-compliance work will continue under FY2011 funding. For users modeling more complex shapes constructed of anisotropic materials we are introducing a general auxiliary file that can be read for the local material orientation specifications. This will free them to write or adapt small, problem-specific utilities.

Code modifications leading to a completely keyword driven input file will continue as our goal is to provide users with a more conveniently read and modified problem specification. We will use a regression test suite traceability matrix completed in FY2010 to guide and prioritize further test problems to assure performance and stability of DYNA3D's features.

NIKE3D Enhancement and Support

For more information contact:

Michael A. Puso
(925) 422-8198
puso1@llnl.gov

The objective of this work is to enhance, maintain and support LLNL's implicit structural mechanics finite element code, NIKE3D. New features are added to accommodate engineering analysis needs. Maintenance includes bug fixes and code porting to the various platforms available to engineering analysts. User support includes assisting analysts in model debugging and general analysis recommendations.

Project Goals

Ongoing code enhancement requires new features to meet our engineering community's user demands. The following are highlights for FY2010:

1. Add and benchmark a new threaded, distributed memory direct equation solver;
2. Port a prototype model for high explosive deformation under long-term loading, and made significant modifications for fast computation; and
3. Add diagnostics to evaluate sources of rigid body motion.

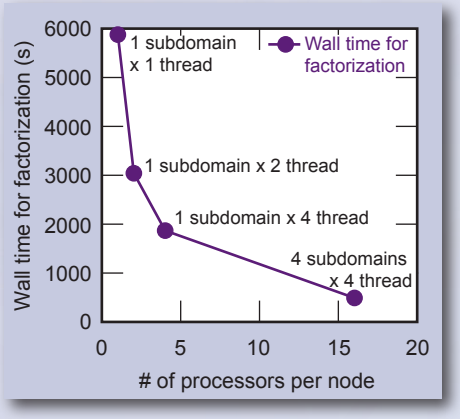

Figure 1. Results from 6-million-element model run on 256 nodes of a Linux high-performance Linux cluster (Hera).

Relevance to LLNL Mission

Structural analysis is one of the most important functions of Engineering and the in-house maintenance, support, and code enhancement we provide for our suite of codes is crucial for meeting engineering's analysis needs. NIKE3D, in particular, is a premier code for handling difficult nonlinear static structural analysis problems.

FY2010 Accomplishments and Results

In contrast to explicit finite element codes like DYNA3D, implicit codes require the solution of systems of coupled linear equations that are typically the bottleneck in large calculations. Many national laboratory implicit codes rely on iterative solvers solely, whereas NIKE3D and Diablo include a highly robust and fast distributed memory parallel direct linear solver (WSMP). We find the direct solver is often the desired approach in many applications due to reliability and speed.

The biggest drawback to using direct solves is the required memory. The typical strategy to achieving large memory is to run the analysis on as many nodes of a parallel computer as necessary. To further economize memory usage, one to four subdomains per node are used for very large analyses (*i.e.,* greater than

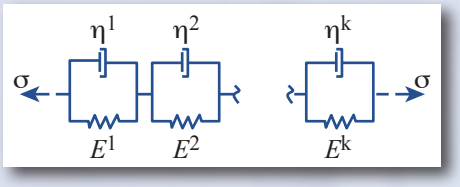

Figure 2. A Kelvin-Voigt spring damper model for visoelastic-plastic response.

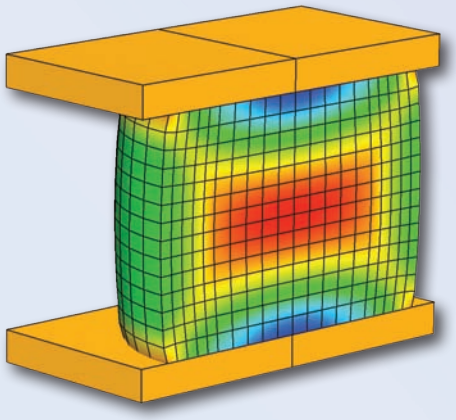

Figure 3. Cylindrical creep specimen for a constant load test.

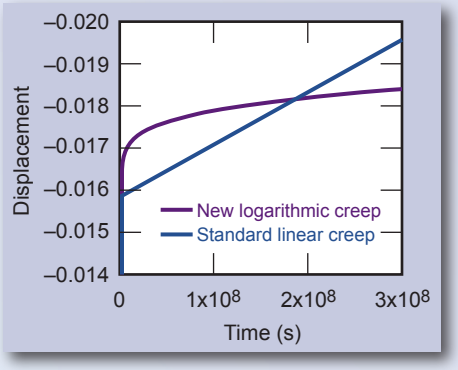

Figure 4. Top displacement of creep cylinder versus time. Note logarithmic response of new creep model compared to classical creep model (Model 27).

1 million elements). Unfortunately, this approach sacrifices processing power for memory. To alleviate this, the Linux version of the WSMP solver in NIKE3D and Diablo has recently been upgraded to include threaded parallelism. This capability has been available for sometime with the AIX version. Now one, two, or four subdomains can be specified on machines such as LLNL's Hera or Juno, and each subdomain can run with multiple threads.

An example showing the factorization times for a 6-million-element analysis is shown in Fig. 1. It should be emphasized that only the linear solver is parallel in the NIKE3D code, whereas Diablo is fully parallel.

A nonlinear creep model for plastic bonded explosive was added to the production version of NIKE3D. While porting the model, a significant effort was made to make it more efficient. The model uses a nonlinear Kelvin-Voigt type spring-damper model with many dependent spring and damper components to capture recoverable creep (Fig. 2). The basic 1-D model is nonlinear:

$$\sigma + c\sigma^2 = E^i\varepsilon^i + \eta^i\dot{\varepsilon}^i \qquad (1)$$

where $\dot{\varepsilon}^i$ represents the i^{th} strain (spring displacement), and E^i, η^i are the spring and damper stiffnesses. The total strain for the Kelvin-Voigt system plus an additional history-dependent, nonrecoverable creep strain ε^{nr} is given by:

$$\dot{\varepsilon} = \sum_{i=1}^{k} \dot{\varepsilon}^i + \dot{\varepsilon}^{nr}(\sigma,t). \qquad (2)$$

Nonrecoverable implies that the strain is fixed after the unloading (*i.e.*, $\sigma \rightarrow 0$).

Time integration of (1) while evaluating (2) requires many computations, including exponential function evaluations. Appropriate compiler options cut CPU time in half for the model. OpenMP was then used to apply threaded parallelism to the material model. A small example (Fig. 3) has a constant 2-ksi load held over 15 years (150 time steps). Figure 4 shows the resultant creep strain to be logarithmic in time as is characteristic with many materials over long time spans. Standard "viscoplastic" creep models are typically linear in time and are thus not valid over such long duration. The original material implementation required 1400 s of wall time, whereas the new threaded parallel version required 114 s of wall time using 16 threads.

FY2011 Proposed Work

In FY2011, our plans include 1) supporting engineering analysts using NIKE2D; 2) modularizing material models for ultimate migration into DIABLO; and 3) upgrading quasi-Newton solver for solution of contact problems.

Electromagnetics Code Enhancement and Maintenance

For more information contact:

Daniel A. White
(925) 422-9870
white37@llnl.gov

LLNL Engineering's EIGER code is a 3-D, parallel, boundary element code for solving Maxwell's equations of electromagnetics (EM). Since EIGER uses a boundary element method (also known as an integral equation method, or method of moments), the EM problem of interest is described by a surface mesh; there is no need to mesh the entire volume. Another advantage of the boundary element method is that it provides an exact radiation boundary condition. The EIGER code is currently being used on several Global Security projects, and can play a large role in possible future work-for-others (WFO) projects.

Project Goals

The goal of this project is to generate an automatic Model Order Reduction (MOR) algorithm for use with EIGER. We are collaborating with staff at Ohio State University. Consider the following example problem: We need to compute electrical currents on cables for 100 different RF frequencies, 100 different angles of incidence, and 100 different cable locations. A brute force approach results in one million distinct EIGER calculations, which is not practical. Automatic MOR is an approach to reduce the total number of calculations by 1) sampling the parameter space; 2) using the samples to build a model of the quantities of interest; and 3) iterating until the model meets a specified accuracy.

Relevance to LLNL Mission

EIGER performs EM analyses that cannot be performed by commercial codes. This allows engineering staff to better support Laboratory programs. Having a unique computational EM capability also provides LLNL a competitive edge when considering additional DOE and WFO projects. Increasing the accuracy and efficiency of our tools benefits all customers.

FY2010 Accomplishments and Results

We created a MOR algorithm, implemented it, and applied it to

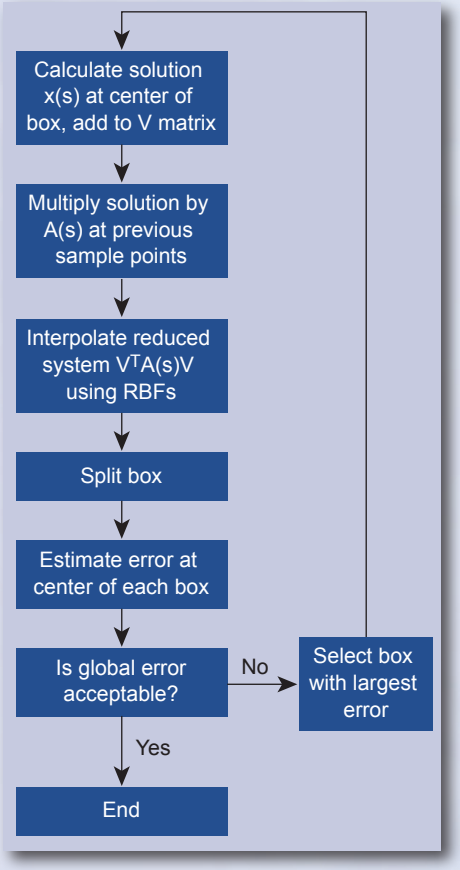

Figure 1. Iterative algorithm for automatic Model Order Reduction. The algorithm performs successive sampling of the original problem space to construct a smaller model having sufficient accuracy to represent all the behavior of interest.

several EM problems of interest to Global Security projects. The outline of the MOR algorithm is as follows.

Let $A(s)\,x = b$ be the boundary element discretization of Maxwell's equations, where $A(s)$ is the $N \times N$ boundary element matrix, x is the vector of unknowns (surface current and charge), b is the source vector, and $s = \{s_1, s_2, \ldots, s_k\}$ is the vector of parameters. The parameters could be, for example, frequency, angle of incidence, material properties, or positions of cables or apertures. The number of unknowns, N, is determined by the computational mesh and can be quite large. $N \approx 10^4$ is common and $N \approx 10^6$ is possible when a fast multiple multipole algorithm is used for the boundary element representation.

The reduced system is given by $a(s) = V^T A(s) V$, where V is a $N \times M$ matrix with $M \ll N$. The columns of V are the basis vectors of the reduced order model, the reduced order model is essentially a "change of basis" resulting in a significantly more compact representation than the full model. The reduced system is evaluated at M sample points (M different values of the parameter vector s); between sample points the reduced system is defined by linear interpolation using Radial Basis Functions (RBF). The basis function expansion is

$$a(s) = \sum_i a_i \phi\left(\left\| s - s_i \right\|\right) + \theta(s)$$

where the RBFs are of the form $\phi(r) = r^{2p}$, and $\theta(r)$ is a polynomial of order p. The coefficients of the basis function expansion are determined by solving a Vandermonde system of equations, this system is only $M \times M$.

The process of choosing the sample points is iterative. The process is like structured adaptive mesh refinement, but in k-dimensional sampling space rather than the physical spatial domain. An error tolerance is specified by the user, and new samples were chosen to minimize the error. The process and an example are shown in Figs. 1 and 2.

As an example, consider the motivating problem of computing electrical currents on cables where a brute force approach would result in one million EIGER calculations. Using the automatic MOR algorithm outlined above, we were able to completely explore this parameter space to within an error of 1% by performing only about 800 EIGER calculations, a reduction of over 1000 ×. It is also important to note that the MOR software implementation is parallel. The EIGER calculations were executed using 8 nodes (32 processors) and completed in just one day.

Related References

1. Sharpe, R., *et al.,* "EIGER: Electromagnetic Interactions Generalized," *IEEE Ant. Prop. Int. Symp.,* pp. 2366–2369, July 1997.
2. Buhmann, M. D., "Radial Basis Functions," *Acta Numerica,* **9**, pp. 1–38, 2000.

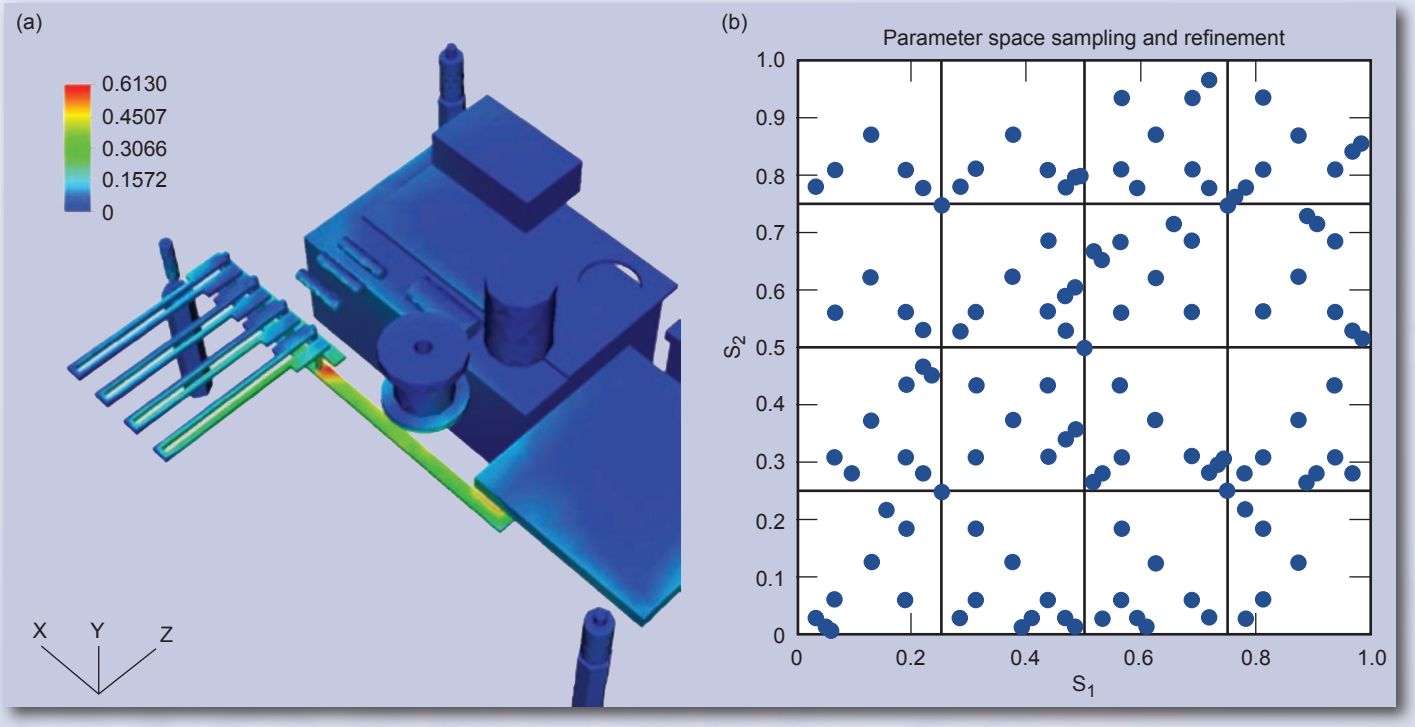

Figure 2. Example calculation using our automatic Model Order Reduction algorithm. (a) Current density computed on a circuit for a single combination of two input parameters, s_1 and s_2. (b) Graphic showing the limited number of cases sampled in the plane needed to capture the behavior over the entire parameter range.

Micro/Nano-Devices & Structures

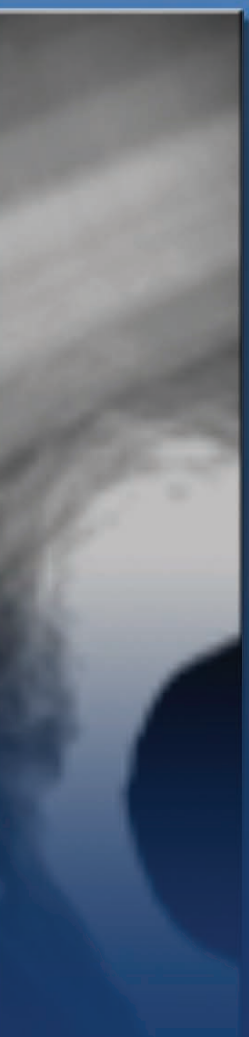

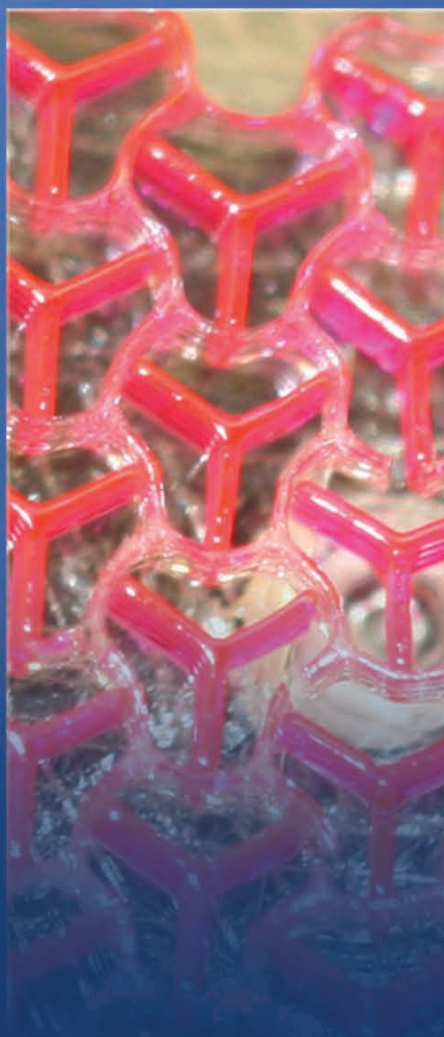

Hybridization, Regeneration, and Selective Release of DNA Microarrays

For more information contact:

Elizabeth K. Wheeler
(925) 423-6245
wheeler16@llnl.gov

DNA microarrays contain sequence-specific probes arrayed in distinct spots numbering from 10,000 to over 1,000,000, depending on the platform. This tremendous degree of multiplexing gives microarrays great potential for environmental background sampling, broad-spectrum clinical monitoring, and continuous biological threat detection. In practice, their use in these applications is not common due to limited information content, long processing times, and high cost.

Our work seeks to characterize the phenomena of microarray hybridization, regeneration, and selective release that will allow these limitations to be addressed. This will revolutionize the ways that microarrays can be used for LLNL's Global Security missions.

One study area is selective release. Microarrays easily generate hybridization patterns and signatures, but there still is an unmet need for methodologies enabling rapid and selective analysis of these patterns and signatures. Detailed analysis of individual spots by subsequent sequencing could potentially yield significant information for rapidly mutating and emerging (or deliberately engineered) pathogens. In the selective release work, optical energy deposition with coherent light is being explored to quickly provide the thermal energy to single spots to release hybridized DNA.

The second study area involves hybridization kinetics and mass-transfer effects. The standard hybridization protocol uses an overnight incubation to achieve the best possible signal for any sample type, as well as for convenience in manual processing. There is potential to significantly shorten this time based on better understanding and control of the rate-limiting processes and knowledge of the progress of the hybridization. In the hybridization work, a custom microarray flow cell will be used to manipulate the chemical and thermal environment of the array and image the changes over time during hybridization.

Project Goals

The goals of the selective release work are to characterize the phenomena involved in high-resolution energy

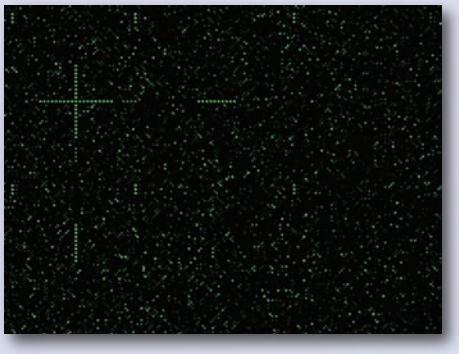

Figure 1. Detail image of a microarray scan after autonomously hybridizing *E. coli, E. faecalis,* and *S. aureus* on the Virulence Array.

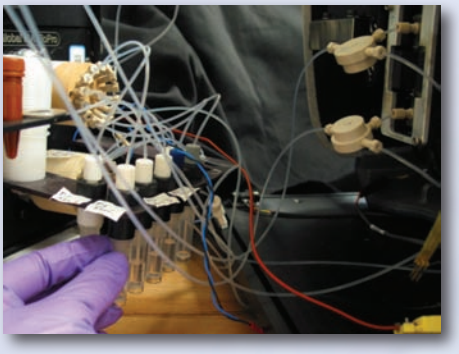

Figure 2. R&D system, showing user loading sample vial onto system prior to beginning integrated hybridization experiments. The microarray flow cell shown on right hand side is connected to fluidics lines.

deposition with an IR laser and to demonstrate selective release of DNA from a microarray. This includes assessing the effects of wavelength, absorption, spot size, materials, pulse energy, and fluid flow.

The goal of the hybridization work is to quantify the rate-limiting processes in microarray hybridization and to demonstrate improvement in hybridization time by controlling the process.

Relevance to LLNL Mission

LLNL has ongoing efforts in detection methods against biological terrorism. The next stage of molecular diagnostics for biological threats is to look much more broadly for emerging threat bio-signatures, such as virulence elements or natural and engineered mutations. This capability is targeted against new natural pandemics and engineered biological warfare agents, while still detecting the full set of known bio-threat agents, to enable prompt countermeasures.

FY2010 Accomplishments and Results

We extended the DNA Release and Capture Laser (DRACULA) to a multiple wavelength system allowing spot size reduction as well as more uniform energy deposition in the fluid column due to the absorption wavelength dependency. We have conducted thermal energy deposition tests to calibrate the elution temperature. Since we do not want to elute all DNA hybridized to the array, we had to investigate non-standard aqueous elution solutions. To quantify how much DNA is selectively released, we have developed a quantitative PCR assay for off-line detection of eluted oligonucleotides for selective release and demonstrated high sensitivity.

For the hybridization platform, we developed the software needed to translate the bench top process to the integrated automated system. Most importantly, we performed our first integrated flow-cell hybridization experiment with a biological sample of *E. coli, E. faecalis,* and *S. aureus,* using the LLNL Virulence Array. Analysis of the data taken at different time points during the hybridization is ongoing with the analysis tool that we developed this year. Also an array to study the kinetics of hybridization has been designed and is in the process of being fabricated, ready for testing in FY2011.

Figures 1 through 4 illustrate the results of our work.

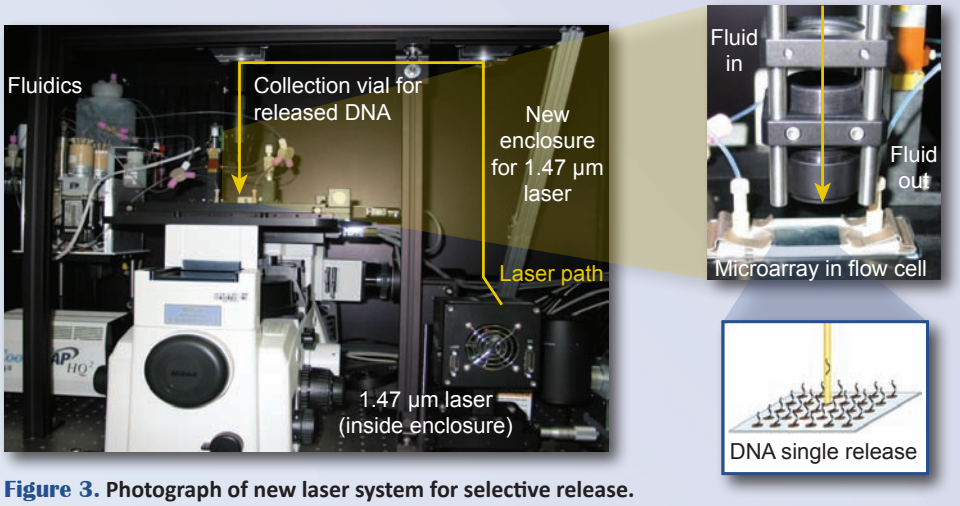

Figure 3. **Photograph of new laser system for selective release.**

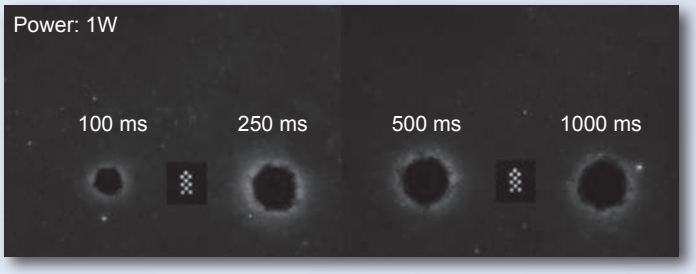

Figure 4. **Characterization of pulse power and duration on spot size for new laser system.**

Related References

1. Jain, C., S. Gardner, K. McLoughlin, N. Mulakken, M. Alegria-Hartman, P. Banda, P. Williams, P. Gu, M. Wagner, C. Manohar, and T. Slezak, "A Functional Gene Array for Detection of Bacterial Virulence Elements," PLoS ONE, **3**, 5, e2163, 2008.

2. Wang, D., A. Urisman, Y. Liu, M. Springer, *et al.*, "Viral Discovery and Sequence Recovery Using DNA Microarrays," PLoS Bio., **1**, pp. 257–260, 2003.

3. Wang, Z., L. T. Daum, G. J. Vora, D. Metgar, E. A. Walter, L. C. Canas, A. P. Malanoski, B. Lin, and D. A. Stenger, "Identifying Influenza Viruses with Resequencing Microarrays," *Emerging Infectious Diseases*, **12**, 4, pp. 638–646, 2008.

FY2011 Proposed Work

For selective release, the key milestone will be release, capture and quantification of an undamaged SARS target. After the initial demonstration of selective release, we will focus on characterizing the effects of laser power and fluid flow conditions on release selectivity and yield. After the initial characterization of hybridization rates using an artificial kinetics array, the hybridization experiments will determine rates using biological samples on the LLNL Virulence Array.

Cadmium–Zinc–Telluride Sandwich Detectors for Gamma Radiation

For more information contact:

Adam M. Conway
(925) 422-2412
conway8@llnl.gov

Detectors to sense the presence of nuclear and radioactive weapons concealed in transit through borders, airports, and seaports are crucial for the international struggle against terrorism and the proliferation of weapons of mass destruction. Currently, high purity germanium detectors offer the best performance in detecting gamma rays; however, they must be operated at cryogenic temperatures.

A room-temperature detector is greatly preferred because of cost and ease of use, but the only available alternative is based on cadmium zinc telluride (CZT) technology, which offers inferior performance. Here we propose a pathway for CZT gamma detectors to achieve the desired energy resolution of better than 1% at 662 keV. We will use a multilayered structure, as shown schematically in Fig. 1, to allow signal collection while simultaneously rejecting noise. By applying energy bandgap engineering to CZT gamma detectors, we believe detector performance can be improved.

Project Goals

With this project, we expect to demonstrate a pathway toward a gamma detector with better than 1% at 662 keV energy resolution that will operate at room temperature. To achieve this goal, we will design a novel structure using bandgap engineering concepts that will result in a 90% reduction in leakage current (which is the dominant noise mechanism at the energies of interest) relative to a resistive device. We will also provide leadership to the detector community through a technical roadmap for the demonstration of a 0.5% (at 662 keV) energy resolution within five years.

Relevance to LLNL Mission

The solution to the radiation-detector materials problem is expected to have significant impact on efforts to develop detectors that are compact, efficient, inexpensive, and operate at ambient temperature for the detection of special nuclear materials as well as radiological dispersal devices. The

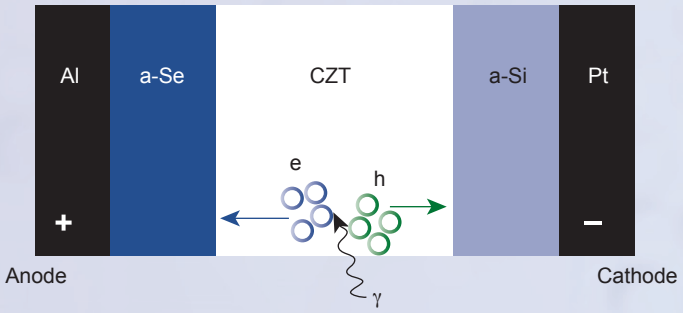

Figure 1. Schematic diagram of a-Se/CZT/a-Si detector layer structure.

multidisciplinary nature of this work and the relevance to national and homeland security align well with LLNL capabilities and missions.

FY2010 Accomplishments and Results

Over the course of this project we have 1) developed finite element modeling capabilities for amorphous-CZT heterojunctions to understand electronic conduction mechanisms; 2) studied amorphous-CZT heterojunctions using current vs. voltage vs. temperature measurements for characterization of Schottky barrier height; and 3) fabricated amorphous Se-CZT-amorphous Si heterojunction detectors (Fig. 2) that have reduced the leakage current by 100 × resulting in an effective resistivity of greater than 10^{12} ohm-cm in bulk material that is too conductive for typical CZT gamma detectors (Fig. 3); and 4) demonstrated proof-of-principle detectors with improved energy resolution (Fig. 4).

Related References

1. Voss, L. F., P. R. Beck, A. M. Conway, R. T. Graff, R. J. Nikolic, A. J. Nelson, and S. A. Payne, "Surface Current Reduction in (211) Oriented CdZnTe Crystals by Ar Bombardment," *J. Appl. Phys.*, **108**, 014510, 2010.
2. Conway, A. M., B. W. Sturm, L. F. Voss, P. R. Beck, R. T. Graff, R. J. Nikolic, A. J. Nelson, and S. A. Payne, "Amorphous Semiconductor Blocking Contacts on CdZnTe Gamma Detectors," *International Semiconductor Device Research Symposium*, December 2009.
3. Voss, L. F., A. M. Conway, B. W. Sturm, R. T. Graff, R. J. Nikolic, A. J. Nelson, and S. A. Payne, "Amorphous Semiconductor Blocking Contacts on CdTe Gamma Detectors," *IEEE Nuclear Science Symposium*, October 2009.
4. Nelson, A. J., A. M. Conway, C. E. Reinhardt, J. J. Ferreira, R. J. Nikolic, and S. A. Payne, "X-Ray Photoemission Analysis of CdZnTe Surfaces for Improved Radiation Detectors," *Materials Lett.*, **63**, 180, 2009.

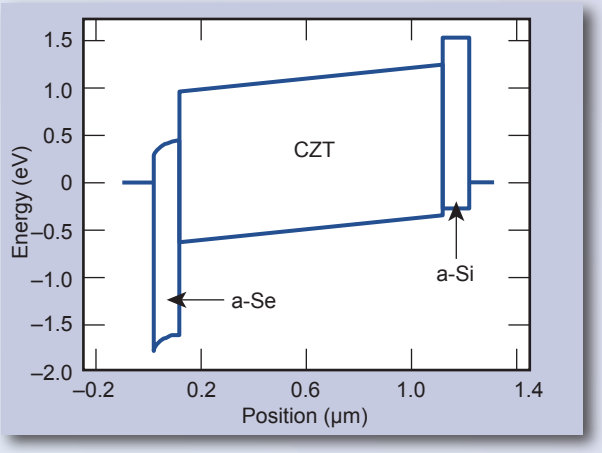

Figure 2. Simulated energy band diagram of a-Se/CdZnTe/a-Si:H layered structure.

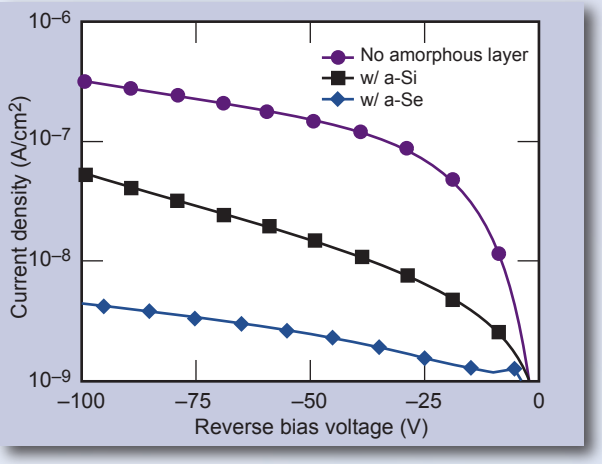

Figure 3. Comparison of current versus voltage characteristics with and without amorphous contacts.

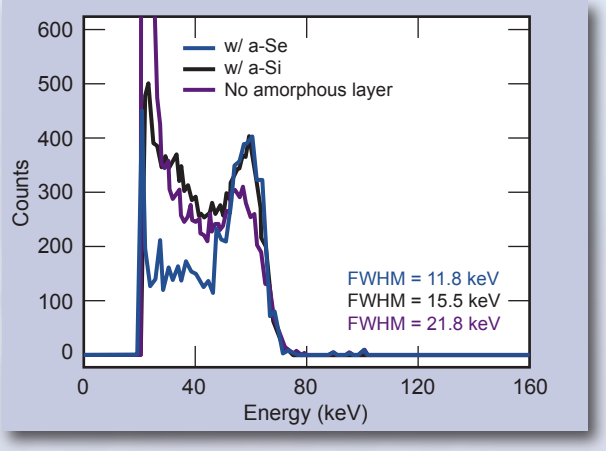

Figure 4. Comparison of Am-241 gamma spectra with and without amorphous contacts.

Enabling Transparent Ceramic Optics with Nanostructured Materials Tailored in Three Dimensions

For more information contact:

Joshua D. Kuntz
(925) 423-9593
kuntz2@llnl.gov

We are developing a novel nanomanufacturing technique, based on the electrophoretic deposition (EPD) process, to create transparent ceramic optics with unique properties based on tailored nanostructures. The EPD process uses electric fields to deposit charged nanoparticles from a solution onto a substrate. We are expanding current EPD capabilities to enable controlled deposition in three dimensions by automating the injection of nanoparticle suspensions into the deposition chamber and dynamically modifying the electrode pattern on the deposition substrate. We can also use the electric field to control the orientation of nonspherical particles during deposition to orient grain structures prior to sintering.

To enable this new functionality, we are synthesizing ceramic nanoparticles as our precursor material, implementing new instrumentation for the benchtop deposition experiments, and developing modeling capabilities to predict deposition kinetics and deposited structures based on the particle, solution, and system properties.

To guide our research and development efforts, we have identified transparent ceramic optics as a major area in which nanostructured functionally graded materials can have a significant impact. Laser physicists and optical system engineers are currently hindered by the small subset of materials available for their designs. The only crystalline materials open to them are those that can be grown as single crystals and isotropic cubic materials that can be formed into transparent ceramics. By depositing nanorods of a noncubic material in the same orientation, the resulting green-body can theoretically be sintered to a transparent ceramic. Additionally, current optics designs are material- and process-limited to uniform composition profiles across optical components and laser gain media. To date, only coarse step function composition changes have been produced in the most advanced transparent ceramic optics. Our EPD platform will enable us to create new transparent ceramic optics with doping profiles tailored in three dimensions.

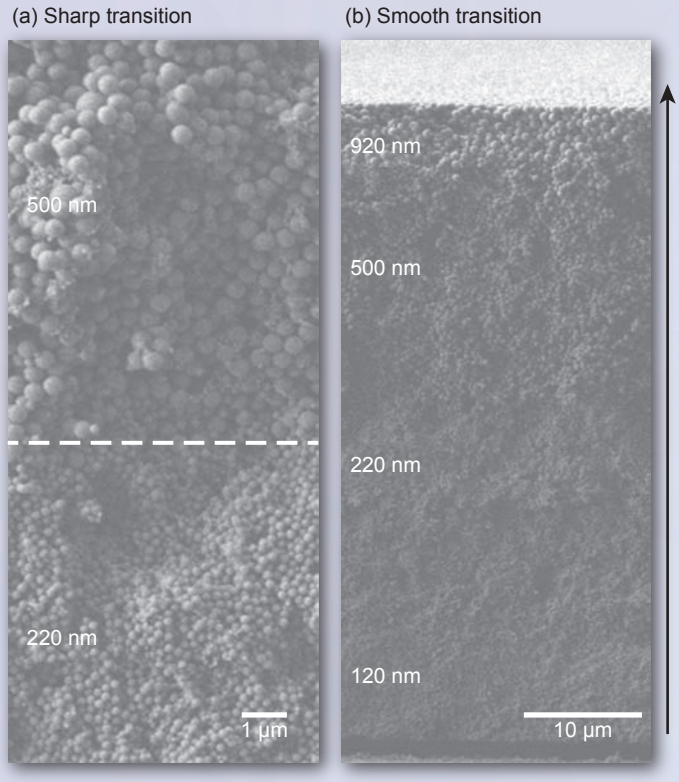

Figure 1. Examples of multilayer films deposited with either (a) sharp or (b) smooth transitions between material layers.

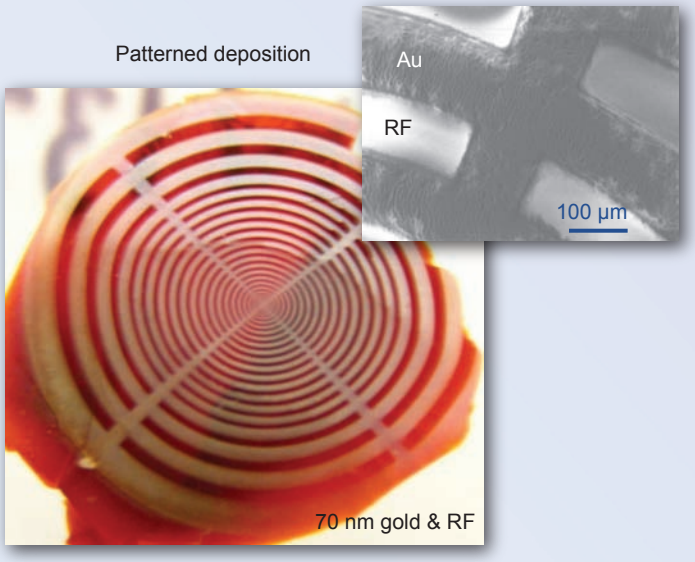

Figure 2. Deposition of 70-nm gold particles onto a fixed electrode pattern that is gelled *in situ* using resorcinol formaldehyde (RF). The white areas are gold and the red areas are the gelled RF. Minimum feature size at the center of the pattern is approximately 10 µm.

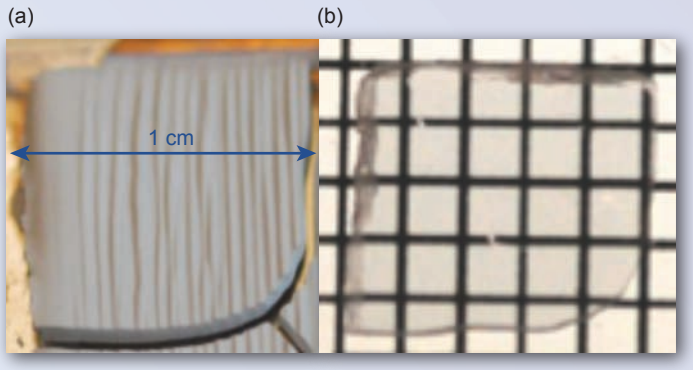

Figure 3. Example of a transparent ceramic fabricated using EPD. The ceramic material is Nd:GYSAG and was deposited to a thickness of 1.4 mm in 10 min using a 10-V/mm electric field. The part shown in (a) was vacuum sintered at 1675 °C and then hot isostatically pressed to create the final transparent part (b).

Project Goals

The goals of this project are: 1) demonstrate the fabrication of functionally graded materials with composition profiles tailored in three dimensions while maintaining desired bulk properties; 2) demonstrate the use of the EPD deposition field to simultaneously align nanorod particles of precursor material as they are deposited; and 3) demonstrate the fabrication of composite structures with controlled material composition and create smooth or sharp material transitions along the z-axis of a composite structure.

Relevance to LLNL Mission

The project is intended to establish LLNL leadership in bottom-up nanofabrication of functionally graded materials. Our dynamic EPD system will position us to deliver the next generation of nanomanufacturing capabilities for projects throughout the Laboratory. Using these capabilities, we are working to produce a number of novel materials and structures. These structures will both illustrate the capabilities of the new process and demonstrate materials and structures of relevance to LLNL missions and programs. The main demonstrations for this project align with current and future needs in NIF as well as the LIFE and ALOSA thrust areas. These are: 1) to create transparent ceramic optics with doping profiles tailored in three dimensions to enable new high-powered laser designs (NIF/LIFE); and 2) to deposit aligned nanoparticles of noncubic ceramics to create a new family of transparent ceramics (NIF/LIFE/ALOSA).

FY2010 Accomplishments and Results

Accomplishments and results in the second year include the following:

1. Demonstrated the ability to change material composition and thickness of deposition layers, and created both sharp and gradual material transitions during deposition (Fig. 1).
2. Successfully deposited a 2-D extruded pattern with 10-µm resolution (Fig. 2). The material is deposited onto a photolithographically patterned metal electrode.
3. Developed a new gelation process that enables deposition in an aqueous solution and then "locks in" the pattern by gelling the solution at elevated temperature.
4. Synthesized near-monodisperse fluorapatite nanorods and demonstrated alignment of the rods in a 300-V/cm electric field.
5. Demonstrated transparent ceramic structures fabricated using the EPD process (Fig 3).

FY2011 Proposed Work

In FY2011 we will 1) demonstrate combined orientation and deposition control and fabricate a transparent optic from a noncubic material; 2) implement fixed-mask x-y control and demonstrate a transparent sintered part with a planar composition gradient; and 3) use *in-situ* AFM to monitor the EPD process and validate our process model.

High-Resolution Projection Micro-Stereolithography (PμSL) for Advanced Target Fabrication

For more information contact:

Christopher M. Spadaccini
(925) 423-3185
spadaccini2@llnl.gov

Our objective is to advance the state of the art in 3-D micro- and nanofabrication by using Projection Micro-Stereolithography (PμSL). PμSL is a low cost, high throughput, microscale, stereolithography technique that uses a spatial light modulator (typically a Digital Micromirror Device (DMD) or a Liquid Crystal on Silicon (LCoS) chip) as a dynamically reconfigurable digital photomask.

PμSL is capable of fabricating complex, 3-D microstructures in a bottom-up, layer-by-layer fashion. A CAD model is first sliced into a series of closely spaced horizontal planes. These 2-D slices are digitized in the form of a bitmap image and transmitted to the LCoS. A UV LED illuminates the LCoS, which acts as a dynamically reconfigurable photomask and transmits the image through a reduction lens into a bath of photosensitive resin. The resin that is exposed to the UV light is then cured and anchored to a platform and z-axis motion stage. The stage is lowered a small increment and the next 2-D slice is projected into the resin and cured on top of the previously exposed structure. This layered fabrication continues until the 3-D part is complete. Figure 1 shows a schematic of our system's optical path.

The process has been shown to have the capability to rapidly generate complex 3-D geometries. Applying this concept to LLNL programmatic problems and advancing PμSL capability with respect to these issues constitutes the primary focus of the research. PμSL performance, such as resolution, materials, geometries, and substrates, has been greatly improved.

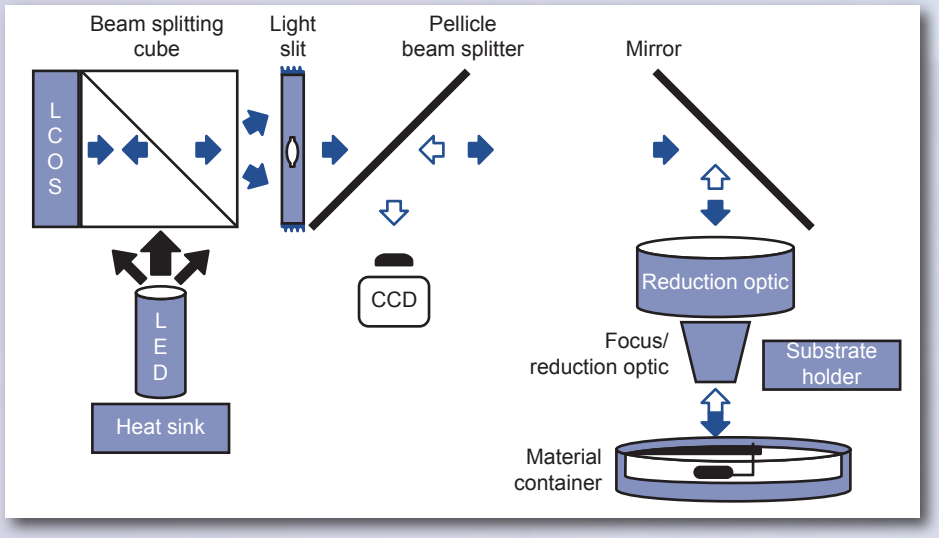

Figure 1. Schematic of PμSL system optical path.

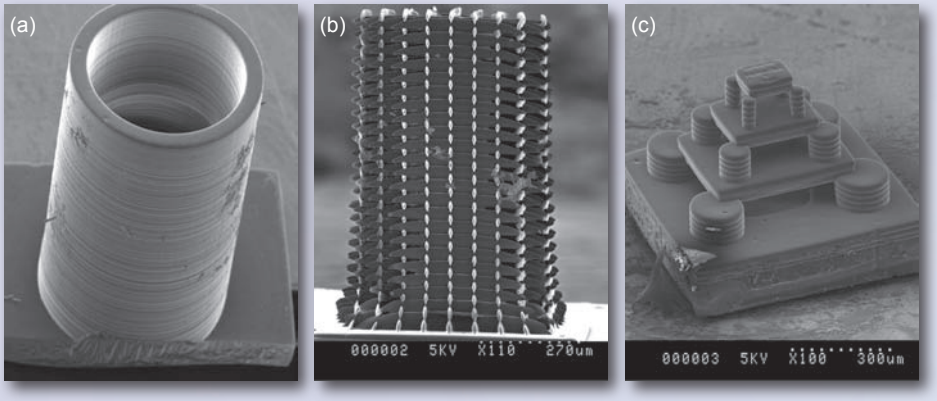

Figure 2. SEM images of (a) cylinders, (b) lattice structures, and (c) 3-D components with overhanging features.

Project Goals

Overall project goals included:

1. Establishing a high functioning PμSL system at LLNL that can produce 3-D components on demand.
2. Improving the resolution of this system by integrating a plasmonic superlens.
3. Broadening the range of materials that can be used with PμSL to

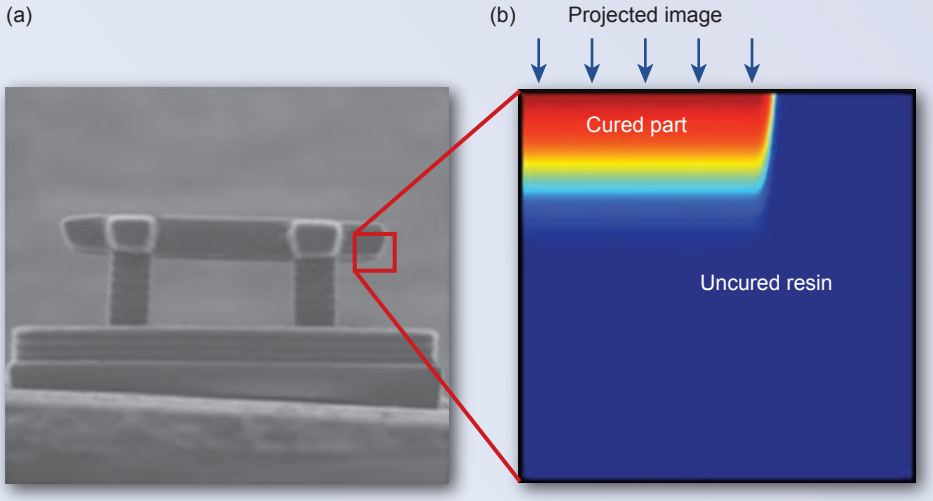

Figure 3. **(a) Fabricated structure next to (b) predicted polymerization profile from numerical model.**

include metals, ceramics and a range of polymers.
4. Establishing a coupled optical-chemical-fluidic model to better understand the physics of the process and to use as a design tool.

Specific goals for FY2010 were:
1. Exercise the LLNL PμSL system to rapidly fabricate 3-D components of interest to the target community.
2. Fabricate and test a plasmonic superlens to demonstrate the capability for improved resolution and begin integration with PμSL.
3. Validate the baseline coupled optical-chemical model by comparing the model's predicted polymerization depths to those measured from parts fabricated with the LLNL system.
4. Include fluid motion in the coupled model to study the impact of moving components in the liquid resin bath.
5. Incorporate microfluidics with PμSL to demonstrate the capability to fabricate with multiple materials.

Relevance to LLNL Mission

Target fabrication for NIF and other stockpile stewardship physics experiments has been a critical factor in limiting the scope of tests that can be conducted. Research efforts across LLNL have focused on developing new fabrication techniques that can generate meso- to microscale targets with micro- to nanoscale precision and features. Although much progress has been made, several key target features have been difficult to achieve and would benefit from advances in 3-D microfabrication techniques.

High resolution PμSL has the potential to directly impact target fabrication limitations and may also be of great benefit to the newly emerging LIFE program at LLNL, which has its own set of challenges. An ancillary impact of this work is to enable a host of new MicroElectroMechanical Systems (MEMS) devices never before conceived due to the rapid, high-resolution, fully 3-D nature of the technique.

FY2010 Accomplishments and Results

Significant progress has been made during FY2010, including:
1. Fabrication of many 3-D components of interest to the target community. Figure 2 highlights some of these pieces including cylinders, lattice structures, and fully 3-D parts with overhanging features. Features as small as 5 μm have been demonstrated.
2. Fabrication and demonstration of a working plasmonic superlens has been accomplished. This superlens device was integrated into a PμSL system. However, the light attenuation as result of the superlens did not allow for any features to be fabricated. As a result, a path to generating subwavelength features includes a stronger light source and a defect-free superlens structure.
3. Validation of the optical-chemical model. Figure 3 shows a fabricated part compared to the predicted geometry from the numerical model. Fluid motion is also incorporated into the model and the movement of the substrate as it is lowered into the resin is captured.
4. A multi-material lattice structure has been generated and is shown in Fig. 4. This demonstrates both the three-dimensionality and the heterogeneous nature of the technique in a single structure and used microfluidic resin delivery and removal systems.

Our success is evidenced by a recent WFO DARPA award where PμSL will be used as one of the fabrication tools for generating Materials with Controlled Microstructural Architectures.

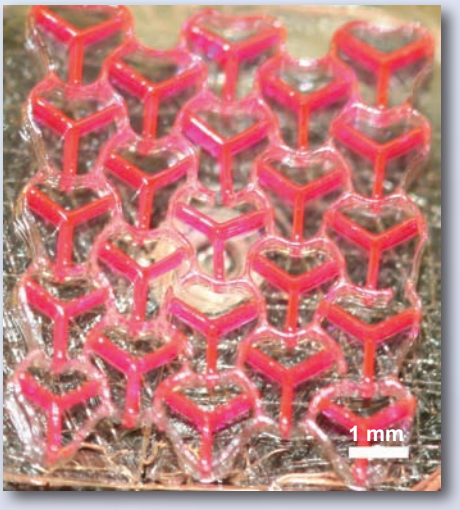

Figure 4. **Lattice of heterogeneous unit cell structures. Two different polymer materials were used in the same structure.**

Three-Dimensional Polymer Fabrication Techniques

For more information contact:

Christopher M. Spadaccini
(925) 423-3185
spadaccini2@llnl.gov

Our objective for this work was to demonstrate the fabrication of several important 3-D polymer shapes of interest to LLNL programs—hollow microspheres and dimple-like structures. This was attempted via two microfabrication techniques: 1) microfluidic-based double emulsions; and 2) wide area, layer-by-layer lithography.

Based on the published literature and guidance from an academic collaborator, we established the capability to generate hollow microspheres in microfluidic channels. Our existing Projection MicroStereolithography System (PμSL) layer-by-layer fabrication tool was used to obtain the dimpled structures.

Project Goals

There were three primary goals for this project: 1) assemble an apparatus for fabrication of microspheres; 2) demonstrate polymeric shell fabrication and encapsulation of liquids; and 3) demonstrate fabrication of dimpled microstructures.

Relevance to LLNL Mission

This project has important programmatic implications for Global Security's E-Program and for the various laser programs at LLNL.

Encapsulating amine solvents in permeable polymer spheres is useful for advanced carbon capture technologies used in E-Program. This technique will enable the use of much higher amine concentrations than is used today, offering the potential to lower costs and improve carbon capture. In addition, assembling a microencapsulation apparatus and demonstrating its use was instrumental in securing WFO funding from ARPA-E for future carbon capture work.

Dimpled meso- and microstructures made from polymer materials provide excellent light scattering surfaces for use in LLNL's optical systems. Smooth surfaces can cause undesirable reflections of laser light in certain experiments and a means of rapidly generating complex, 3-D, dimpled structures for light scattering applications is useful in many experimental configurations.

FY2010 Accomplishments and Results

Microfluidic assembly techniques have recently emerged as a new platform for creating droplets, core-shell beads, polymer particles, colloid-filled granules, and microcomponents of controlled shape, size, and polydispersity.

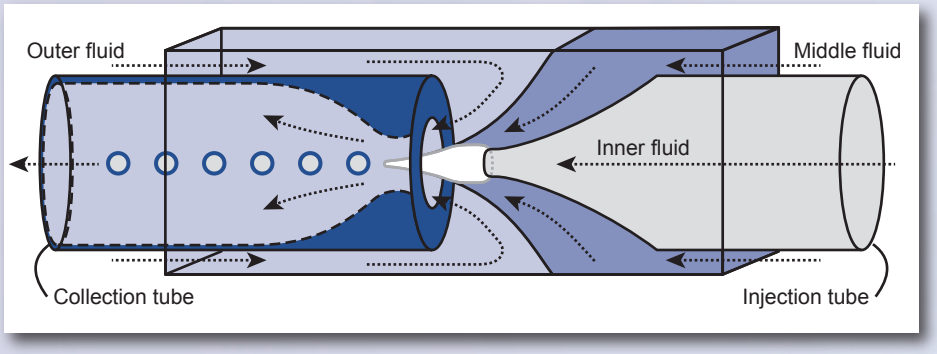

Figure 1. Schematic of flow-focusing microfluidic geometry for microencapsulation.

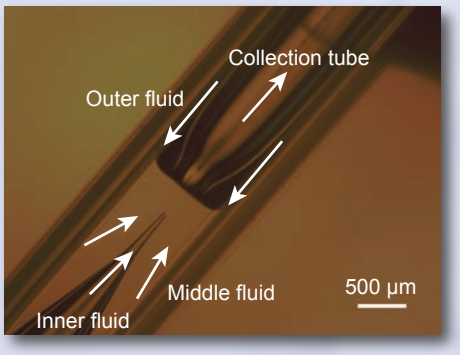

Figure 2. Optical micrograph of microfluidic geometry.

We targeted a microfluidic approach for microcapsule fabrication based on a flow-focusing geometry. We identified this approach because it offers exquisite control of shell diameter and wall thickness, which are important parameters for mass transfer consideration and mechanical robustness. In addition, this approach conserves expensive materials since it encapsulates nearly 100% of the desired solution, which is a significant improvement over other batch processes. In this approach, a tapered capillary nozzle with circular cross-section is aligned within a square capillary (Fig. 1). To do this, the outer diameter of the circular capillary must be approximately equal to the inner diameter of the square capillary. A second circular capillary with a larger opening is inserted into the square capillary from the opposite end, which forces alignment. This configuration allows the flow of three fluids: the inner fluid (to be encapsulated), the middle fluid (the shell material) and the outer fluid, which focuses and pinches off the microcapsule droplets in the collection tube (Fig. 2). The dimensions of the capsules are controlled by the fluid viscosities and flow rate as well as the channel size.

We have assembled an apparatus for microcapsule fabrication (Fig. 3). Our setup consists of an inverted microscope and high-speed camera for visualization, three syringe pumps for independent flow control of the three fluids, a UV LED for curing of the photosensitive shell material, and a laptop computer for control. The microfluidic device in Fig. 4 shows the three inlets for the fluids and the outlet for collection of the microcapsules. We used a photopolymerizable material for the shell. The shells were exposed to UV light after collecting in a vial (Fig. 5). We encapsulate a fluorescent dye within the shells in order to confirm that they are capsules. This also shows that the encapsulated material does not diffuse out of the shell.

Dimpled structures were fabricated out of hexanediol diacrylate (HDDA) using our PμSL system. This technique uses UV light and polymerizes 3-D shapes in a layer-by-layer fashion. An example of a dimpled structure fabricated using this technique is shown in Fig. 6.

Related References

1. Thorsen, T., *et al.,* "Dynamic Pattern Formation in a Vesicle-Generating Microfluidic Device," *Physical Review Letters,* **86**, 4163, 2001.
2. Utada, A., *et al.,* "Monodisperse Double Emulsions Generated from a Microcapillary Device," *Science*, **308**, 537, 2005.
3. Dendukuri, D., *et al.,* "Controlled Synthesis of Nonspherical Microparticles Using Microfluidics," *Langmuir*, **21**, 2113, 2005.
4. Shepherd, R. F., *et al.,* "Microfluidic Assembly of Homogeneous and Janus Colloidal Granules," *Langmuir*, **22**, 8616, 2006.

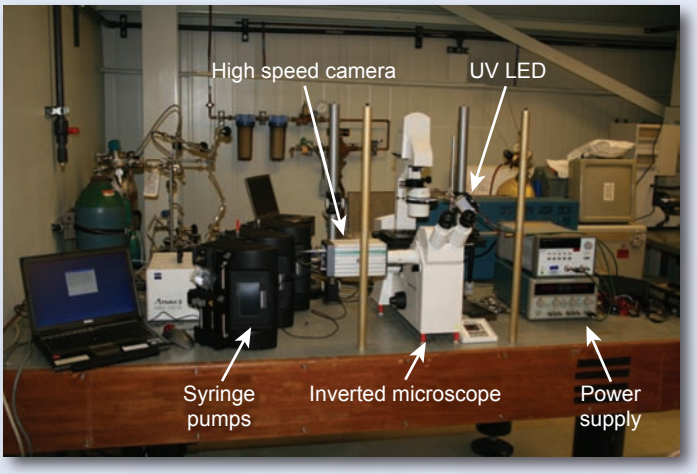

Figure 3. Apparatus for microencapsulation.

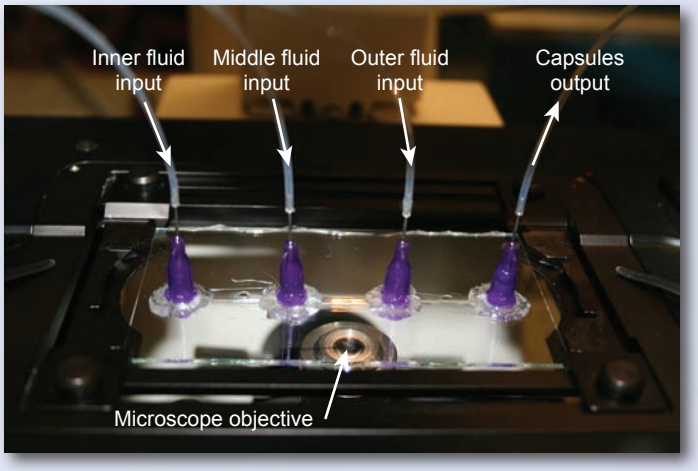

Figure 4. Photograph of microfluidic geometry.

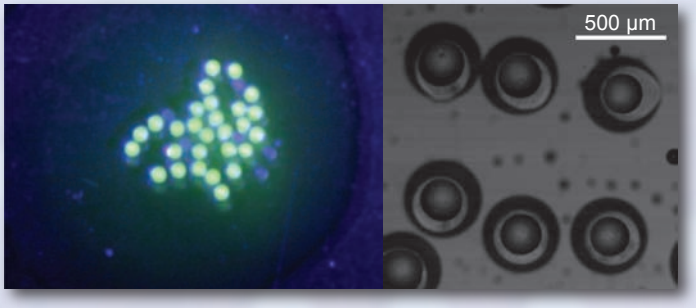

Figure 5. (a) Photograph of microcapsules under UV illumination; (b) optical micrograph of capsule cross-sections.

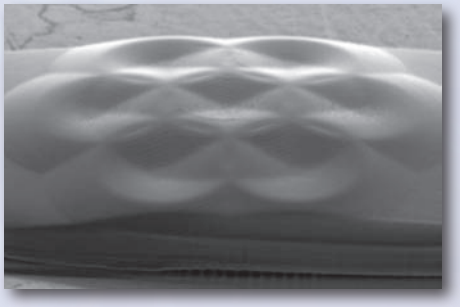

Figure 6. Dimpled microstructure fabricated with PμSL for light scattering.

PDMS Multilayer Soft Lithography for Biological Applications

For more information contact:

Dietrich A. Dehlinger
(925) 422-4030
dehlinger1@llnl.gov

Rapid and accurate characterization of biological pathogens is crucial for the response to new and emerging medical threats and for effective countermeasures. Large reductions in analytical time for characterization of novel biological pathogens require the demonstration of advanced instrumentation that completely automates complicated laboratory procedures and data analysis. Such automation will enable the determination of growth conditions, metabolic requirements, and effective treatments for novel pathogens in time to cut short incipient epidemics.

Project Goals

The primary goal of this project is to bring to LLNL the capability of fabricating polydimethylsiloxane (PDMS) multilayer soft lithography chips.

The secondary goal is to build a complete system to demonstrate their value for both reducing labor-intensive operations in biological research and improving biological methods. For example, microfluidic systems provide better environmental control for culturing cells than standard laboratory methods and also simplify continuous monitoring of individual cells. These advances are enabled by PDMS soft lithography, which allows for microfluidic channels that become instantly reconfigurable through the use of appropriately placed valves. The valves are simply an intersection of one microfluidic channel above another with each channel fabricated in a different stack of thin parallel silicon rubber. By pressurizing one microfluidic channel, the thin membrane separating it from another channel deflects, creating a small hydraulic valve. This reconfigurability can create new chambers, pump fluids through peristaltic action, and route those fluids to different parts of a device. The devices were made using the LLNL microfabrication facilities.

Relevance to LLNL Mission

The rapid detection and characterization of countermeasures are essential tools for detecting novel pathogens in time and to limit the scale of an incipient epidemic. Soft lithography capability will allow for the rapid creation of experimental platforms for screening, analysis, and enclosed long term monitoring of biological systems, thereby enhancing the nation's ability to prevent epidemics.

FY2010 Accomplishments and Results

In FY2010 we have:

1. Introduced the complete PDMS fabrication process to LLNL. This includes both the capability to manufacture the molds required for fabrication, as well as the processes required for complete device assembly. With capacity to manufacture chips using PDMS soft lithography in house, we have demonstrated an experimental platform tailored to meet an experimenter's specific needs while reducing experimental turnaround time.
2. Successfully and repeatedly fabricated robust, high yield devices. Using our established processes, we have demonstrated our capability to consistently make devices that hold up to long term experimental conditions. To test the viability of our devices, we ran complicated biological procedures that did not require operator input for days. Ultimately, similar experiments will operate unattended for weeks or months.
3. Assembled an automated microscope workstation for monitoring of devices under controlled conditions.

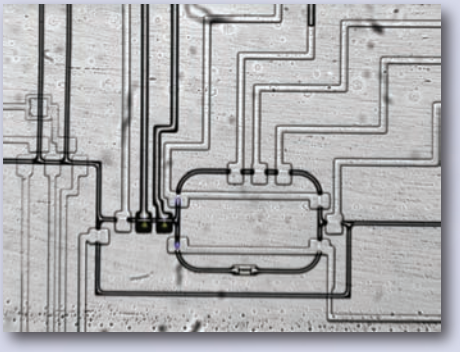

Figure 1. A close-up view of PDMS microchannels and valves used for cell cultures. The culture loop holds approximately 5 nL of fluid and thousands of cells.

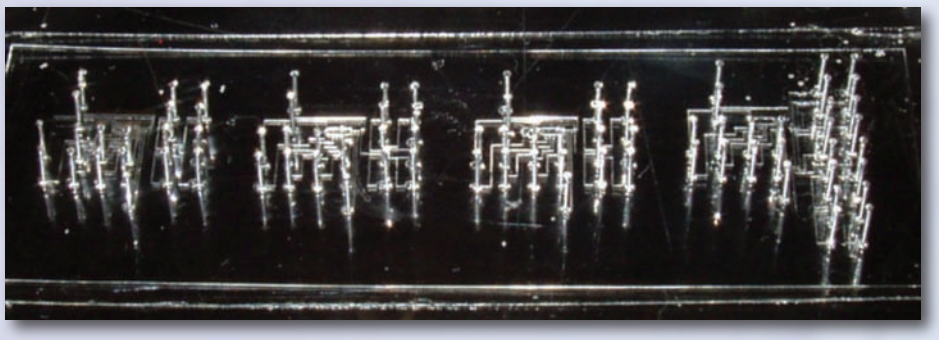

Figure 2. PDMS microfluidic chip containing four separate devices.

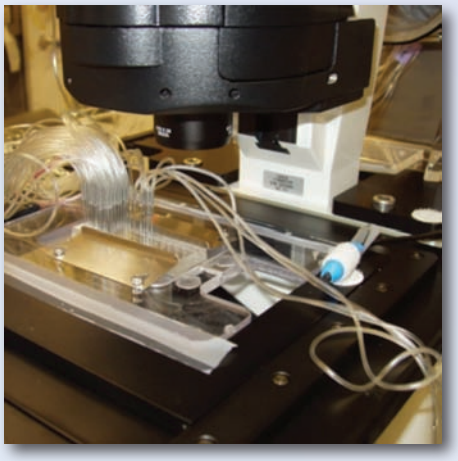

Figure 3. Chip interface system.

The primary use of the devices is to run experiments with highly controlled environmental conditions with optical measurements of the results. Our experimental platform took both fluorescent and bright field optical images at controlled points in space and at specified times. We gained high-resolution data about cellular systems over long periods of time without disrupting the experiment or requiring operator input.

4. Written a flexible program to control and monitor chips in an automated fashion. Both our experimental chip and the monitoring platforms are controlled via automation. We implemented a software package in Labview that provides integrated control of all platform components through one interface, and allows the scripting of automatic operation and monitoring of experiments for days.
5. Integrated all the components to form an automated cell culture system on a chip. By integrating our control software and our experimental monitoring and control system to our PDMS microfluidic laboratories we have demonstrated a fully automatic cell culture system with unprecedented ability to collect a time sequenced bright field and fluorescent images under various operating conditions without operator intervention.

Figures 1 through 5 are photographs of our system and controls.

Related References

1. Balagadde, F. K., H. Song, C. H. Collins, M. Barnet, F. H. Arnold, S. R. Quake, and L. You, "A Synthetic *Escherichia Coli* Predator-Prey Ecosystem," *Mol. Sys. Biol.,* **4**, 187, pp. 1–8, 2008.
2. Unger, M. A., H.-P. Chou, T. Thorsen, A. Scherer, and S. Quake, "Monolithic Microfabricated Valves and Pumps by Multilayer Soft Lithography," *Science,* **288**, 7, pp. 113–116, April 2000.
3. Duffy, D. C., J. C. McDonald, O. J. A. Schueller, and G. Whitesides, "Rapid Prototyping of Microfluidic Systems in Poly(dimethylsiloxane)," *Analytical Chemistry,* **70**, 23, pp. 4974–4984, December 1998.
4. Melin, J, and S. R. Quake, "Microfluidic Large-Scale Integration: The Evolution of Design Rules for Biological Automation," *Annu. Rev. Biophys. Biomol. Struct.,* **36**, pp. 213–31, 2007.
5. Balagadde, F. K., L. You, C. L. Hansen, F. H. Arnold, and S. R. Quake, "Long-term Monitoring of Bacteria Undergoing Programmed Population Control in a Microchemostat," *Science,* **309**, 5731, pp. 137–140, July, 2005.

FY2011 Proposed Work

In FY 2011, we will continue to use our results to support energy and medical applications as well as new areas.

We propose to 1) introduce this capability to several collaborating groups at LLNL; 2) implement a series of modules that can be used to rapidly assemble new devices as required; 3) work toward making these systems more portable and user friendly; and 4) implement devices and procedures to improve the input/output connections of the microfluidic devices with the macroscale world.

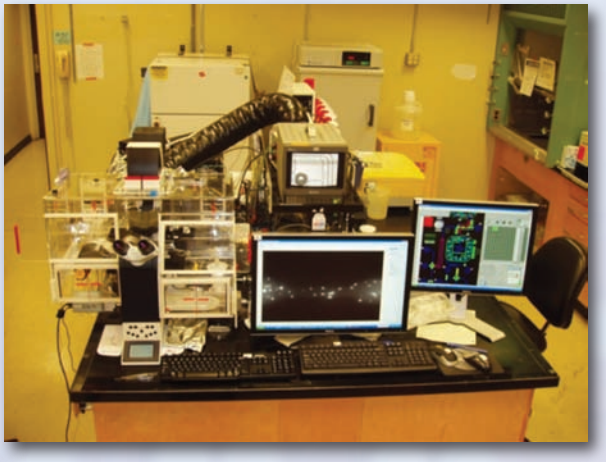

Figure 4. Microscope and environmental control system used to monitor and maintain growth conditions on the microfluidic system.

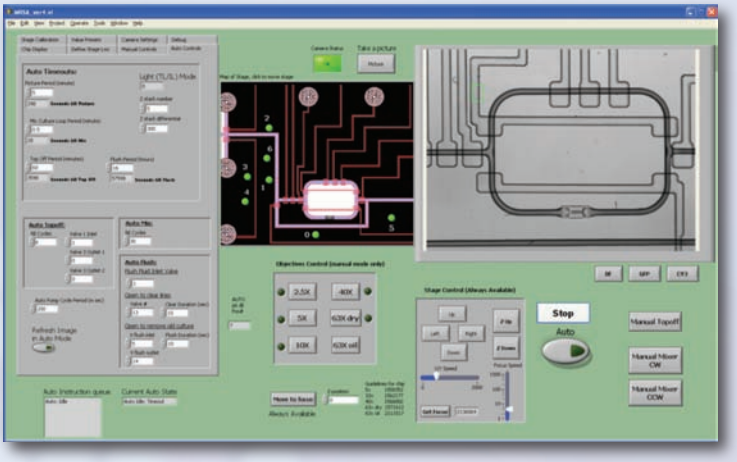

Figure 5. System control software.

Embedded Sensors for Gas Monitoring in Complex Systems

For more information contact:

Jack Kotovsky
(925) 424-3298
kotovsky1@llnl.gov

The change of a complex gas mixture within a closed system indicates the status of aging materials. Emission monitoring of trace gases reveals the onset and evolution of chemical indicators that offer an early warning of ensuing problems. This project advances technologies relevant to complex-mixture gas detection for advanced state-of-health system assessments.

Project Goals

The overall goal of this project is to develop broad-specie gas detection systems relevant for embedded trace-gas detection. These systems must be small, embeddable, and safe, while offering long-term fingerprint gas detection. To accomplish these goals, PhotoAcoustic Spectroscopy (PAS) and Surface Enhanced Raman Spectroscopy (SERS) are both being pursued. Both methods offer the potential of meeting the stated goals with fiber-optic addressable systems and offer similar features: fingerprint gas detection capability, very small form-factor, and remote, fiber-optic interrogation. Each has technical challenges that need to be overcome to meet their intended function.

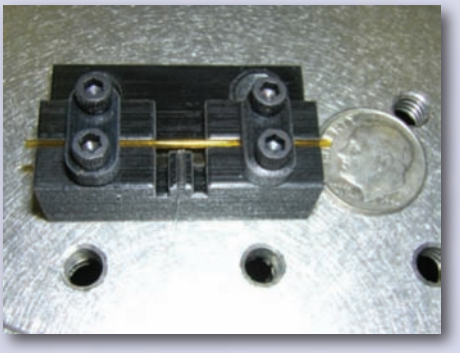

Figure 1. Second-generation photoacoustic spectrometer. The design includes an acoustic chamber and is powered and interrogated with a pair of optical fibers for remote, embedded trace-gas detection.

Relevance to LLNL Mission

As a national security laboratory, LLNL is responsible for ensuring that the nation's nuclear weapons remain safe, secure, and reliable through application of advances in science and engineering. Persistent surveillance through embedded sensing is a new paradigm for the efficient determination of the overall state-of-health of the stockpile. This effort contributes tools needed for this challenging instrumentation effort.

FY2010 Accomplishments and Results

PAS. PAS is capable of detecting infrared absorbing gas molecules in concentrations as low as parts per trillion. Molecules that absorb pulsed light at unique wavelengths will partially release absorbed energy in non-radiative modes, which produces local gas heating and a resultant pressure pulse. If the target molecule is present in a complex gas sample, a pressure wave is produced at the light's pulse frequency. To be adapted to LLNL mission relevance, a fiber-optic-based acoustic detector must be created and the system must be reduced in size by orders of magnitude.

In this first year, an electronic acoustic detector was used to score optical-acoustic-detector prototypes. Absorption lines and thermal noise investigations guided the design and implementation of a proprietary laser system that addresses background noise issues, such as thermal noise and broad-absorbing acoustic chamber, with a novel optical compensation. A first-generation optical acoustic detector was designed, built, and tested. A second-generation acoustic detector was designed with excellent flexibility and tunability to optimize the system's sensitivity (Fig. 1).

SERS. SERS has been around for many years, principally for liquid and solid sample analyses. At LLNL we have been able to detect femtomolar-concentration solutions reproducibly on wide area, Ag- and Au-coated Si or SiO_2 nanopillar substrates. The high sensitivity of our substrates enables the pursuit of much harder gas-phase detection, and their compatibility with optical fiber leads to consideration for an *in-situ*, compact detection device (Fig. 2).

A confocal Raman setup (Fig. 3) was used to detect O_2 in ambient air and in nitrogen-purged atmosphere at different temperature cycles, as shown in Fig. 4. Most of the observed peaks are within 10 cm^{-1} of assigned peaks due to O_2 species reported in literature, the presence of which was also confirmed by XPS.

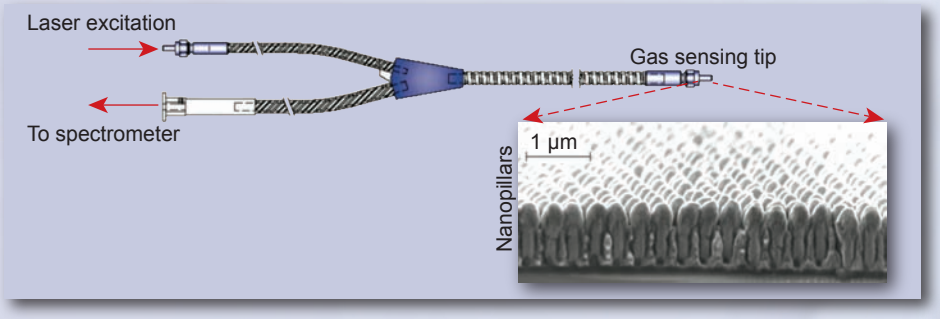

Figure 2. Conception of fiber-based SERS using LLNL SERS templates for sensing and fiber bundles for excitation and delivery of signal.

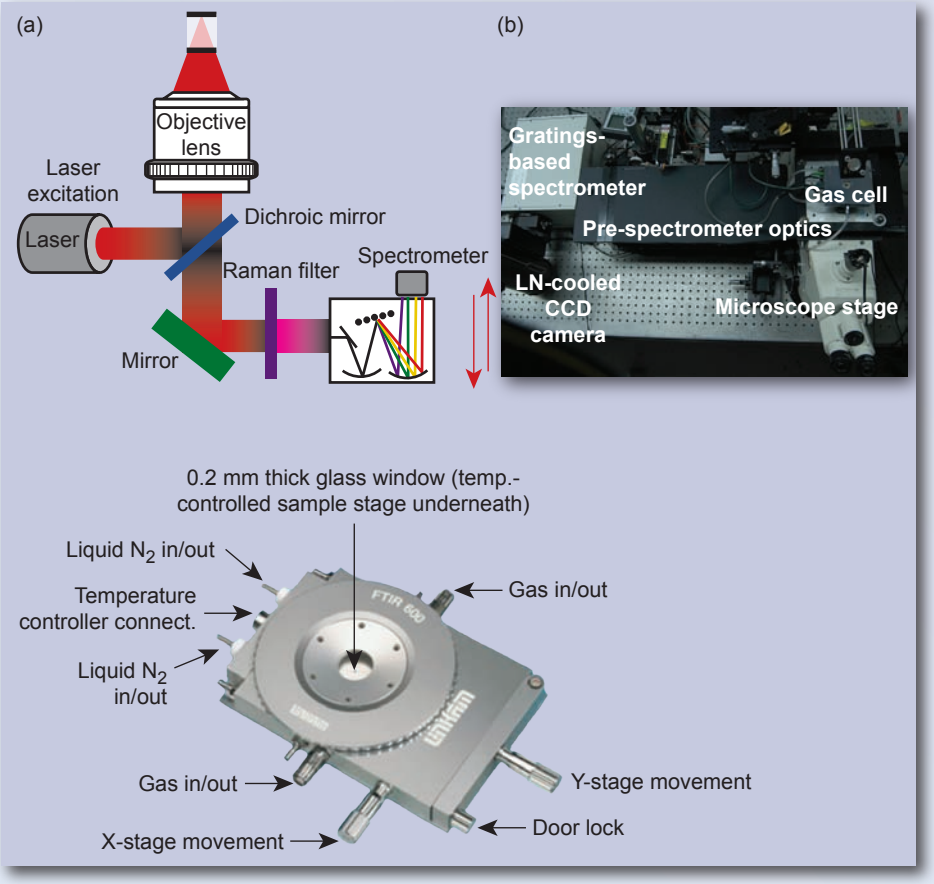

Figure 3. (a) Schematic of confocal Raman system; (b) real setup with pressure- and temperature-controlled gas cell (196 °C to 600 °C).

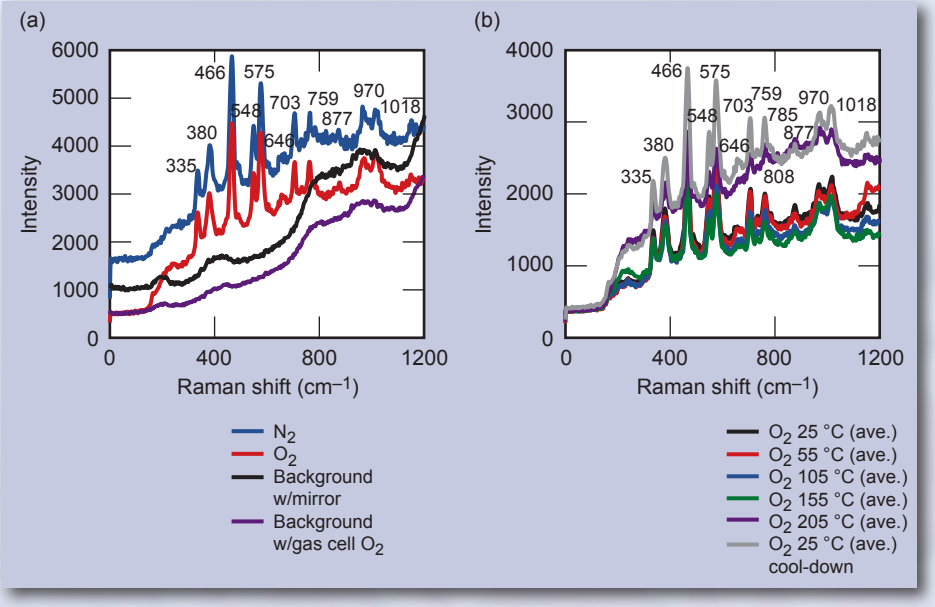

Figure 4. (a) SERS spectra from LLNL Pillars Substrate under N_2 and O_2 flow at room temperature; (b) SERS spectra of O_2 using LLNL Pillars Substrate at various substrate temperatures.

An independent fiber-based Raman system was setup in a fume hood with a controlled gas delivery of CO, various NOx, as well as VOCs, in addition to a low-noise fiber probe and high-power ultra-stable laser for highly sensitive measurements. Initial tests on toluene have been performed with detection by SERS.

Related References

1. Gartia, M., *et al.*, "Surface Enhanced Raman Spectral Characterization of Large-Area High-Uniformity Silver-Coated Tapered Silica Nanopillar Arrays," *Nanotechnology*, **21**, 39, 2010.
2. Gartia, M., *et al.*, "Large-Area Vertical Nanopillar Arrays," *FACCS*, Raleigh, North Carolina, October 2010.
3. Bora, M. G., *et al.*, "Vertical Pillar Array Plasmon Cavities," *Nanoletters,* **10**, 8, 2010.
4. Moseir-Boss, P., and S. H. Lieberman, "Detection of Volatile Organic Compounds Using Surface Enhanced Raman Spectroscopy Substrates Mounted on a Thermoelectric Cooler," *Journ. Chim. Acta*, **488**, pp. 15–25, 2003.
5. Smythe, E. J., *et al.*, "Optical Antenna Arrays on a Fiber Facet for *In Situ* Surface-Enhanced Raman Scattering Detection," *Nanoletters*, **9**, 3, pp. 1132–1138, 2009.

FY2011 Proposed Work

PAS. In FY2011, the new laser system and the second-generation acoustic detector (Fig. 1) will be tested. These features will be housed in a series of shrinking acoustic chambers in the pursuit of an embedded system of less than 3 mm. If successful, design iterations will work toward a balance of improved limits of detection and reduced system size. Tests of varied CO_2 concentrations and complex mixtures will be used to benchmark the system performance.

SERS. In FY2011, we plan to test different gas mixtures in a controlled environment to determine cross-sensitivity, specificity, and limit of detection. We will also introduce chronocoulometry to characterize the surface dynamics.

Neutron Cookoff: Read-Out Electronics for LLNL Pillar Detector

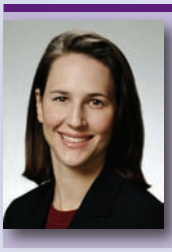

For more information contact:

Rebecca Nikolić
(925) 423-7389
nikolic1@llnl.gov

This project is constructing a high-efficiency pillar structured thermal neutron detector. As we are now moving from the proof-of-principle phase toward instrumentation, having the ability to read out our device is critical for our continued growth in this area.

Specifically, as there is a pressing need for a ^{3}He tube replacement, our project is now under increased time pressure to show that a field ready device is possible in a short time frame. LLNL has been requested to participate in the next "neutron cookoff," in which the Domestic Nuclear Detection Office (DNDO) will perform laboratory tests of the detector modules with neutron- and gamma-ray emitting sources to characterize parameters such as the inherent efficiency, response/dead time, environmental/mechanical performance, and gamma rejection.

Project Goals

Under this project we will build the read-out electronics for one element and test the electrical and radiation performance. Then we will tile up to nine of these elements together and integrate again with the read-out components and characterize our instrument.

Relevance to LLNL Mission

LLNL is funded by DHS-DNDO to construct a high-efficiency pillar structured thermal neutron detector, consistent with its homeland and global security missions.

FY2010 Accomplishments and Results

A schematic of our device is shown in Fig. 1.

The read-out electronics is based on a well-known topology, its arrangement originally constructed to provide germanium-quality performance. In this case, such a level of performance is not required and several compromises could be made for low power while preserving adequate bandwidth (20 ns rise time). The fast response is needed to provide adequate timing for coincidence measurements. The noise profile of the system is different from most standard applications, in that the dominant noise in the read-out is given by the detector leakage current. Therefore, the input JFET was not chosen, as in common practice, to capacitively match the detector, but to give negligible overall noise contributions (1/f, white and current noise) to the overall noise figure for the lowest reasonable current consumption (~1 mA drain current).

For simplicity, and to allow the capability of collecting holes or electron signals, the power supply rails have been kept at +/–12 V, but further optimization on their value could be done to further lower the power consumption. The preamplifier is followed by a fast shaper using a semi-Gaussian, fourth-order bipolar shape with 250-ns peaking time. This choice minimized the dominant noise component, the detector's current noise associated with its leakage current. Bipolar shaping poses a penalty to the white (high-frequency) noise components but is more tolerant to the lower frequency components and offers intrinsically better baseline return than unipolar signals, mitigating the need for a baseline restoration circuit.

The shaper optimizes the signal-to-noise ratio for the signal and its output is fed to a simple low-power, leading edge comparator that detects the presence of a signal, but the shaper output is also capable of driving 50-ohm loads for different applications.

The fabrication of the read-out electronics board, integration with our detectors and system characterization was done at LLNL.

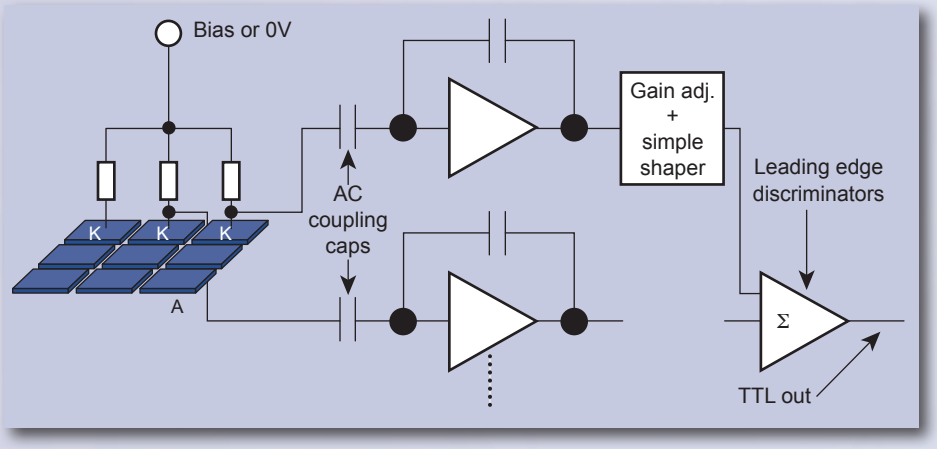

Figure 1. Schematic of LLNL pillar detector integrated with read-out.

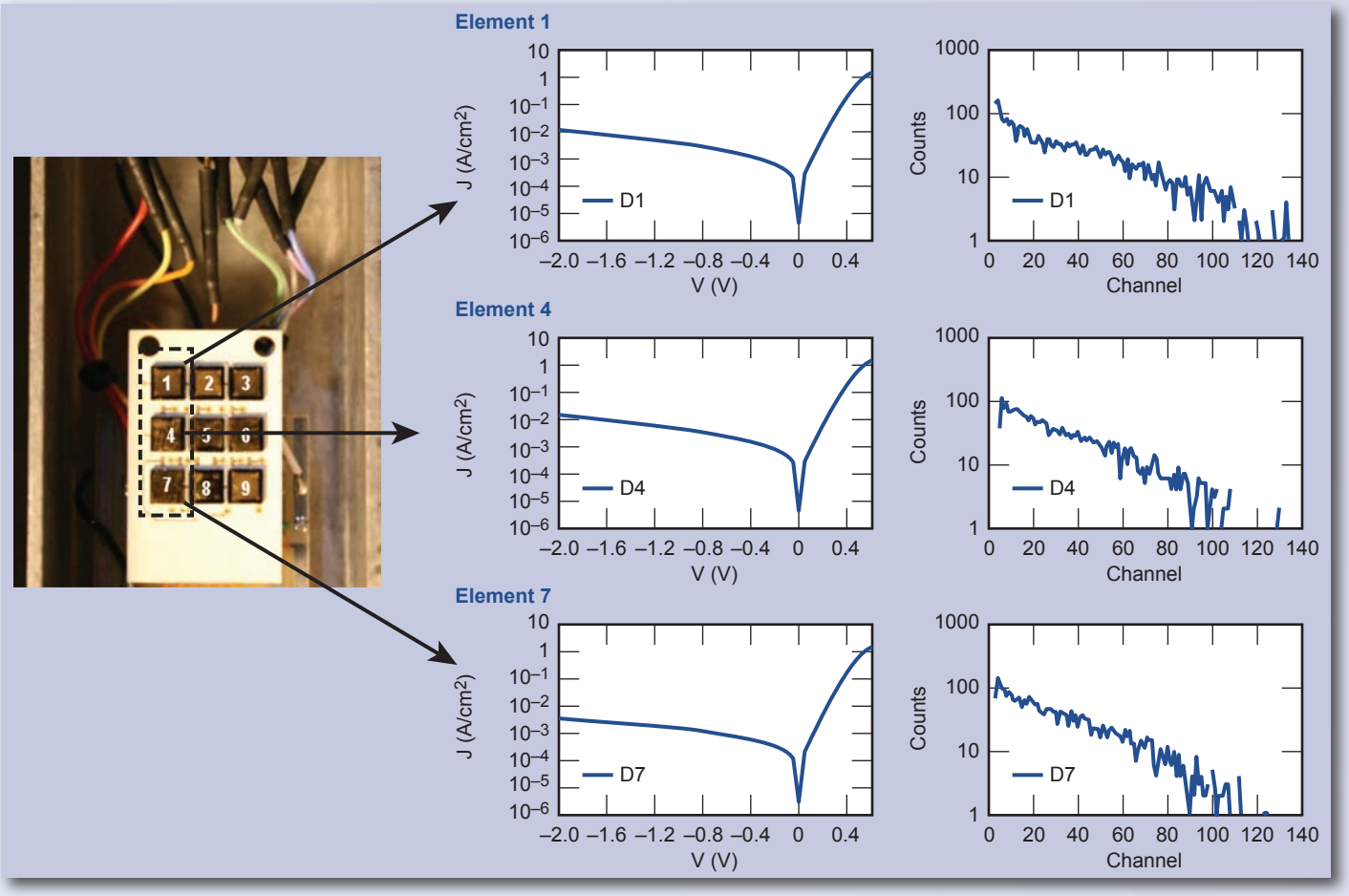

Figure 2. **Nine-element detector. Each detector has an active area of 2 mm × 2 mm. Current vs. voltage and thermal neutron response are shown for the first column of the 3 × 3 set.**

Figure 2 shows a picture of a 3-×-3 array of detectors integrated into the 9-channel read-out system, showing the electrical and radiation response. Figure 3 shows the final integrated system that was fully characterized under this project. The next step is the participation of our detector in the "DNDO Neutron Cookoff" tentatively scheduled for fall 2010.

Related References

1. Fabris, L., N. W. Madden, and H. Yaver, "A Fast, Compact Solution for Low Noise Charge Preamplifiers," *NIM-A* **4242**, pp. 545–551, 1999.

2. Conway, A. M., R. J. Nikolic, and T. F. Wang, "Numerical Simulations of Carrier Transport in Pillar Structured Solid State Thermal Neutron Detector," *International Semiconductor Device Research Conference,* College Park, Maryland, December 12–14, 2007.

3. Nikolic, R. J., A. M. Conway, C. E. Reinhardt, R. T. Graff, T. F. Wang, N. Deo, and C. L. Cheung, "Pillar Structured Thermal Neutron Detectors," *International Conference on Solid State and Integrated Circuit Technology,* Beijing, China, October 20–23, 2008.

4. Nikolic, R. J., C. L. Cheung, C. E. Reinhardt and T. F. Wang, "Roadmap for High Efficiency Solid-State Neutron Detectors," *SPIE – International Symposium on Integrated Optoelectronic Devices,* **6013**, 1, pp. 36–44, 2005.

5. Nikolic, R. J., A. M. Conway, C. E. Reinhardt, R. T. Graff, T. F. Wang, N. Deo and C. L. Cheung, "Pillar Structured Thermal Neutron Detector With 6:1 Aspect Ratio," *Appl. Phys. Lett.,* **93**, p. 133502, 2008.

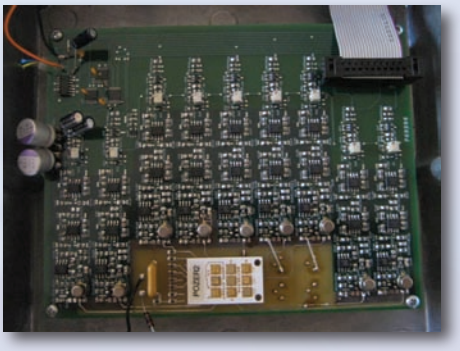

Figure 3. **Nine-channel COTS read-out integrated with nine-element pillar detector array.**

Isotachophoretic Separation of Actinides

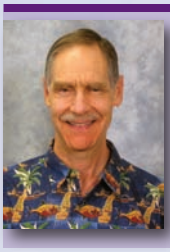

For more information contact:

Raymond P. Mariella, Jr.
(925) 422-8905
mariella1@llnl.gov

Isotachophoresis (ITP), also known as ionic migration, electromigration, steady-state-stacking electrophoresis, and disc electrophoresis, is an electrophoretic technique that separates and stacks mixtures of two or more ions (charged particles) in solution, according to their electrophoretic mobilities, μ_i, where the subscript "i" refers to the "i^{th}" ion, either "A" or "B" in Figure 1. The ultimate resolution of two ions, A and B, is a nonlinear function of the differences of their electrophoretic mobilities, μ_A and μ_B, as well as their diffusion coefficients in the solution at the interface between the separated regions. Influenced by the concentration of the leading electrolyte, "L," ions, A and B can be both separated and concentrated, with concentrations possibly exceeding the Debye-Hückel assumptions of dilute solute.

A reduction of overall channel length has been demonstrated with the use of a counter flow.

Figure 1 is a schematic of the ITP technique, showing the separation of a mixture of "A" and "B," with time progressing from t_0 to t_6; "L" is the leading electrolyte, and "T" is the trailing electrolyte.

Project Goals

Our goal was to determine whether ITP could be applied to the analysis of numerous 10-g samples of debris/rubble from an event. ITP was identified for such an application, because, as opposed to chromatography and electrophoresis, ITP is capable of rivaling state-of-the-art separations that use ion-exchange columns for separation *and* concentration of minority constituents in multi-gram samples. Our literature search also found that the apparatus for ITP can be very simple (Figs. 2 and 3).

As can be seen from equations (1) and (2), the key physical parameters that are needed to model the ITP

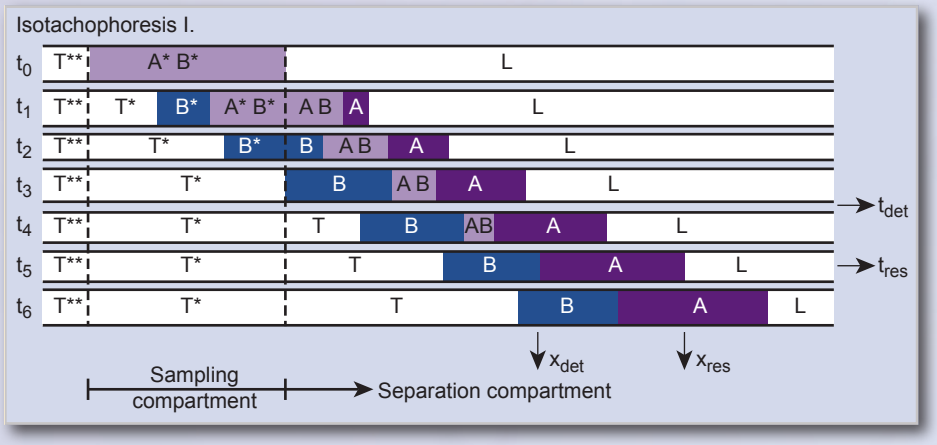

Figure 1. Schematic of ITP technique.

Figure 2. Apparatus for ITP.

process are diffusion coefficients D_i and electrophoretic mobilities μ_i. Although this feasibility project did not have sufficient funds to perform *ab initio* or similar modeling, we have found literature examples that have modeled the ions, themselves, which leaves us optimistic that D_i and μ_i. can be calculated, using semi-empirical calculations:
Simplified equation of continuity

$$\frac{\partial c_i}{\partial t} = D_i \frac{\partial^2 c_i}{\partial x^2} - j \frac{\partial}{\partial x}\left(\frac{c_i \mu_i}{k}\right) \qquad (1)$$

Kohlrausch regulating function

$$C_i = C_L \frac{\mu_i(\mu_L + \mu_{LC})}{\mu_L(\mu_i + \mu_{LC})} \qquad (2)$$

where μ is the mobility of an ion (i), leading electrolyte (L), or leading counter ion (LC).

Figure 4 is a QM calculation of $UO_2(CO_3)_3^{4-}\bullet 28(H_2O)$ that includes the double layer and even the outer (third) layer of associated solvent molecules. It seems likely that the "non-slip" assumption in which such an ion is modeled as a hard sphere will fail, since the "free" solvent molecules can be expected to exchange readily with the third layer of "bound" solvent molecules.

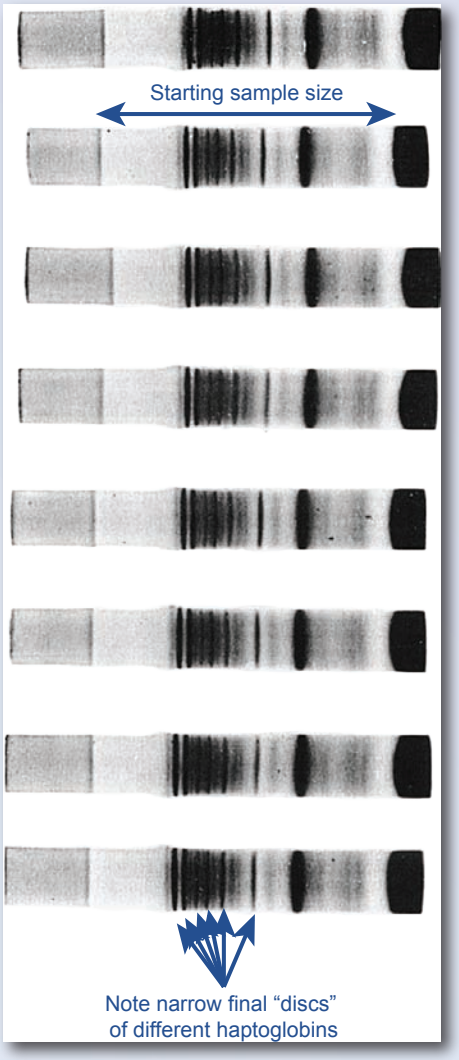

Figure 3. Large-scale separation of proteins from serum, using the apparatus pictured in Fig. 2. Note the narrow zones (discs) that formed for each constituent, over time, notwithstanding the relatively large diameters of the separation columns. Flow was left to right and the reproducibility of the process for multiple tubes in parallel is clearly visible.

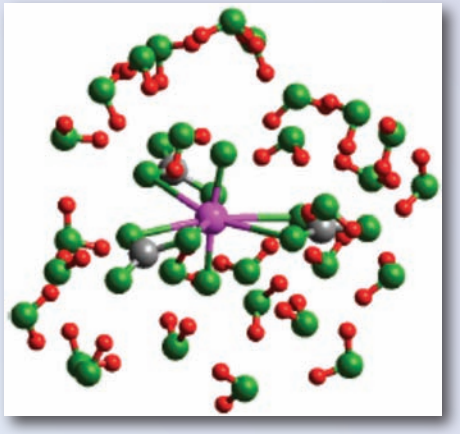

Figure 4. QM calculation of $UO_2(CO_3)_3^{4-}\bullet 28(H_2O)$ that includes the double layer and the outer (third) layer of associated solvent molecules. Green = oxygen atom; red = hydrogen atom; pink = uranium atom; and gray = carbon atom.

Relevance to LLNL Mission

Rapid, quantitative sample preparation (separation and purification) is a key step in post-detonation nuclear forensic analysis, an important component of the Laboratory's mission. A procedure that uses ITP offers increased throughput over the state-of-the-art procedures.

FY2010 Accomplishments and Results

The FY2010 Literature Search provided information that strongly supports the application of ITP to analyze heavy metals in debris/rubble. We conclude that ITP is appropriate for three reasons:

1. Majority constituents, such as ions from the elements Ca, Mg, Al, Na, and K can be discarded from the sample, due to their significantly differing electrophoretic mobilities from ions such as UO_2^{+2}.

2. Many-gram quantities are handled via ITP in relatively simple apparatus.

3. Minority constituents of a mixture are routinely concentrated during the ITP process, reaching concentration factors of one million-fold in optimized cases.

It would be very important to make experimental measurements of the separation factors of actinide ions and ion complexes as the heart of a follow-on project.

Related References

1. Kendall, J., *Science*, **67**, 163, 1928.
2. Brewer, A. K., *et al., Journal of Research of the National Bureau of Standards,* **38**, 137, 1947.
3. Kubicki, J., G. Halada, P. Jha, and B. Phillips, *Chemistry Central Journal,* **3**, 10, 2009.
4. Choppin, G. R., and R. J. Silva, *Journal of Inorganic & Nuclear Chemistry,* **3**, 153, 1956.
5. Jung, B., R. Bharadwaj, and J. G. Santiago, *Analytical Chemistry,* **78**, 2319, April 2006.

Extraction of White Blood Cells from Whole Blood Through Acoustic Focusing

For more information contact:

Elizabeth K. Wheeler
(925) 423-6245
wheeler16@llnl.gov

In this project, we used acoustic focusing within a microfluidic device to attempt to separate white blood cells from a sample of whole blood. White blood cells provide important biomarkers that can be used as presymptomatic detection of infections and disease. To isolate and detect these biomarkers, the white blood cells must first be extracted from whole blood to remove the significant background material.

The microfluidic device used for these separations was created previously as a large cell/particle separator for performing automated sample preparation on complex biological samples such as blood, sputum, and urine.

The device works by using a piezoelectric transducer bonded to a silicon/glass chip with a microchannel etched into the silicon. When the transducer is driven with a high frequency AC voltage, it generates acoustic standing waves in the microfluidic channel. These waves produce a force field that moves particles to nodes or antinodes of the acoustic wave depending on the relative compressibility and density between the particle and the suspending liquid. The magnitude of the acoustic forces scales with the volume of the particle, providing a natural size cutoff for fractionation, while the node and antinode locations depend on the fluid channel geometry and the acoustic driving frequency.

This system, shown in Fig. 1, was previously demonstrated to separate polystyrene particles as small as 2 µm at a throughput of up to 100 µL/min.

Project Goals

The goals of this project are: 1) create a surrogate blood sample with white blood cells spiked into whole animal

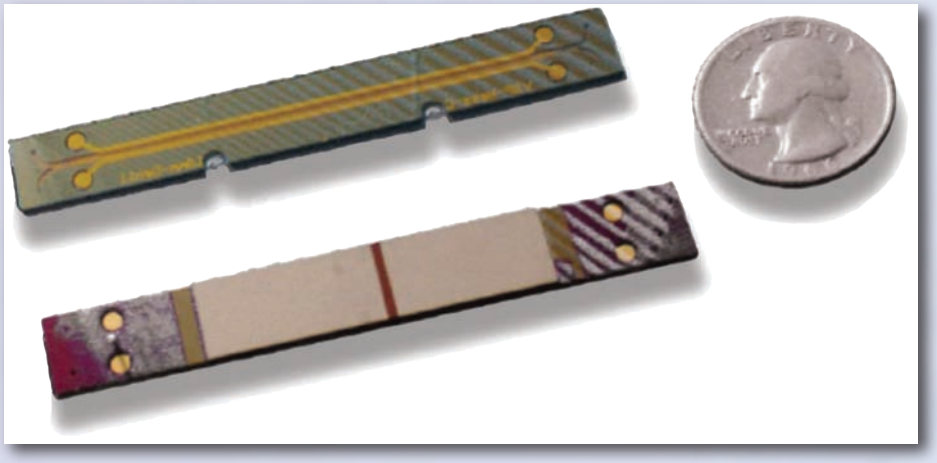

Figure 1. Image of the front (top) and back (bottom) of microfluidic acoustic chip. The gray region in the lower Image is the piezoelectric transducer that generates the acoustic waves within the etched microchannels.

blood for device testing; 2) demonstrate that the acoustic forces in the existing devices are sufficient to focus and separate white blood cells in a purified sample (1X phosphate buffered saline (PBS) solution); and 3) demonstrate separation of white blood cells from whole blood.

Relevance to LLNL Mission

This work directly impacts ongoing and future efforts within LLNL's Global Security Principal Directorate for new platforms for biosecurity applications. Preparation of complex samples, such as the removal and extraction of target white blood cells, is a critical step to maximize the selectivity and sensitivity of downstream biological assays to detect important markers for infection and/or disease. To date, the best selective preparation results have been achieved in laboratories where effective sample preparation using benchtop techniques, such as membrane filtration, centrifugation, and chemical methods, have been applied to the samples. Our goal is to demonstrate a robust, automated sample preparation that reduces preparation time, improves performance of downstream detection assays, and can be integrated into an end-to-end detection platform.

FY2010 Accomplishments and Results

Accomplishments and results for this year include the following:

1. Implemented protocols for culturing and staining Raji cells that are B lymphocytes from a leukemia cell line with an average size of 7–8 µm (Fig. 2).
2. Demonstrated focusing and separation of white blood cells out of a phosphate buffered saline stream using the microfluidic acoustic device shown in Fig. 3.
3. Identified the need for a coating (*e.g.,* heparin) in the microfluidic separator and associated fluidics to reduce clogging due to adsorption of material from the blood onto the exposed surfaces.

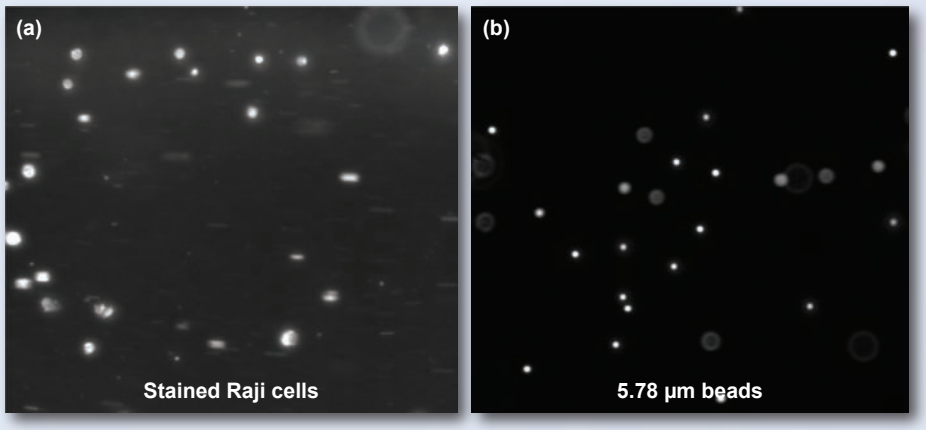

Figure 2. (a) Stained white blood cells (Raji cells) used in acoustic separation experiments. The cells are generally 7–8 µm in diameter and are shown next to (b) 5.78-µm fluorescent particles for comparison.

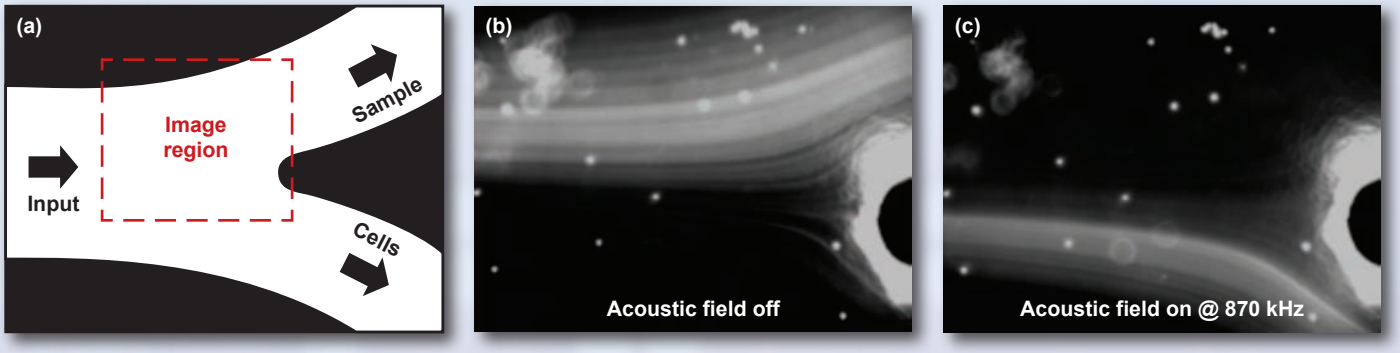

Figure 3. Acoustic focusing and extraction of white blood cells from an input sample stream (cells suspended in PBS). (a) Top view of microfluidic chip near the bifurcating exit. The sample flows in from the left side in the upper half of the channel and exits the top if the acoustic field is turned off and the bottom when the field is on. (b) Raji cells exiting through the upper outlet with the acoustic field turned off. (c) Raji cells focused and exiting the lower stream when the acoustic field is turned on.

Measurement Technologies

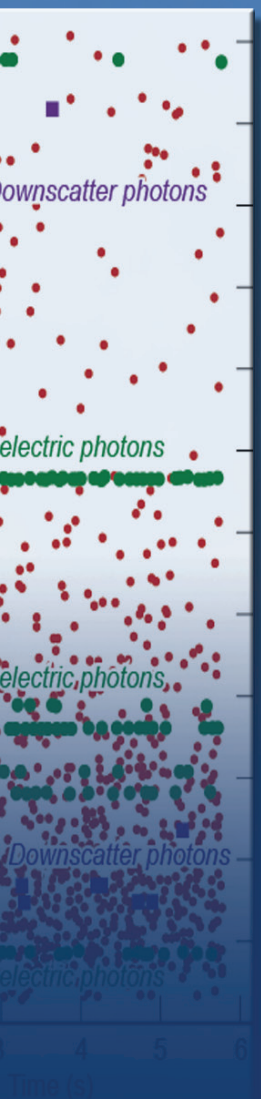

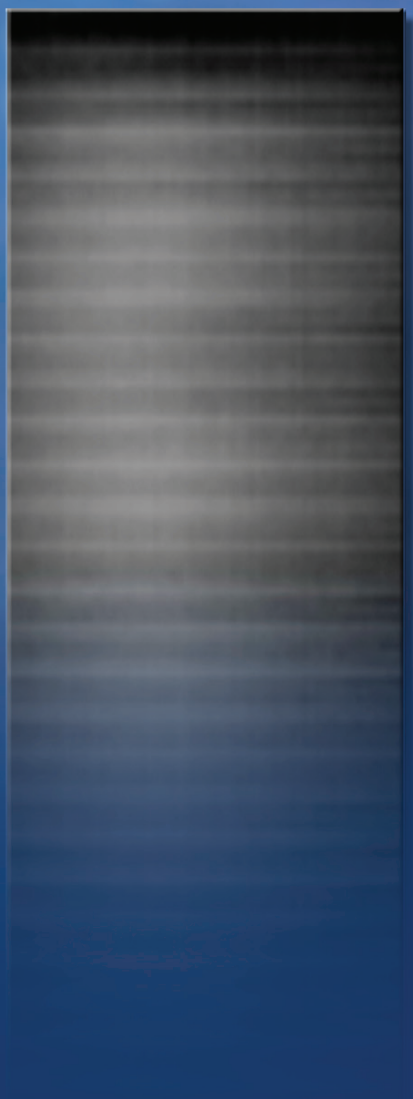

Detection, Classification, and Estimation of Radioactive Contraband from Uncertain, Low-Count Measurements

For more information contact:

James V. Candy
(925) 422-8675
candy1@llnl.gov

Radionuclide (RN) detection is a critical first line defense used by Customs and Border Protection (CBP) to detect the transportation of radiological materials by potential terrorists. Detection of these materials is particularly difficult due to the inherent low-count emissions produced. RN detection from low-count gamma ray emissions is a critical capability that is very difficult to achieve.

This project is focused on the detection, classification, and estimation of special nuclear material (SNM) from highly uncertain, low-count RN measurements. We apply innovative sequential Bayesian model-based statistical processing algorithms that take advantage of the statistical nature of radiation transport physics by incorporating *a priori* knowledge of nuclear physics. This effort encompassed theory, simulation, experiments, and application. It enabled the development of advanced signal/image-processing techniques for the next generation of processors.

Project Goals

The goal is to develop an innovative radiation-detection solution uniquely qualified to provide rapid and reliable performance in applications that require accurate detection of radioactive material. Thus, our goal is a reliable detection with a 95% detection probability at a 5% false alarm rate in less than a minute.

Relevance to LLNL Mission

The detection of illicit SNM is a top priority of LLNL in furthering its national security mission. RN detection, classification, and identification are critical for detecting the transportation of radiological materials by terrorists, an important goal in national and international security.

FY2010 Accomplishments and Results

Our FY2010 accomplishments included the development of a "smart" Statistical Radiation Detection System (SRaDS) software capable of automatically detecting the presence of targeted SNM by incorporating a parallel/distributed sequential processor. The following was accomplished:

1. Theoretically, developed an optimal (physics-based) decision function incorporating both photoelectric and downscattered photons (Compton scattering).
2. Applied these theoretical results to develop a "smart" algorithm capable of automatically providing detection of targeted SNM.
3. Implemented a simple signal processing transport (1-D geometry) model enabling downscatter photon discrimination.
4. Estimated the required physics parameters such as channel energy, interarrival parameters, and emission probabilities, using modern Bayesian sequential techniques (Kalman and particle filters).
5. Implemented a parallel/distributed algorithmic structure capable of being realized by field programmable gate arrays (FPGA) for high computational speeds.

The basic structure of the processor implementation is shown in Fig. 1. After the photon information (energy/rate) is extracted from the photon by the measurement electronics, it is *discriminated* to determine if it is associated with the target RN. If so, the parametric information is enhanced by performing *parameter estimation* and input to update the sequential decision function to *decide*

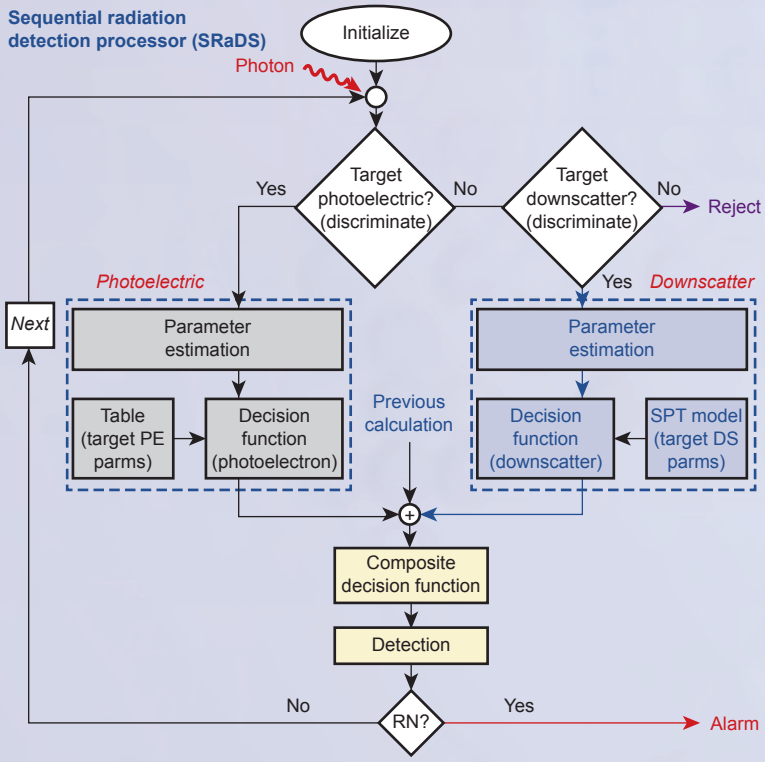

Figure 1. Schematic of statistical Bayesian design.

(detection) whether or not the targeted RN is present.

Results of this photon-by-photon processor with downscatter are shown in Fig. 2. In the figure, three columns are shown. The first column is the composite (not used) pulse-height spectrum (PHS), with the second the measured photon energies (arrivals) in red circles with the green circles representing the *discriminator* output photoelectrons and the purple squares the discriminated downscatter photons. Notice that they align with the PHS energy "lines." The final column is the *decision* function for each of the targeted RNs. As each photon is processed, the decision function is sequentially updated until one of the thresholds (target/non-target) is crossed (solid red box in figure) declaring a targeted threat or non-threat.

The performance of the processor was substantiated by extracting a 100-member ensemble of controlled experimental data and comparing it to the GAMANAL software solution, where its detection rate of 98% easily exceeded that of 47% both at essentially 0% false alarm rate. These results demonstrate the potential capability of the sequential Bayesian model-based approach to solving a variety of radiation-detection problems.

Related References

1. Candy J. V., E. F. Breitfeller, B. L. Guidry, D. Manatt, K. E. Sale, D. H. Chambers, M. A. Axelrod, and A. M. Meyer, "Physics-Based Detection of Radioactive Contraband: A Sequential Bayesian Approach," *IEEE Trans. Nuclr. Sci.,* **56**, 6, pp. 3694–3711, 2009.
2. Candy, J. V., D. H. Chambers, E. F. Breitfeller, B. L. Guidry, J. M. Verbeke, M. A. Axelrod, K. E. Sale, and A. M. Meyer, "Threat Detection of Radioactive Contraband Incorporating Compton Scattering Physics: A Model-Based Processing Approach," *IEEE Trans. Nuclr. Sci.,* **57**, 6, 2010.
3. Candy, J. V., D. H. Chambers, E. F. Breitfeller, B. L. Guidry, J. M. Verbeke, M. A. Axelrod, K. E. Sale, and A. M. Meyer, "Model-Based Detection of Radioactive Contraband for Harbor Defense Incorporating Compton Scattering Physics," *Proc. OCEANS09, IEEE OES Soc.,* 2010.
4. Candy, J. V., D. H. Chambers, E. F. Breitfeller, B. L. Guidry, J. M. Verbeke, M. A. Axelrod, K. E. Sale, and A. M. Meyer, "Radioactive Threat Detection with Scattering Physics: a Model-Based Application," *Proc. CIP, IEEE Comp. Soc.,* 2010.

FY2011 Proposed Work

Teaming with ICx, a well-known, portable radiation detection system manufacturer, an R&D 100 award was received for this project with a high anticipation of "bringing it to market" in the future.

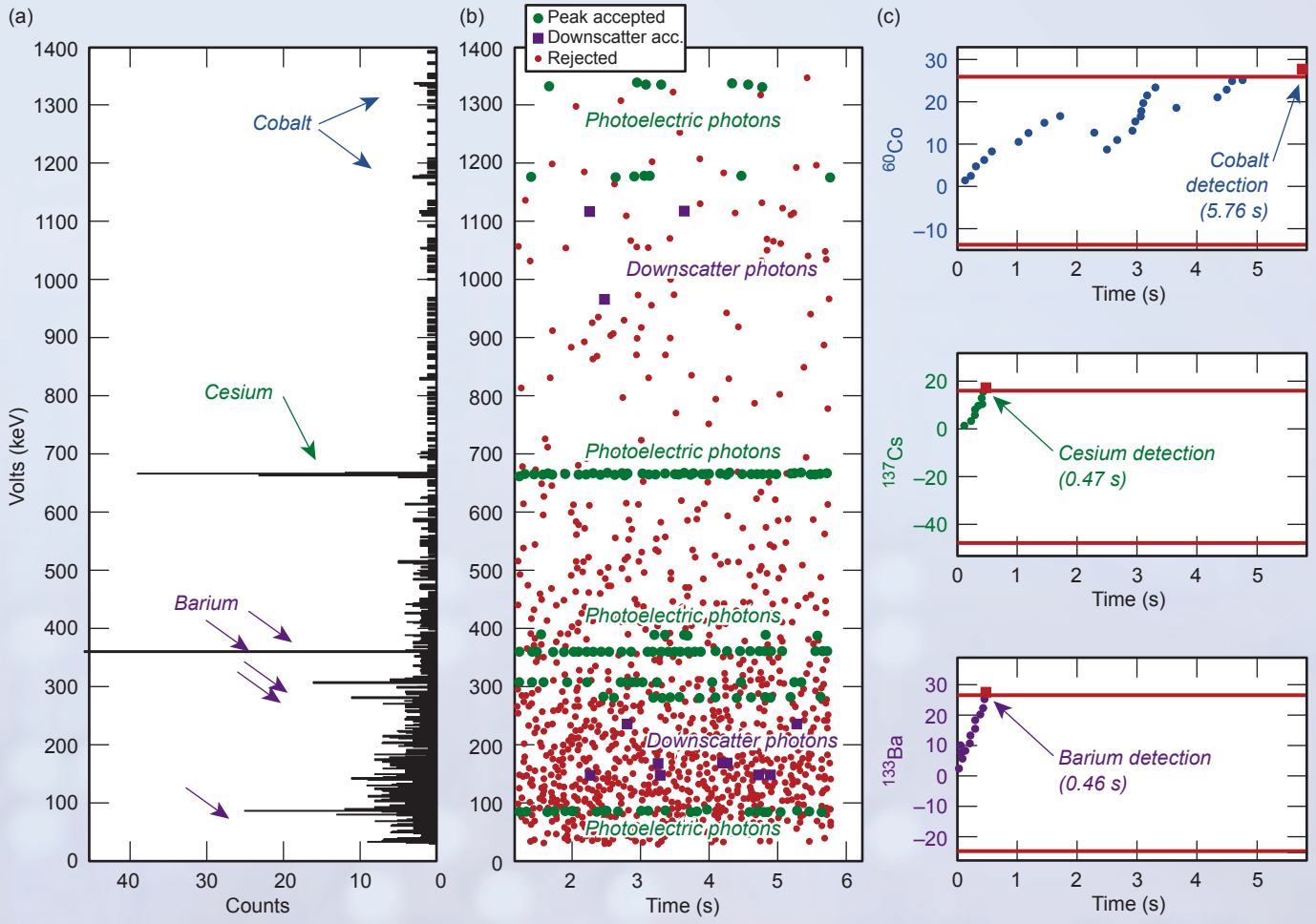

Figure 2. Sequential Bayesian detection and identification. (a) Pulse-height spectrum (after calibration). (b) Photon arrivals (red circles) with photoelectron discrimination (green circles) and downscatter photons (purple squares). (c) Decision functions for ^{60}Co.

Optimized Volumetric Scanning for X-Ray Array Sources

For more information contact:

Angela M. K. Foudray
(925) 422-1509
foudray1@llnl.gov

X-ray measurement systems are used for nondestructive evaluation (NDE) to determine noninvasively the internal structure of objects. NDE application areas include medicine, industrial manufacturing, military, homeland security, and airport luggage screening. X rays are most widely used because of their ability to penetrate a wide range of materials. In a traditional x-ray system, a single source and detector system rotates and/or translates with respect to the object under evaluation, gathering projections from only a single perspective. Mathematical algorithms are used to invert the detected forward-attenuated ray projections to form images of the object.

More recently, arrays of sources have been used to gather projections from multiple perspectives per detection location. The spatially diverse nature of x-ray array sources has the potential of reducing data collection time, reducing imaging artifacts, and increasing the resolution of the resultant images. Most of the existing CT algorithms were developed assuming a single source, some making approximations that take advantage of the simplified traditional system configuration.

Figure 1. Photograph of the x-ray array source and array detector system designed and developed by industrial collaborators NovaRay and Triple Ring.

We are investigating methods to determine if these sources would change the way LLNL would acquire NDE computed tomography (CT) data.

Single-source x-ray CT data collection, processing, and imaging methods and algorithms are not applicable when the source location is expanded from one dimension (a rotating and/or translating point source) to two (a rotating and/or translating array). There are four tasks in the research to achieve the project goal: 1) develop forward array source analytic and computational models; 2) research and develop array source reconstruction algorithms; 3) perform experiments and simulations; and 4) evaluate systems' performances.

Project Goals

The goal of this project is to determine the applicability of x-ray array sources to problems of interest to LLNL and its customers. It is believed array source data collection will be faster, while yielding higher resolution reconstructions with fewer artifacts.

Relevance to LLNL Mission

X-ray tomography is a workhorse in LLNL's NDE capabilities. X-ray array sources may constitute leading edge technology in NDE. This project is underway to determine if there is a role for array sources and what it would be in terms of maintaining LLNL's NDE leadership.

FY2010 Accomplishments and Results

The acquisition of x-ray array source data was obtained through a collaboration with Triple Ring Technologies, a research, development, and array source and detector system manufacturing

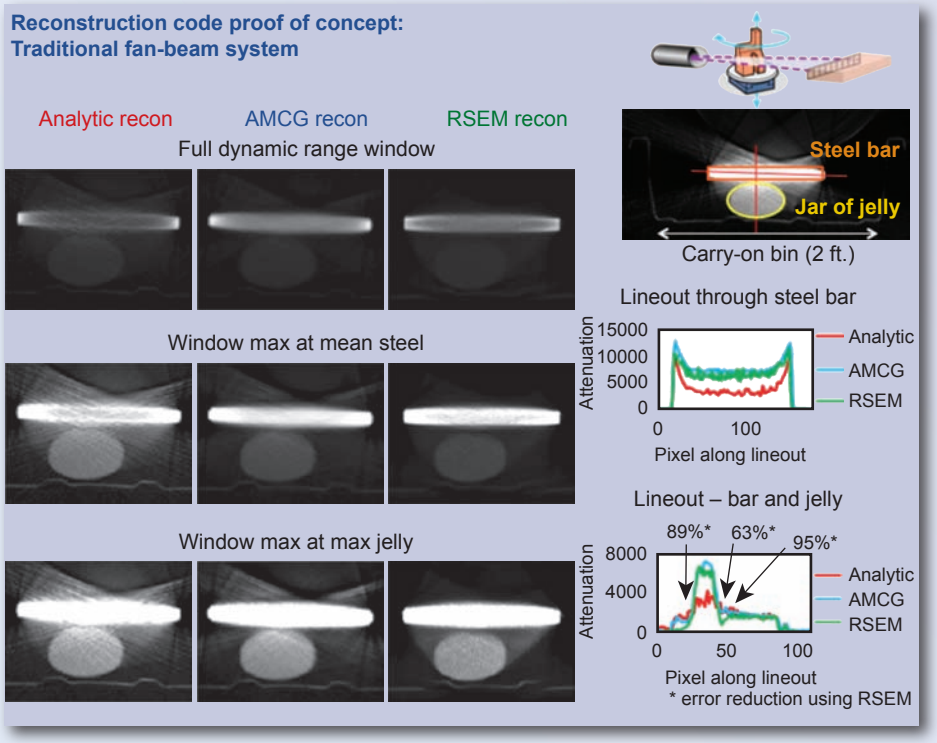

Figure 2. **Comparison of algorithms for traditional 2-D cross-sectional data.**

company. The partnership was formalized in FY2010. A Triple Ring Technologies system is presented in Fig. 1.

The project identified and tested three reconstruction algorithms on 2-D array source data for algorithm testing and comparison. The three algorithms were: a traditional analytic method (Filtered Back-Projection (FBP)); the Adjoint Method Conjugate Gradient (AMCG) algorithm developed at LLNL; and the Ordered Subset Expectation Maximization (OSEM) method, which is used widely in the medical imaging field for emission tomographic reconstruction.

OSEM showed a significant impact on reducing artifacts. Particularly evident was a reduction in streak artifacts (>65% reduction in streak artifacts in regions, as shown in Fig. 2). Although OSEM was specifically included in this study because no modification was necessary to reconstruct array source data, it has shown it can also improve the reconstruction of traditionally acquired data as well (reduction in streak artifacts, also shown in Fig. 2).

Two test objects were identified and scanned with the array source: a cylindrically symmetric "As-Built" phantom, and a Contrast and Resolution Interleaved Stacked Plate (CRISP) phantom. The CRISP phantom was designed and manufactured within this project and metrology was performed to determine the ground truth feature sizes and locations for system comparison. The data collected using the Triple Ring array source for both the "As-Built" and CRISP phantoms were reconstructed with OSEM (Fig. 3).

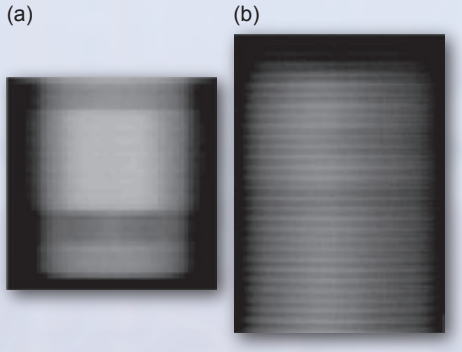

Figure 3. **OSEM reconstructed images for array source-acquired cross-sectional data on both the (a) as-built and (b) CRISP phantoms.**

Multiplexing sources within the array consists of simultaneously activating sources in a predetermined fashion during acquisition. Although currently available systems are not able to acquire data in a multiplexed acquisition mode, to understand whether multiplexing would be useful for LLNL's NDE efforts, the Triple Ring system was modeled and multiplexing simulated. The noise was analyzed in various multiplexing methods as well as the available single-source-at-a-time (single-series) illumination method. Single-series collection methods were found to contain less noise for the data collection rates currently achievable by array source systems.

Related Reference

De Man, B., S. Basu, D. Bequé, B. Claus, P. Edic, M. Iatrou, J. LeBlanc, B. Senzig, R. Thompson, M. Vermilye, C. Wilson, Z. Yin, and N. Pelc, "Multi-Source Inverse Geometry CT: A New System Concept for X-Ray Computed Tomography," *Medical Imaging : Physics of Medical Imaging Proc. of SPIE,* **6510**, 2007.

FY2011 Proposed Work

Instead of acquiring data by rotation and only in a single plane, project goals for FY2011 will investigate a portable, field-ready system by acquiring select views of objects from any vantage (*i.e.,* region-of-interest (ROI) acquisition). Simulations will provide direction for object construction as well as choosing which views to use for ROI imaging. To collect these data, new equipment and acquisition gantries will be necessary, which will be developed and used through a collaboration with Triple Ring and Stanford University.

We will also expand on our work accomplished in FY2010 by acquiring data on the previously investigated phantoms using a 1-D array source system developed by XinRay. All systems (cone-beam, Triple Ring (2-D) array and XinRay array) will then be evaluated.

Low-Energy, Fast-Pulsed, Power-Driven Dense Plasma Focus for WCI and NIF Relevant Experiments

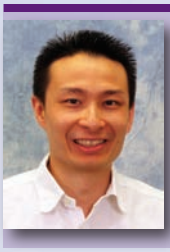

For more information contact:

Vincent Tang
(925) 422-0126
tang23@llnl.gov

In this work we constructed and analyzed a new modular, table-top, low-energy (up to 10's kJ) pulsed-power driver for Dense Plasma Focus (DPF) z-pinch loads that can provide a low-cost means of generating plasma conditions relevant to LLNL's WCI and NIF, the study of primary and secondary boost and laser-plasma interactions (LPI), respectively. Our preliminary models show that relevant plasma conditions with average electron densities greater than 10^{21}/cc and temperatures up to ~10 keV can be reached in a 55-kJ machine approximately 2 m in radius, powered by 10's of modular arms arranged in a circle. Lower energy machines were found to reach some of the relevant conditions. Additionally, a small experiment was constructed and operated with the end goal of validating our models.

Project Goals

The goal of this feasibility project was to examine whether modular, tabletop, low-energy (up to ~10's kJ) pulsed-power systems, using modern off-the-shelf technology, can drive DPF z-pinches to plasma conditions that enable WCI and NIF relevant experiments. The enabling new technologies include new low-inductance, high-voltage capacitors and transmission lines, along with fast high-current switches. Figure 1 illustrates the device and concept, along with some of the enabling technologies.

Relevance to LLNL Mission

The ability to reach plasma conditions useful for LLNL missions in a tabletop format will enable significantly more experiments to be performed and more data to be collected. A secondary objective is the possibility of using these devices for neutron or accelerator sources for Global Security applications.

FY2010 Accomplishments and Results

In FY2010, we built and exercised models of modular tabletop Marx pulsed-power drivers to study this topic.

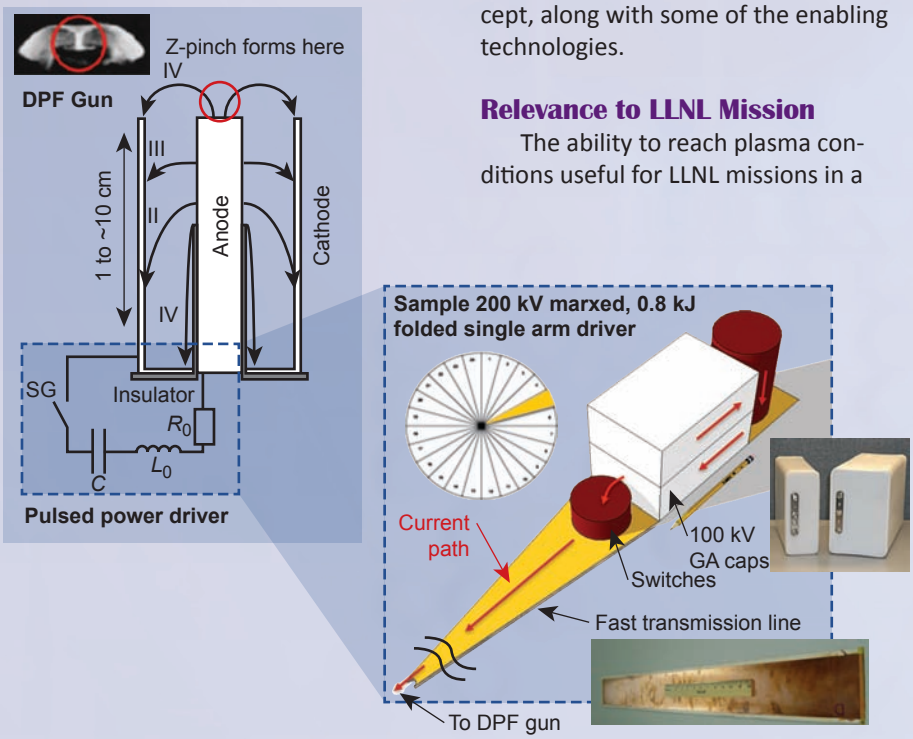

Figure 1. Left: DPF gun driven by a switched capacitor bank. Right: New modular Marx driver concept using new pulsed-power technologies. By shortening the pulse-width through low inductance and resistance, higher peak currents can be delivered at lower total energy and driver size.

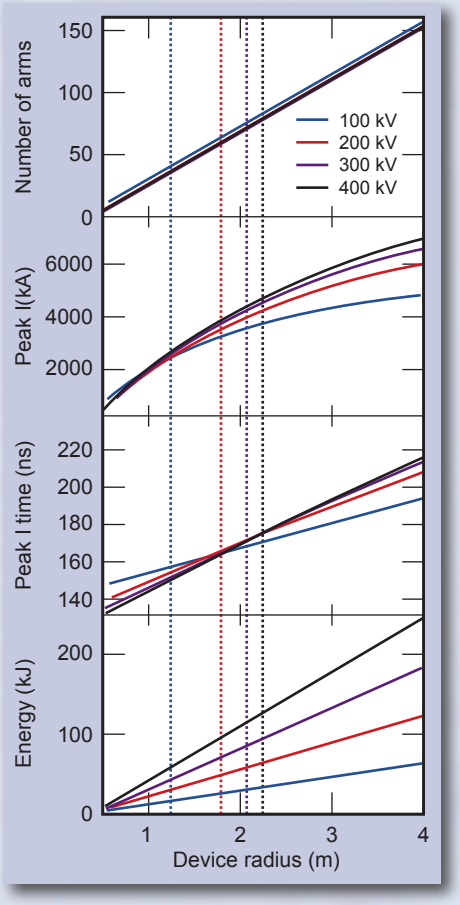

Figure 2. Key parameters of the modular driver concept in Fig. 1 as a function of total pulser radius. The different curves on each plot are for drivers with different Marx setups.

We studied a multi-arm circular driver to maximize current as a function of size at 100 to 400 kV. We showed analytically and through full circuit simulations that a multi-arm driver can be represented as a lumped RLC circuit.

Figure 2 provides short-circuit performance of several drivers as a function of size and voltage using modern components. These models were coupled to a version of our three-phase DPF z-pinch model, which allowed us to perform scans of engineering parameters to determine achievable plasma conditions.

Figure 3 shows relevant plasma regimes that can be achieved with a 2-m radius, 69-arm, 200-kV driver with various gun geometries. Data for plasma regimes using loads for only 2 and 8 of the 69 arms are also shown. Overall, the modeling shows that it should be possible to achieve relevant plasma conditions with a low-energy machine at tabletop dimensions on the order of ~3–4 m due to newer pulsed-power technology. This is an improvement over previous leading machines with 8-m diameter footprints.

We constructed, from existing components, a small, up to 200-J DPF device to enable experiments to validate our model. Figure 4 shows the 1-arm 100-kV pulsed-power driver equipped with a simple self-break oil switch and a starting DPF gun load. Figure 5 shows sample short circuit data from the driver with a simple RLC fit, along with dI/dt data indicating pinch formation and particle emission from initial experiments.

Related References

1. Tang, V., M. L. Adams, and B. Rusnak, "Dense Plasma Focus Z-pinches for High Gradient Particle Acceleration," *IEEE Transactions on Plasma Science,* **38**, 4, pp. 719–727, 2010.
2. Decker, G., W. Kies, M. Malzig, *et al.*, "High Performance 300 kV Driver Speed 2 for MA Pinch Discharges," *Nuclear Instruments and Methods,* **A249**, 1986.
3. Soto, L., "New Trends and Future Perspectives on Plasma Focus Research," *Plasma Phys. Cont. Fusion,* **47**, 5A, p. A361, 2005.

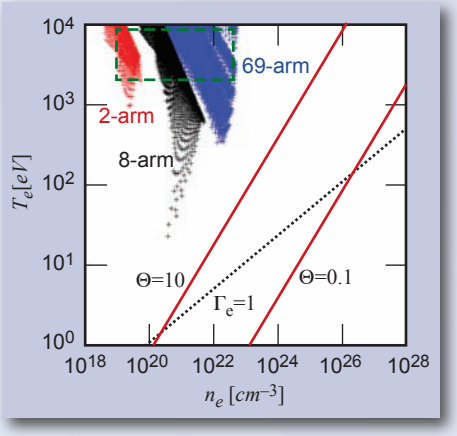

Figure 3. Plasma temperature and densities reached in our simulations for various gun geometries with dimensions on the ~cm scale. The black dotted line is the electronic coupling parameter; below the line the plasma is strongly coupled. The red lines are the electron degeneracy parameter; below Θ = 0.1 degeneracy effects dominate, and above Θ = 10 degeneracy effects are negligible. The green dashed box indicates conditions of interest to NIF LPI studies.

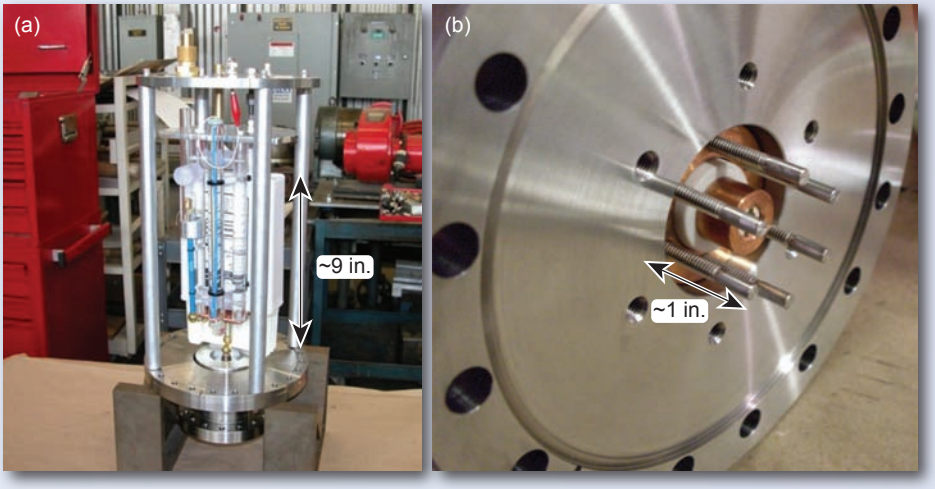

Figure 4. (a) Small, 100-kV, 200-J pulsed-power driver and (b) DPF gun. The experiment used existing equipment with the objective of validating our code at low energies.

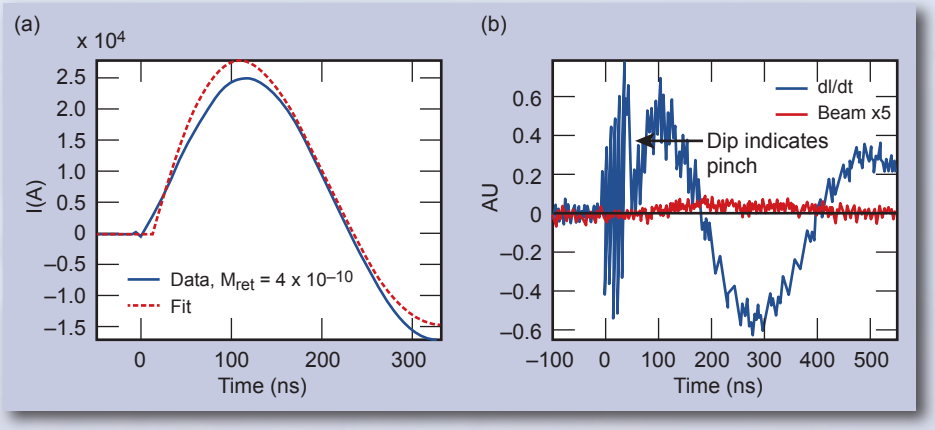

Figure 5. (a) Short circuit current profile of the driver in Fig. 4 at 64 kV and 82 J. A peak current of ~25 kA was reached with a rise time of ~100 ns. (b) Raw dI/dt data from the DPF gun in Fig. 4.

Applying High-Resolution Time-Domain Radiation Detection Techniques to Low-Resolution Data

For more information contact:

Brian L. Guidry
(925) 422-1661
guidry1@llnl.gov

The Statistical Radiation Detection System (SRaDS) is a software system for detecting specific radioactive materials from their characteristic gamma-ray emissions. Each year more than 16 million cargo containers arrive in the United States and the detection of illicit radioactive materials hidden within the cargo is perhaps the most technically and logistically challenging problem facing the Homeland Security community.

The SRaDS system processes gamma-ray photon arrivals individually as they arrive at a detector. For each photon arrival, a decision function is calculated based on its energy and inter-arrival time. The value of the decision function is then compared to thresholds set by the user for a given radionuclide. The thresholds are calculated from the detection and false alarm probabilities required by the user. If the function value goes below the lower threshold, the radionuclide is declared not present. If it goes above the upper threshold, the radionuclide is declared present. If neither occurs, more data is required to reach a decision at the desired level of performance (Fig. 1).

Project Goals

To date, SRaDS processing has been successfully applied only to data collected from high-resolution HPGe detectors. Our goal was to apply the underlying approach to data collected using lower-resolution sodium iodide (NaI) detectors, by far the most ubiquitous type of radiation detector on the market today.

Relevance to LLNL Mission

LLNL has a long history of working with others in government as well as

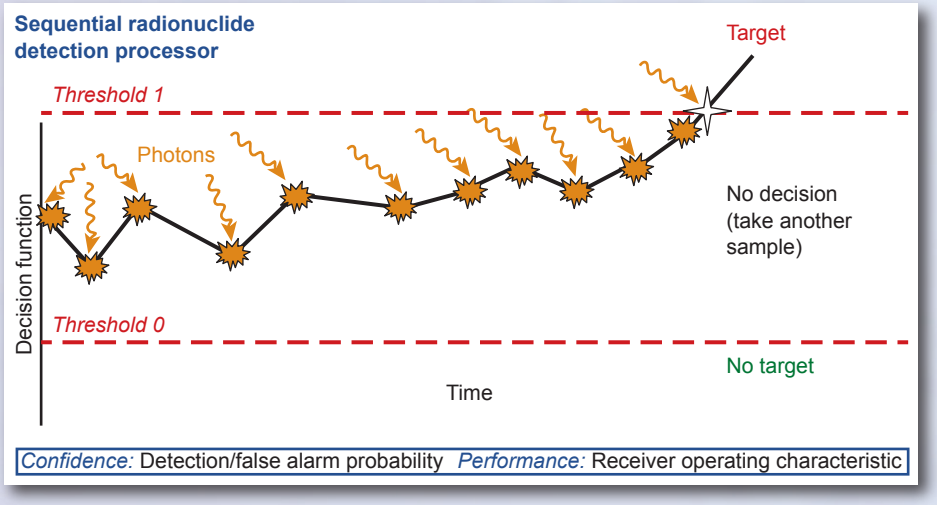

Figure 1. Operation of a sequential processor. A decision function is calculated at each discriminated photon arrival. This is compared to two thresholds, one for positive detection and the other for negative detection.

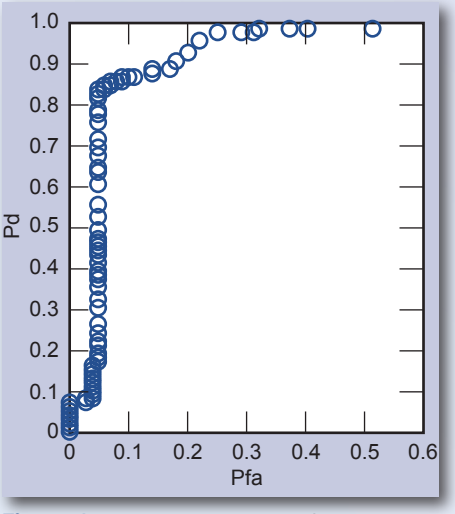

Figure 2. Receiver Operating Characteristic curve for NaI data.

our partners in industry to find solutions for the problems involved in monitoring for illicit proliferation activities as well as monitoring for treaty verification. To that end, the SRaDS system was created to help address these challenging issues.

FY2010 Accomplishments and Results

NaI data collected during previous work was extracted and arranged in a format suitable for use by SRaDS. Two types of event-mode sequence (EMS) data were used: data with a target source present and data consisting of only background. The high-resolution SRaDS algorithm was then re-targeted for the lower resolution NaI data. Receiver Operating Characteristic (ROC) curves describing probabilities of detection and false alarm are shown in Fig. 2. An operating region for the detection software was selected. Using threshold values derived from the operating region, SRaDS was run again on the extracted data and comparisons were made between the target performance of the system and the actual performance (Figs. 3 and 4, and Tables 1 and 2).

Related References

1. Candy, J. V., E. Breitfeller, B. L. Guidry, D. Manatt, K. Sale, D. Chambers, M. A. Axelrod, and A. Meyer, "Radioactive Contraband Detection: A Bayesian Approach," *Proc. OCEANS09, IEEE OES Soc.,* 2009.

2. Candy, J. V., E. Breitfeller, B. L. Guidry, D. Manatt, K. Sale, D. H. Chambers, M. A. Axelrod, and A. M. Meyer, "Physics- Based Detection of Radioactive Contraband: A Sequential Bayesian Approach," *IEEE Trans. on Nuclear Science,* **56**, 6, 2, pp. 3694–3711, 2009.

FY2011 Proposed Work

The true strength of the SRaDS processing technique lies in our ability to effectively use the information contained in down-scattered photon arrivals. The next step is to continue working on our low-resolution detector capabilities with a particular interest in using photons in the Compton continuum.

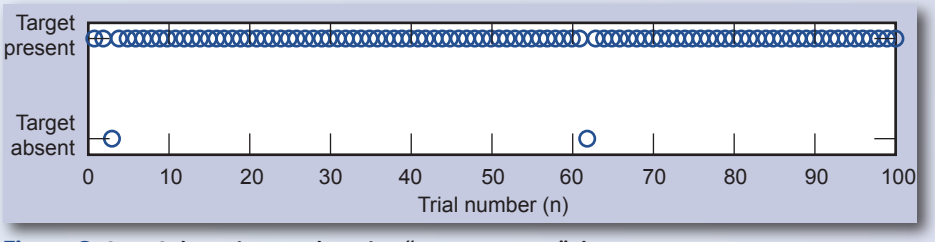

Figure 3. SRaDS detection results using "Target Present" data.

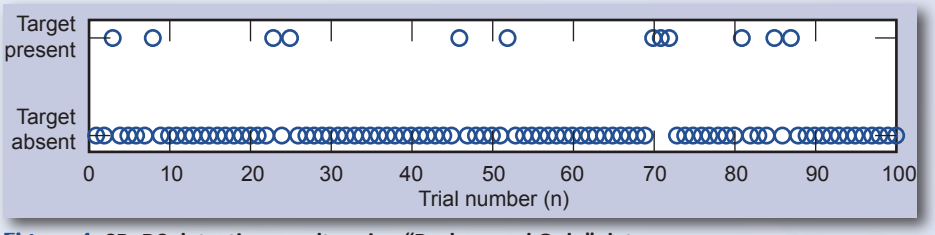

Figure 4. SRaDS detection results using "Background Only" data.

Table 1. Comparison of desired operating characteristics with actual SRaDS performance using "Target Present" data.

	Operating Region	Actual Performance
Probability of detection of target present (Pd)	>90%	98%
Probability of miss (Pmiss)	<5%	2%

Table 2. Comparison of desired operating characteristics with actual SRaDS performance using "Background Only" data.

	Operating Region	Actual Performance
Probability of false alarm (Pfa)	<20%	12%
Probability of correctly identifying background only	>90%	88%

Flexible Testbed for 95-GHz Impulse Imaging Radar

For more information contact:

Christine N. Paulson
(925) 423-7362
paulson4@llnl.gov

During the 1990s, Lawrence Livermore National Laboratory (LLNL) was funded by the Naval Air Warfare Center to develop a 95-GHz high-frequency, ultra-wideband (UWB) radar as a diagnostic tool for extending the lifetime of the rotor bearings and blades of the V-22 Osprey tiltrotor aircraft. Numerous emerging applications could benefit from this technology.

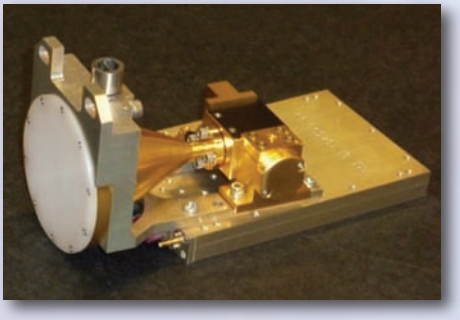

Figure 1. V-22 diagnostic radar prototype hardware system.

Project Goals

The primary objective is to establish a flexible and reconfigurable high-frequency radio frequency testbed that will enable feasibility studies for new applications relating to DOE, DoD, and LLNL programs. To implement this, we restored the 95-GHz UWB radar prototype to an operational state and upgraded its obsolete timing and processing systems.

Relevance to LLNL Mission

There is renewed interest in the use of high-frequency pulsed radar systems for a variety of DOE, DoD and LLNL applications. As an initial target goal for this effort we chose to focus the retooling of the 95-GHz UWB radar technology to support feasibility studies in standoff explosive detection. Other potential uses of pulsed 95-GHz radar systems, which can offer high (*i.e.*, submillimeter) resolution include

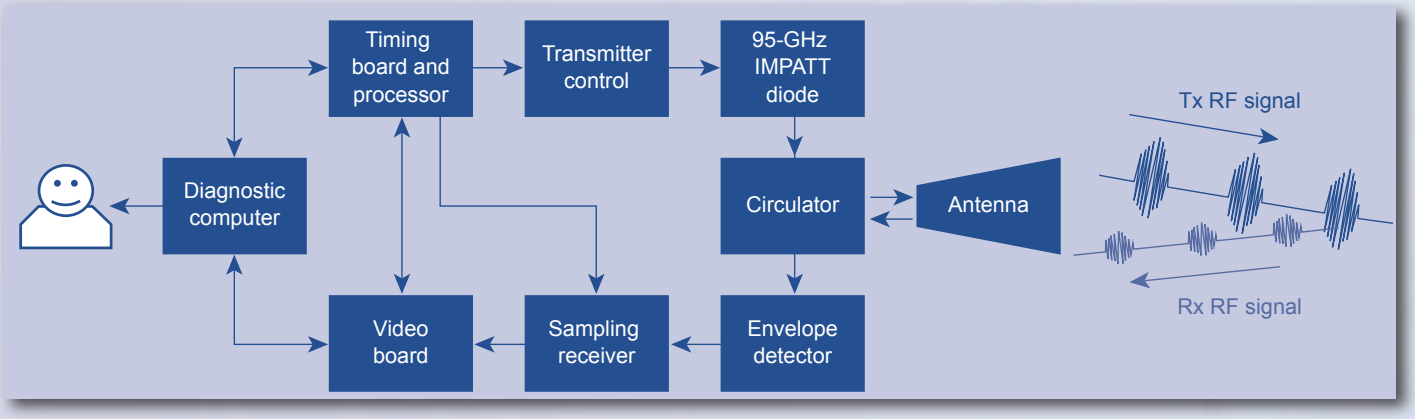

Figure 2. Functional block diagram for V-22 diagnostic radar prototype.

standoff imaging, nondestructive evaluation, vibration detection and analysis, materials characterization, surface mapping, vital signs monitoring, and small projectiles tracking.

The construction of fieldable radar systems operating near 100 GHz is costly and requires technicians skilled in the art. Many outside entities lack the resources to perform feasibility studies involving high-frequency radar. However, the restoration of LLNL's 95-GHz radars will provide a flexible and reconfigurable high-frequency radio frequency testbed and enable LLNL to work with outside groups such as government agencies and universities on new applications in a cost-effective manner.

FY2010 Accomplishments and Results

The original V-22 diagnostic radar prototype and its functional block diagram are shown in Figs. 1 and 2. The most significant modification required to make a versatile high-frequency radar testbed from the existing prototype was to replace the existing timing control, data acquisition, and data processing hardware with modern, software reconfigurable circuitry. In its original form, the timing signals, data acquisition, and data processing functions were self-contained within a MicroChip PIC 17C756 microcontroller and a digital timing board for the very specific V-22 application requirements. This made it difficult to change radar settings or access the received radar data for other applications and studies. In addition, while it was the state of the art at its time, this 33-MHz, 8-bit microcontroller with limited data and programming memory is obsolete today.

By upgrading the timing system, we have the capability to electronically control the sweep position and range parameters of the radar. We replaced some of the functionality of the digital board with an add-on radar controller board, shown in Fig. 3. This controller taps into the timing signals on the original digital control board inside the radar, enabling the configuration of the radar to be rapidly changed using a software application. In addition, the board contains a USB interface, allowing the connection to modern computer systems and improving the data acquisition functionality of the radar. Now, instead of processing the data using hard-coded algorithms within the PIC processor, data can be exported to software applications running on a computer for more advanced and more easily reconfigurable processing algorithms. These changes enable the customization of the radar operating parameters and provide easy access to the raw data captured by the radar.

Recently, LLNL teamed with a group at the University of South Carolina (USC) to conduct feasibility studies combining laser spectroscopy with microwave technologies for standoff identification of high-explosive vapors and residues (*e.g.*, radar resonance-enhanced multiphoton laser ionization (RADAR-REMPI)). Microwave devices were used, ranging from 10.5 to 26 GHz, to detect *in situ* the formation of laser-induced plasmas by microwave reflection and scattering over ranges of 10s of centimeters, as shown in Fig. 4. To increase the sensitivity of the USC studies to achieve longer standoff detection ranges, LLNL is investigating the use of higher RF frequencies for their REMPI-based standoff detection work. Certain LLNL elements have significantly improved the signal-to-noise ratio of the RADAR-REMPI setup. Currently, we are conducting in-house plasma measurements, shown in Fig. 5, with plans to combine the newly restored 95-GHz radar testbed with the USC group's REMPI technique for longer-range standoff detection of REMPI plasmas.

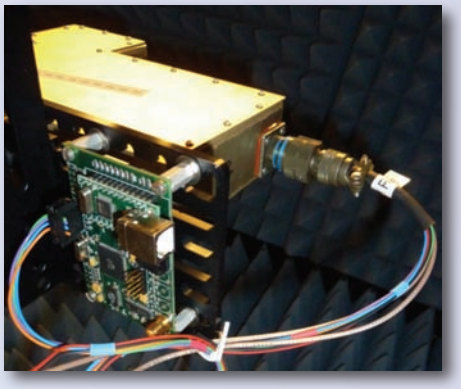

Figure 3. Modified high-frequency radar with external controller.

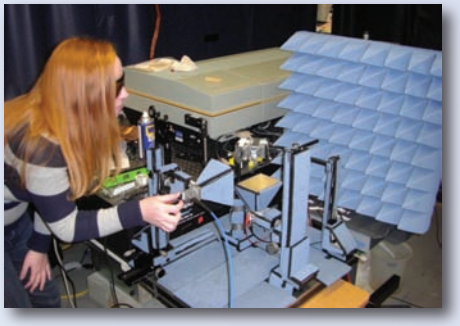

Figure 4. USC microwave plasma detection apparatus being tuned.

Figure 5. Standoff signal-to-noise characterization data collection on a plasma using LLNL's 95-GHz flexible UWB radar test.

Engineering Systems for Knowledge & Inference

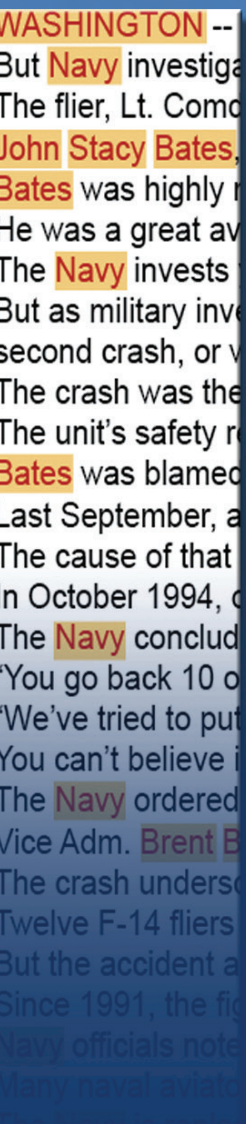

Toward Understanding Higher-Adaptive Systems

For more information contact:

Brenda M. Ng
(925) 422-4553
ng30@llnl.gov

This project is a two-year research effort that seeks to understand higher-adaptive systems, which are systems that can modify their structures and behaviors in response to attempts at detection or regulation. These systems are ubiquitous: in the real world, there are many entities, such as money launderers and cyber intruders, whose fundamental behavior changes upon probing or intervention by an observer. Such a system outputs observations (*e.g.,* an unintentional trail of evidence connected to its activities) and adversarial actions (*e.g.,* direct assaults/countermoves against its opponent). In particular, these actions can span a spectrum of aggression, from limiting information available to its opponent to misleading the opponent into making the wrong moves or decisions.

Project Goals

The objective of this work is to explore and extend as necessary current decision-theoretical frameworks and algorithms for solving real-world adversarial problems, especially those involving adversaries that are higher-adaptive. The results of this work can provide foundational knowledge for building a computationally efficient framework that can characterize and respond to dynamically changing, deceptive adversarial systems. This knowledge will be invaluable for future studies of even more adaptive and aggressive adversarial systems, such as those that limit resources as well as information from their opponents. This type of study will have scientific merit in both the artificial intelligence and game theory communities; it also provides the basis for addressing significant national security threats.

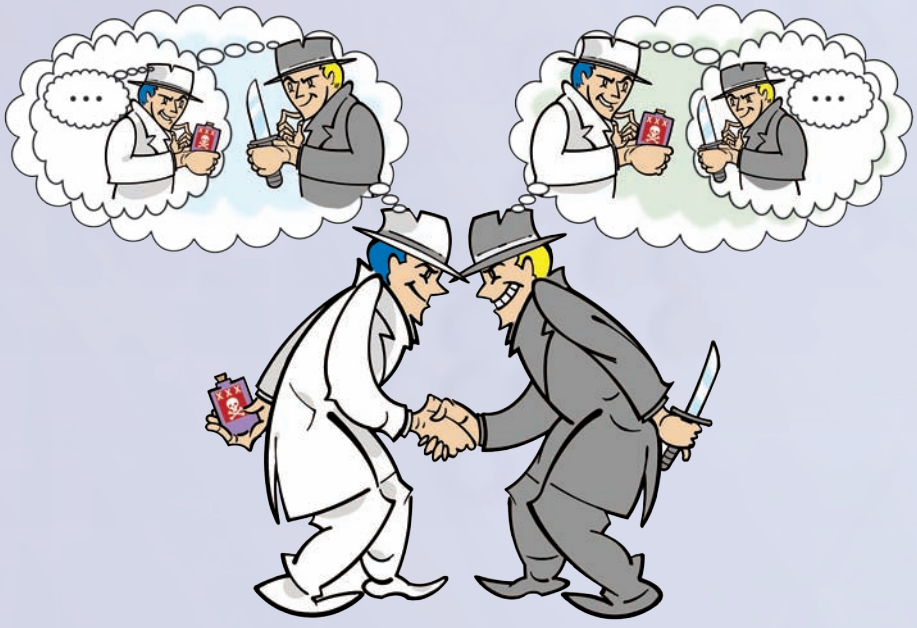

Figure 1. Illustration of human adversaries "gaming" against each other. To adequately respond in a realistic adversarial situation, it is important to model the adversary as an intentional agent, who anticipates its opponent's counteractions in its strategies.

Relevance to LLNL Mission

This research effort directly supports the Cyber, Space, and Intelligence thrust area in LLNL's Five-year Strategic Roadmap. This work can provide important insights about real-world adversarial modeling and higher-adaptive systems, with applications in law enforcement (*e.g.,* money laundering and drug trafficking), homeland security (*e.g.,* terrorist networks), cyber security, and nonproliferation.

FY2010 Accomplishments and Results

In FY2009, our work was driven by a money laundering application, an extremely pervasive crime in which the funds from illegal activity are disguised to appear legitimate. We formulated a simplified model of money laundering using an interactive partially observable Markov decision process (IPOMDP). In an IPOMDP, each agent maintains beliefs about the physical states of the environment, and the models of other agents (*e.g.,* how each of them might perceive or act in the same environment). This makes IPOMDP especially relevant for adversarial modeling in that it incorporates the notion of nested intent into the belief of each agent, allowing for the modeling of agents that "game" against each other (see Fig. 1).

From this work, we gained insights about the capability gaps required for IPOMDPs to be applied in real-world settings. One deficiency with the standard IPOMDP is its assumption that agents are privy to the knowledge of model parameters, when these parameters are often unknown in real-world scenarios. Our FY2010 contribution is the proposal of a new framework called the Bayes-Adaptive IPOMDP (BA-IPOMDP), which augments the IPOMDP with model-learning capabilities. Our approach is to assume that the

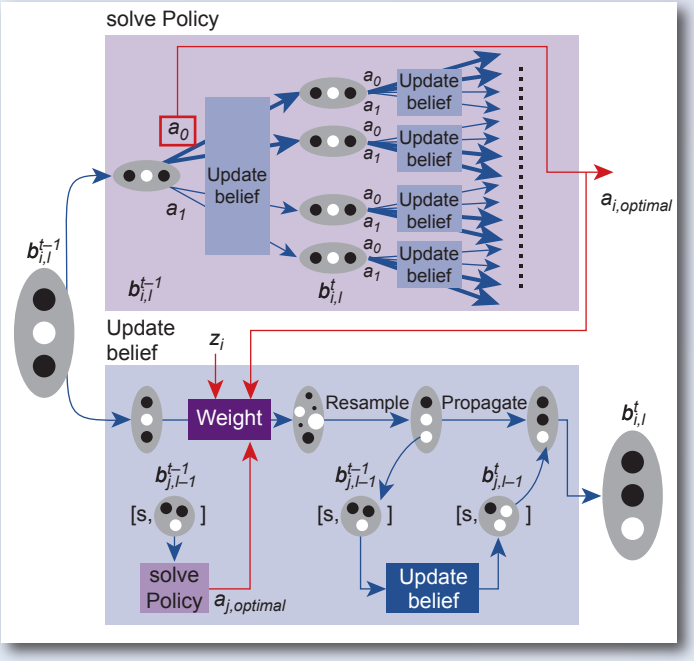

Figure 2. Representation of beliefs, approximated by samples over the physical states and "counts" that parametrize the model. Beliefs are updated via interactive particle filtering, which entails a recursive procedure.

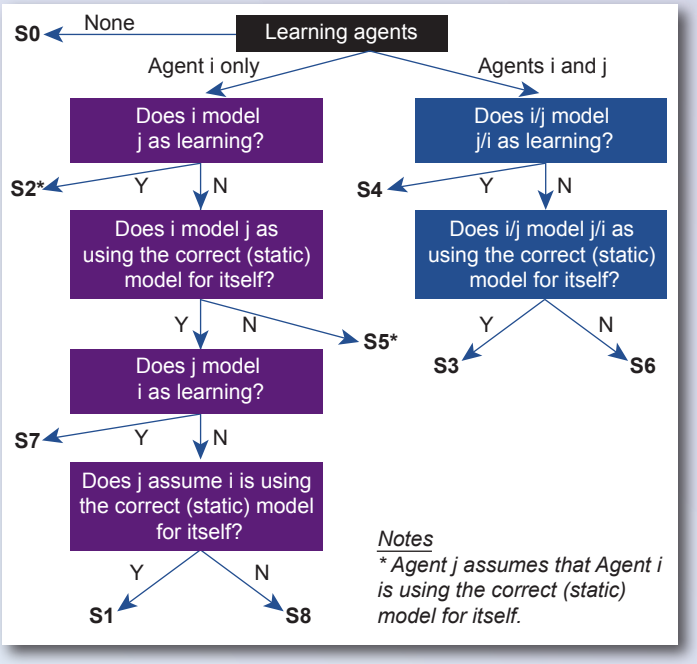

Figure 3. Nine scenarios are considered, differing according to which agent is learning and what it assumes of its opponent's capabilities.

state, action, and observation spaces are finite and known, but the model parameters (namely, the state transition probabilities and the observation probabilities) are not fully known. We include these parameters as part of the state space and maintain beliefs, in the form of probability distributions, to represent our uncertainty about these parameters and the physical state of the environment.

At each time step, an agent searches for and executes the optimal action given its current belief. When it receives an observation, it uses this observation to iteratively refine its estimate of the state transition and observation models, and applies these learned models to update its belief about the physical state of the environment. During this process, the agent must anticipate the action, observation, and belief update of its opponent. Thus, belief updates are recursive.

To solve an IPOMDP is to determine the optimal policy, which for every possible observation, produces an optimal action that maximizes the agent's expected reward. Previous work has shown that value iteration can be used to solve IPOMDPs.

In FY2009, we introduced approximations such as the interactive particle filter (I-PF) to address the curse of dimensionality (belief complexity that increases with the number of states), and reachability tree sampling (RTS) to address the curse of history (policy complexity that increases with number of time steps or horizons in the decision process).

In FY2010, we optimized I-PF to compute an approximation to the BA-belief, and we used RTS to construct a pruned version of the finite-horizon reachability tree and applied dynamic programming to search this tree for the optimal policy (see Fig. 2).

To evaluate the performance of these methods, we tested our algorithms against a popular academic problem, known as the multiagent Tiger problem, over multiple scenarios (see Fig. 3). Runtime was recorded for varying resolutions of the approximation algorithms; average rewards and model parameter convergence was compared for different learning scenarios.

Baselining against the standard IPOMDP, we found that 1) the agent quickly converges on a model which is slightly off the true model; 2) the average rewards and model convergence depend on how accurately the agent models its opponent's learning process; and 3) the parameter learning introduced by our BA-IPOMDP significantly improved the agent's initial estimate of the model parameters while maintaining reasonable runtime. The ability to incorporate learning into these models brings us one step closer to their applicability in realistic adversarial modeling.

Related References

1. Ng, B., C. Meyers, K. Boakye, and J. Nitao, "Towards Applying Interactive POMDPs to Real-World Adversary Modeling," *Proceedings of the 22nd Innovative Applications of Artificial Intelligence Conference*, pp. 1814–1820, 2010.
2. Doshi, P., and P. Gmytrasiewicz, "Monte Carlo Sampling Methods for Approximating Interactive POMDPs," *Journal of Artificial Intelligence Research*, **34**, pp. 297–337, 2009.
3. Ross, S., B. Chaib-draa, and J. Pineau, "Bayes-Adaptive POMDPs," *Proceedings of the 21st Neural Information Processing Systems*, pp. 1225–1232, 2008.

Enhanced Event Extraction from Text via Error-Driven Aggregation Methodologies

For more information contact:

Tracy D. Lemmond
(925) 422-0219
lemmond1@llnl.gov

Knowledge discovery systems are designed to construct massive data repositories using text and information extraction methodologies, and then infer knowledge from the ingested data, allowing analysts to "connect the dots." The extraction of relational information (*e.g.,* triples, events) and related entities (*e.g.,* people, organizations) often forms the basis for data ingestion. Unfortunately, these systems are particularly vulnerable to errors introduced during the ingestion process, frequently resulting in misleading or unreliable analysis. Though state-of-the-art extraction tools may achieve insufficient accuracy rates for practical use, not all extractors are prone to the same types of error. This suggests that substantial improvements might be achieved through appropriate combinations of existing extraction tools, provided their behavior can be accurately characterized and quantified.

Our research is addressing this problem through the aggregation of extraction tools based on a general inferential framework that exploits their strengths and mitigates their weaknesses.

Project Goals

The objective of this effort is to develop a significantly improved entity/event extraction system that enables 1) greater insight into the downstream effects of extraction errors; 2) more accurate automatic text extraction; 3) better estimates of uncertainty in extracted data; 4) effective use of investments by the Natural Language Processing community; and 5) rapid incorporation of future advancements in extraction technologies.

An extensive analysis of the error processes of individual extractors has yielded insights into their synergistic and conflicting behaviors that have been leveraged to configure a collection of base extractors, through a general inferential framework, into an aggregate meta-extractor with substantially improved extraction performance (Fig. 1).

Relevance to LLNL Mission

Nonproliferation, Counterterrorism, and other national security missions rely on the acquisition of knowledge that is buried in unstructured text documents too numerous to be manually processed. Systems are under development by LLNL and its customers that must automatically extract critical information from these sources. To enable effective knowledge discovery,

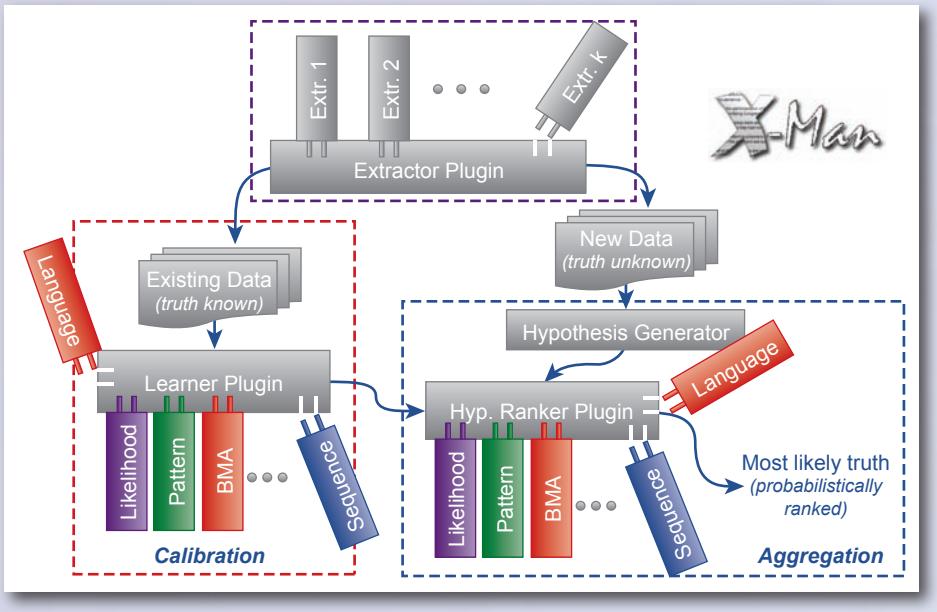

Figure 1. Meta-extraction system.

however, extraction error rates must be driven down. Probabilistic aggregation of extractors is a promising and innovative approach to accomplishing this goal. This effort directly supports Engineering Systems for Knowledge and Inference (ESKI) Text to Inference area and the Cyber, Space, and Intelligence strategic mission thrust in the LLNL Five-year Strategic Roadmap. Successful completion of this research will provide highly valued and unprecedented inference and decision-making capabilities to internal programs, such as IOAP and CAPS, and to external customers such as DHS, DoD, and the intelligence community.

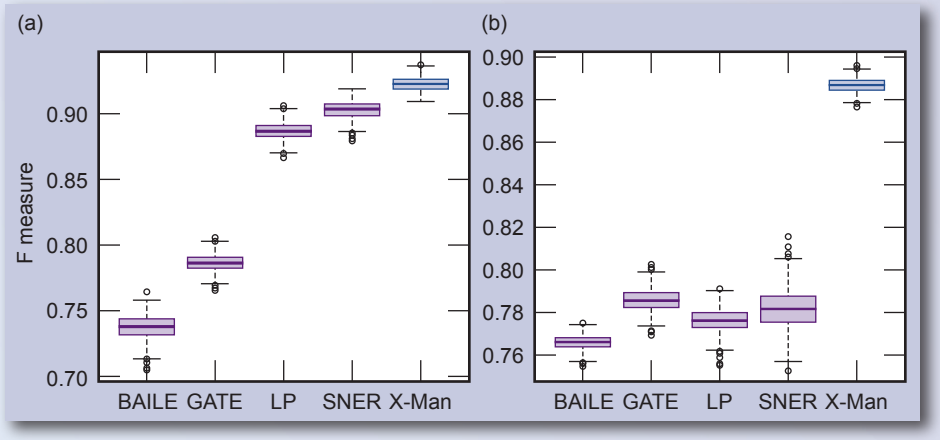

Figure 2. Box plots showing bootstrapped samples of the weighted mean of F measure. Extractors and X-Man were trained on MUC6 (Message Understanding Conferences). Results are shown for testing on (a) MUC6 and (b) CoNLL-2003.

FY2010 Accomplishments and Results

Insights gained in event extraction error analyses performed in FY2008 motivated a graduated approach to triple/event aggregation that is founded fundamentally on the aggregation of extracted entities.

To this end, we have developed a novel text extraction management methodology ("X-Man") focused on entity extraction that can be generalized to multiscale triples (*i.e.,* simple events) and more complex event aggregation solutions. X-Man is a flexible, generalized framework for the aggregation of named entity extraction technologies that uses the joint characteristics of its constituent extractors' output to aggregate extracted text. Hence, existing extraction tools (*e.g.,* commercial, academic) can be readily incorporated to enhance the quality of extracted data. Moreover, the methodology has been designed to enable the incorporation of new extractor evaluation and aggregation methodologies, as well as language modules that can leverage language-specific resources such as gazetteers, stop word lists, and parsers. This unprecedented level of flexibility makes X-Man highly customizable and adaptable to a wide range of applications and problem domains.

X-Man incorporates machine learning and probabilistic methods, ranging from classical probability to Bayesian Model Averaging, into several novel algorithms, each consisting of a calibration component coupled with an aggregation component (Fig.1).

For each of these algorithms, calibration hinges on the estimation of probability distributions over a joint hierarchical error space arising from the suite of underlying extractors. The generated error distributions characterize each extractor's performance relative to disjoint regions of contiguous text. Performance takes into account joint extractor characteristics, as well as the statistical behaviors (both individual and joint) of the errors occupying the defined error space. These algorithms are particularly distinguished by their reliance on a range of underlying models and/or assumptions. Accordingly, X-Man's final stage of calibration involves using state-of-the-art machine learning methods to determine an optimal deployment strategy for incoming data.

When newly extracted output data are encountered, the X-Man System constructs a space of hypotheses over ground truth for each piece of contiguous text and then deploys the text to its optimal aggregation algorithm, which assigns a probability to each ground truth hypothesis. The resulting relative ranking of hypotheses for each piece of text provides not only an ordered list of the most probable ground truths, but a mechanism for determining those hypotheses that are *significantly* more likely in a statistical sense. Thus, the ranking informs downstream decision-making and analysis by enabling confidence assessments of extracted data.

Figure 2 shows sample test results.

X-Man has been shown to 1) produce statistically significant improvements in extraction relative to standard performance metrics (up to 120% improvement under certain operating conditions); 2) be able to reconstruct truth when all of its constituent extractors fail; and 3) provide a framework for quantifying uncertainty in extracted output. Moreover, mechanisms have been developed to help X-Man adapt to sparse data conditions.

Related Reference

Lemmond, T., N. Perry, J. Guensche, J. Nitao, R. Glaser, P. Kidwell, P., and W. Hanley, "Enhanced Named Entity Extraction via Error-Driven Aggregation," *International Conference on Data Mining*, Las Vegas, Nevada, July 2010.

Robust Ensemble Classifier Methods for Detection Problems with Unequal and Evolving Error Costs

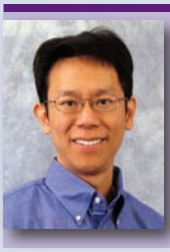

For more information contact:

Barry Y. Chen
(925) 423-9429
chen52@llnl.gov

Successful analysis in real-world detection applications often hinges upon the automatic collection of massive amounts of data over time. However, the pace of automatic data collection far exceeds our manual processing and analysis capabilities, making automated pattern detection in streaming data critical. Machine learning classifiers capable of detecting patterns in datasets have been developed to address this need, but none can simultaneously address the many challenging characteristics of real-world detection problems.

The costs associated with false alarms and missed detections are frequently unequal, extreme (demanding near-zero false alarm or miss rates) or changing over time. Moreover, the underlying data distribution modeled by the classifiers may also evolve over time, resulting in progressively degraded classification performance.

We are addressing these deficiencies through the development of new dynamic ensemble classifier algorithms that leverage diverse cost-sensitive base classifiers.

Project Goals

The ultimate goal of this two-year effort focuses on the understanding and development of new ensemble learning algorithms that can effectively address the considerable challenges presented by detection problems of national significance. The developed methodologies will yield significantly improved performance at near-zero false alarm (or missed detection) rates and be able to adapt to changing costs and data distributions in a dynamic environment. This research will lead to greater insight into the factors that interact to govern classification performance, including ensemble size, feature dimensionality, and data sampling.

Relevance to LLNL Mission

This research effort directly supports the Cyber, Space, and Intelligence thrust area in LLNL's Five-year Strategic Roadmap. As threats continue to evolve, and relevant data grow in size and complexity, the capability to automatically detect threat signatures in data becomes increasingly more critical. Real-time situational awareness is paramount and requires dynamic learning systems that maintain high detection performance as misclassification costs and data distributions change over time. Our research explicitly addresses these needs in cyber, counterterrorism, nonproliferation, and national security missions for a broad range of customers, including the IC, DHS, DOE, DoD, and NNSA.

FY2010 Accomplishments and Results

In FY2010, we extended the traditional ensemble classifier error bound to a class-specific error bound that allowed us to develop the fundamental understanding of the conditions in which ensemble classifiers can be expected to achieve higher detection rates at lower false alarm rates (and vice versa). This led to a counterintuitive finding that there are times when increasing classifier agreement in an ensemble results in higher detection rates at lower false alarm rates (Fig. 1). This theory bore

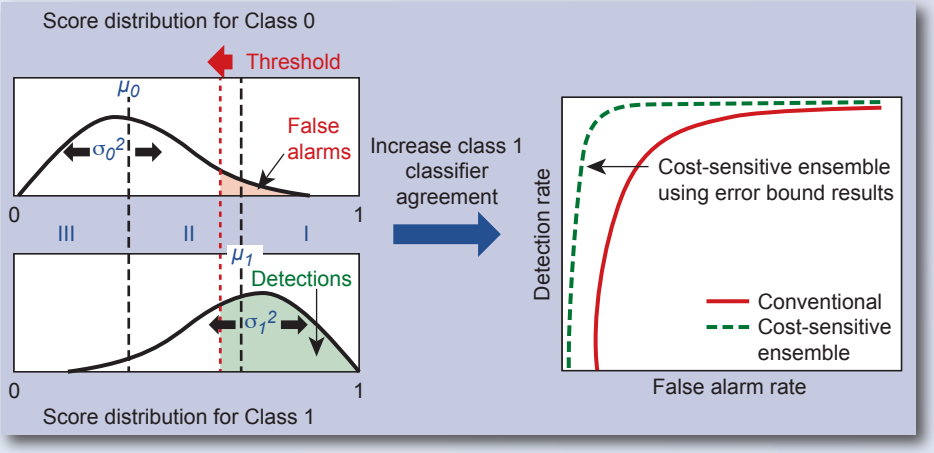

Figure 1. **Class-specific error bounds governing ensemble classification performance. Increasing classifier agreement in the ensemble can lead to higher detection rates at extremely low false alarm rates.**

fruit on a very difficult hidden signal detection application, where our new classifiers were able to achieve a previously unattainable level of performance: non-zero detection rates at 0% false alarms.

In applications where computational resources are scarce, it is extremely important to have ensemble classifiers that are compact and fast. We developed a Bayesian Random Forest to provide high-throughput classification using orders of magnitude fewer bytes. Unlike traditional Random Forests whose trees are grown until homogeneity in data class is reached, Bayesian Random Forests stop growing when the data no longer justifies the increased complexity of adding another layer of split nodes. The Bayesian Random Forest achieved a 32.5 × speedup using two orders of magnitude fewer bytes while maintaining high classification accuracy on an important cyberthreat detection application (see Table).

Bayesian Random Forest compared to a standard Random Forest for cyberthreat detection.

	Standard RF	Bayesian RF
Memory	16 MB	0.021 MB
Classification speed (s)	195	6
Avg. class accuracy	99.1%	98.7%

To address the challenge of changing data distributions, we have developed several new approaches for dynamic density estimation. The Forest Based Density Estimator (FBDE) is an approach inspired by Random Forests whose trees randomly partition feature space into appropriately sized hyper-rectangles. An ensemble of these trees allows for a robust estimate of the probability density of high dimensional data. As data distributions change, the trees in the forest evolve to track changes in the data. Using dynamic density estimators, we developed a classification system that is able to maintain high detection rates at low false alarm rates even as the underlying detection pattern changes.

In Fig. 2, we compare a standard static classifier to our dynamic classification system on a cyberthreat detection application where the threat class undergoes six different changes during the experiment. Our dynamic classifier successfully tracks the changing threat class and significantly outperforms the static classifier over the low false alarm rate regions of the receiver operating characteristic (ROC) curve.

Related References

1. Chen, B. Y., T. D. Lemmond, and W. G. Hanley, "Building Ultra-Low False Alarm Rate Support Vector Machine Ensembles Using Random Subspaces," *Proc. IEEE Symposium on Computational Intelligence and Data Mining*, 2009.
2. Lemmond, T. D., W. G. Hanley, L. J. Hiller, D. A. Knapp, M. J. Mugge, and B. Y. Chen, "Discriminant Random Forest," U.S. Provisional Patent Filed, May 2008.
3. Lemmond, T. D., A. O. Hatch, B. Y. Chen, D. A. Knapp, L. J. Hiller, M. J. Mugge, and W. G. Hanley, "Discriminant Random Forests," *Proceedings of 2008 International Conference on Data Mining*, 2008.
4. Lemmond, T. D., B. Y. Chen, A. O. Hatch, and W. G. Hanley, "An Extended Study of the Discriminant Random Forest," Data Mining Special, *Annals of Information Systems*, **8**, 2010.
5. Prenger, R. J., T. D. Lemmond, K. R. Varshney, B. Y. Chen, and W. G. Hanley, "Class-Specific Error Bounds for Ensemble Classifiers," *Proc. ACM SIGKDD Conference on Knowledge Discovery and Data Mining*, July 2010.

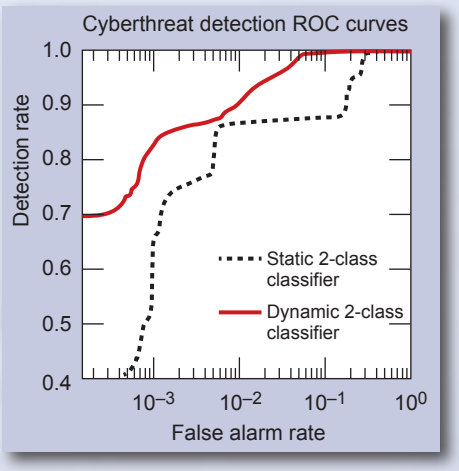

Figure 2. **Our dynamic classifier, which outperforms the traditional static classifier in cyberthreat detection when the threat class undergoes six distinct changes.**

Entity Extractor Aggregation System

For more information contact:

Tracy D. Lemmond
(925) 422-0219
lemmond1@llnl.gov

The extraction of relational information (*e.g.,* triples, events) and entities (*e.g.,* people, organizations) from unstructured text often forms the basis for data ingestion by Knowledge Discovery (KD) systems. These systems enable analysis and inference on massive sets of data and are particularly vulnerable to errors introduced during the ingestion process.

Though state-of-the-art extraction tools often achieve insufficient accuracy rates for practical use, not all extractors are prone to the same types of error. This suggests that improvements may be achieved via appropriate combinations of existing extraction tools, provided their behavior can be accurately characterized and quantified. Several methodologies that combine pattern-based and probabilistic approaches with state-of-the-art machine learning technologies address the entity extraction problem through the aggregation of extraction tools (*i.e., base extractors*).

In FY2009, a prototype of many of these algorithms, within a robust, extensible framework, was constructed, that enables the generation of detailed results and performance assessment data. The focus of the FY2010 effort has been to extend that framework with more advanced aggregation algorithms and to enhance its efficiency, usability, and flexibility for future use in an operational environment.

Project Goals

Key objectives for the system included 1) extending the first generation "plug-and-play" aggregation framework to incorporate ongoing algorithmic advancements; 2) enhancing the flexibility of the framework to allow users greater freedom in experimentation; and 3) streamlining the graphical user interface for greater efficiency and usability.

Relevance to LLNL Mission

Nonproliferation, counterterrorism, and other national security missions rely on the acquisition of knowledge that is buried within unstructured text documents too numerous to be manually processed. Systems are being constructed by LLNL and its customers that must automatically extract entities from these sources, and methodologies have been produced that significantly advance entity extraction capabilities. Bringing these capabilities to an operational status is critical to the timely deployment of knowledge discovery technologies that will impact LLNL mission goals.

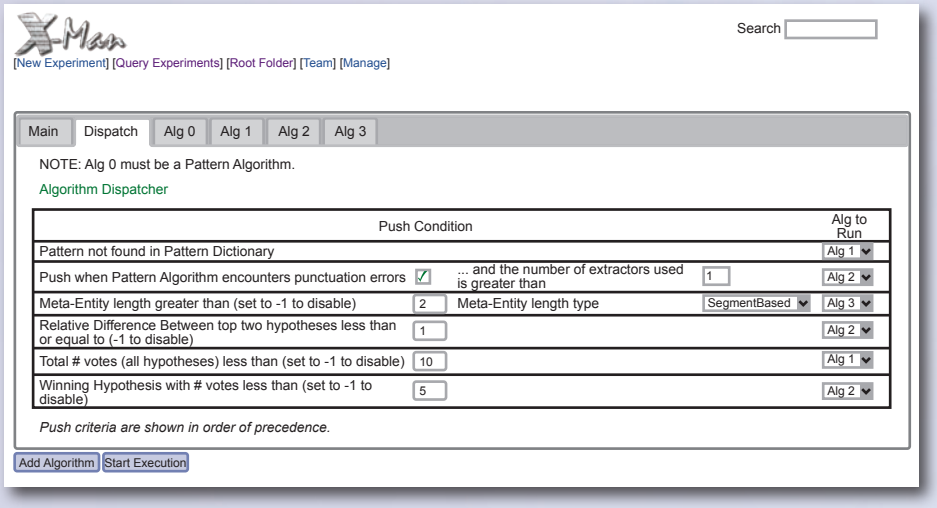

Figure 1. Manual extracted data deployment in X-Man.

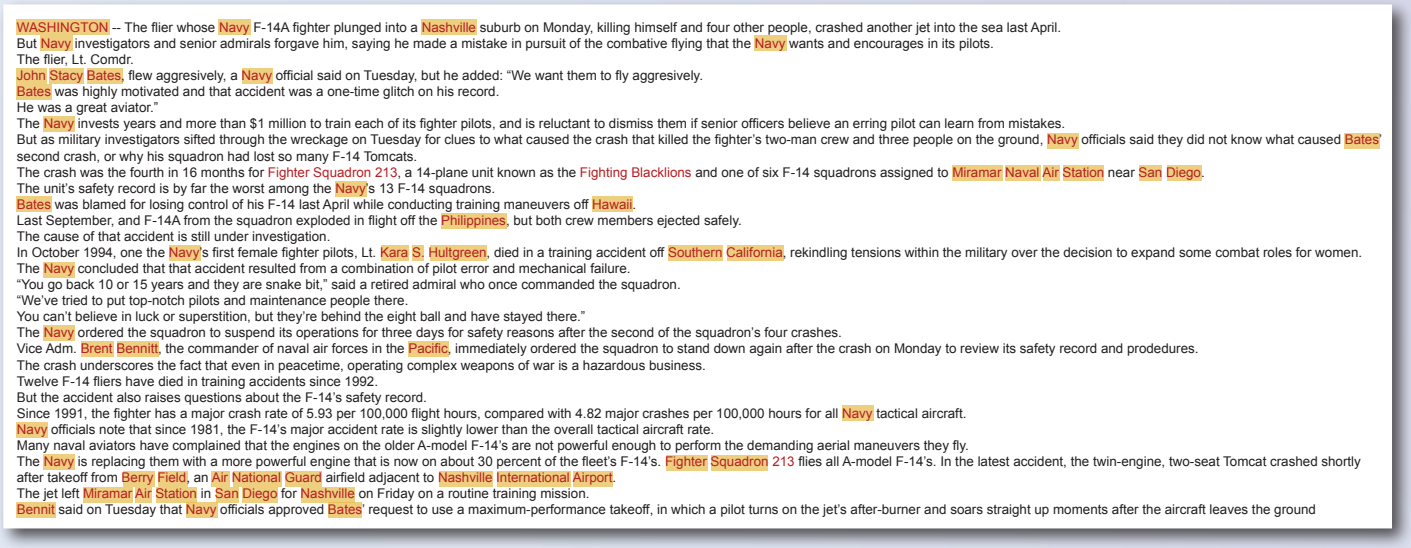

WASHINGTON -- The flier whose Navy F-14A fighter plunged into a Nashville suburb on Monday, killing himself and four other people, crashed another jet into the sea last April.
But Navy investigators and senior admirals forgave him, saying he made a mistake in pursuit of the combative flying that the Navy wants and encourages in its pilots.
The flier, Lt. Comdr.
John Stacy Bates, flew aggresively, a Navy official said on Tuesday, but he added: "We want them to fly aggresively.
Bates was highly motivated and that accident was a one-time glitch on his record.
He was a great aviator."
The Navy invests years and more than $1 million to train each of its fighter pilots, and is reluctant to dismiss them if senior officers believe an erring pilot can learn from mistakes.
But as military investigators sifted through the wreckage on Tuesday for clues to what caused the crash that killed the fighter's two-man crew and three people on the ground, Navy officials said they did not know what caused Bates' second crash, or why his squadron had lost so many F-14 Tomcats.
The crash was the fourth in 16 months for Fighter Squadron 213, a 14-plane unit known as the Fighting Blacklions and one of six F-14 squadrons assigned to Miramar Naval Air Station near San Diego.
The unit's safety record is by far the worst among the Navy's 13 F-14 squadrons.
Bates was blamed for losing control of his F-14 last April while conducting training maneuvers off Hawaii.
Last September, and F-14A from the squadron exploded in flight off the Philippines, but both crew members ejected safely.
The cause of that accident is still under investigation.
In October 1994, one the Navy's first female fighter pilots, Lt. Kara S. Hultgreen, died in a training accident off Southern California, rekindling tensions within the military over the decision to expand some combat roles for women.
The Navy concluded that that accident resulted from a combination of pilot error and mechanical failure.
"You go back 10 or 15 years and they are snake bit," said a retired admiral who once commanded the squadron.
"We've tried to put top-notch pilots and maintenance people there.
You can't believe in luck or superstition, but they're behind the eight ball and have stayed there."
The Navy ordered the squadron to suspend its operations for three days for safety reasons after the second of the squadron's four crashes.
Vice Adm. Brent Bennitt, the commander of naval air forces in the Pacific, immediately ordered the squadron to stand down again after the crash on Monday to review its safety record and prodedures.
The crash underscores the fact that even in peacetime, operating complex weapons of war is a hazardous business.
Twelve F-14 fliers have died in training accidents since 1992.
But the accident also raises questions about the F-14's safety record.
Since 1991, the fighter has a major crash rate of 5.93 per 100,000 flight hours, compared with 4.82 major crashes per 100,000 hours for all Navy tactical aircraft.
Navy officials note that since 1981, the F-14's major accident rate is slightly lower than the overall tactical aircraft rate.
Many naval aviators have complained that the engines on the older A-model F-14's are not powerful enough to perform the demanding aerial maneuvers they fly.
The Navy is replacing them with a more powerful engine that is now on about 30 percent of the fleet's F-14's. Fighter Squadron 213 flies all A-model F-14's. In the latest accident, the twin-engine, two-seat Tomcat crashed shortly after takeoff from Berry Field, an Air National Guard airfield adjacent to Nashville International Airport.
The jet left Miramar Air Station in San Diego for Nashville on Friday on a routine training mission.
Bennit said on Tuesday that Navy officials approved Bates' request to use a maximum-performance takeoff, in which a pilot turns on the jet's after-burner and soars straight up moments after the aircraft leaves the ground

Figure 2. Highlighted extracted and ground truth entities.

This effort directly supports Engineering Systems for Knowledge and Inference (ESKI) Text to Inference R&D area and the Cyber, Space, and Intelligence strategic mission thrust in the LLNL Five-year Strategic Roadmap. The completed system will provide highly valued and unprecedented entity extraction capabilities to internal programs, such as IOAP and CAPS, and to external customers such as DHS, DoD, and the intelligence community.

FY2010 Accomplishments and Results

The entity extractor aggregation tool was originally constructed to serve as both a prototype of first generation aggregation methodologies (*i.e.,* meta-extraction algorithms) and as an environment for the incorporation of these advancements.

In FY2010, the final prototype, called the Extraction Manager (X-Man), contains not only more advanced aggregation algorithms that improved the effectiveness of entity extractor aggregation, but also additional features that enhanced the flexibility provided to its users. Specifically, the new meta-extraction system consists of various modules, linked through a central component called the *dispatcher*, that collectively allow 1) joint characterization of extracted data relative to various features of interest (*e.g.,* entity length, data sparseness, entity type); 2) performance evaluation (in terms of F-measure, exact match, miss and/or false alarm) of aggregation algorithms and extractors relative to these data characteristics; and 3) either manual or automatically optimized deployment of data to the corresponding aggregation algorithms.

Figure 1 shows an example of manual dispatching of extracted entity data to four different algorithms that may be defined by the user. These algorithms may include any of several aggregation algorithms (*e.g.,* Pattern-based, Bayesian Model Averaging), or the base extractors themselves, if desired. Automatic deployment, when selected, is optimized using state-of-the-art machine learning techniques (*e.g.,* ensemble predictors) to determine an optimal mapping of extracted data features to appropriate aggregation and/or base algorithms.

Performance estimation takes place through cross-validation, in which the data are partitioned into multiple folds with associated performance estimates that are typically averaged to obtain an overall estimate. The X-Man tool runs these folds in parallel for increased efficiency. When an experiment has been completed, the user is provided with an array of statistics associated with the execution. These include 1) error counts and probability estimates for the base and meta-extractor algorithms; 2) detailed output of the entities extracted by the base extractors, the space of hypothesized ground truths proposed by the meta-extractor, and the corresponding meta-extractor result; 3) the rate that events of interest occur (*e.g.,* the frequency that the meta-extractor recreates the truth when all base extractors fail); and 4) the original text with extracted and ground truth entities highlighted (Fig. 2).

This information collectively provides substantial insight into the behaviors and performance of the base extractors, as well as of X-Man itself, enabling the potential for algorithm optimization and enhancement.

Related Reference

Lemmond, T., N. Perry, J. Guensche, J. Nitao, R. Glaser, P. Kidwell, P., and W. Hanley, "Enhanced Named Entity Extraction via Error-Driven Aggregation," *International Conference on Data Mining*, Las Vegas, Nevada, July 2010.

Improving Optimization Capabilities for Energy Modeling via High-Performance Computing

For more information contact:

Carol A. Meyers
(925) 422-1252
meyers14@llnl.gov

Energy systems within the United States are expected to undergo a significant transition in the coming decades. These changes are due in large part to the goal of creating a more energy-efficient infrastructure by increasing renewable energy generation and introducing Smart Grid technologies, electric vehicles, and smart appliances. This in turn generates the need for grid models capable of capturing this new paradigm, as well as the need for improved *optimization capabilities*, which can handle the massive size and complexity associated with these future energy scenarios. Currently, grid and dispatch problems are limited to a small number of generators and/or a simplified network topology, which will not be suitable to understand or solve the energy challenges of the future.

As a byproduct of interactions with the California Public Utilities Commission, LLNL was alerted to an energy model currently used for planning in California that suffers from exactly this kind of computational bottleneck. This model is an electric generation dispatch planning model for studying the operational requirements and market impacts of transitioning to a 33% renewable energy standard across the western United States (Figs. 1 and 2). Because many of the decisions (such as turning a generator on or off) associated with grid operations are binary, it is formulated as a mixed-integer linear program. The model's stakeholders have expressed a significant interest in using LLNL expertise and supercomputing hardware to get the model to solve more quickly and eventually add more complexity.

Project Goals

The primary objective of this project is to greatly speed the execution time of the obtained electric generation dispatch planning model. In the process, we hope to demonstrate how LLNL energy modeling expertise and high-performance computing resources can be successfully leveraged to solve large-scale energy problems. Within this context, our specific milestones are as follows: 1) identify where in the planning model the computational bottlenecks are occurring; 2) investigate strategies for reformulating the underlying model to speed execution time; 3) improve performance by demonstrating the ability to run multiple copies of the model in parallel; and 4) improve performance

Figure 1. Composition of grid dispatch model currently used for planning in California.

by demonstrating the ability to run a single copy of the model across many nodes, in a massively parallel setting.

Relevance to LLNL Mission

This work directly aligns with the Energy Security and Regional Climate Change Impacts pillar of the LLNL Institutional Science and Technology Five-year Roadmap to the Future. It also supports the growing Livermore Valley Open Campus initiative, specifically the intended high-performance computing center. The successful completion of this project will also support the proposed Partnership for 21st Century Energy Systems between LLNL and the utilities in the state of California.

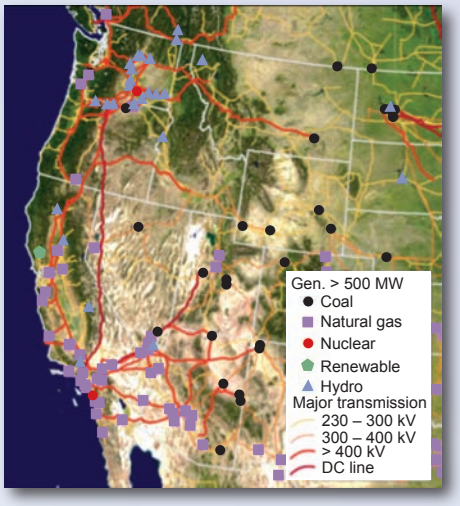

Figure 2. Structure of power grid in the western United States.

Figure 3. Hyperion cluster at LLNL, a high-performance computing testbed.

FY2010 Accomplishments and Results

We accomplished our first milestone of identifying the computational bottleneck in the planning model. We were able to determine that the vast majority of the time is spent solving a daily unit commitment model, which is formulated as a mixed integer linear program by the front-end energy modeling software, and solved by the back-end optimization engine. Formulation of the problem itself, inputs, and outputs are computationally trivial compared to the length of time necessary to solve this unit commitment problem for every day.

We were able to identify a number of improvements to the original problem formulation (our second milestone), primarily concerning the representation of certain generator dispatch constraints. These improvements enabled the unit commitment model to be solved nearly four times faster than before.

Next, we demonstrated that the front-end software could be successfully run on our supercomputers, using the Hyperion testbed (Fig. 3). This included porting the software package (a .NET executable natively run in Windows) to Linux, and scripting the software calls to function in this environment. Our third milestone was completed via the implementation of a parallel job launching capability, whereby many copies of the software could be executed simultaneously on different nodes of Hyperion. On a yearly timeframe, this parallelism alone caused the model to solve an additional three times faster than before.

Altogether, we have thus demonstrated a 12× speedup in the original planning model via the use of our supercomputing resources (see Table). Our fourth milestone, which is to more fully leverage these resources by implementing the model in a massively parallel framework, is ongoing work in conjunction with the creators of the underlying optimization engine.

Sources and degrees of improvement in solution times of the grid dispatch model.

Source of speedup	Degree of speedup
Reformulation of the mixed integer programming model	4x
Parallel execution over months in the year	3x
Massively parallel implementation of underlying algorithms	Not yet determined
TOTAL	**12x (so far)**

Related References

1. Crainic, T., B. Le Cun, and C. Roucairol, "Parallel Branch-and-Bound Algorithms," Parallel Combinatorial Optimization, Chapter 1, E. Talbi, Ed., John Wiley & Sons, New Jersey, 2006.
2. DeMeo, E., G. Jordan, C. Kalich, J. King, M. Milligan, C. Murley, B. Oakleaf, and M. Schuerger, "Accommodating Wind's Natural Behavior," *IEEE Power and Energy Magazine,* pp. 59–67, November/December, 2007.
3. Lamont, A., "Assessing the Long-Term System Value of Intermittent Electric Generation Technologies," *Energy Economics,* **30**, pp. 1208–1231, 2008.
4. Phillips, C., J. Eckstein, and W. Hart, "Massively Parallel Mixed-Integer Programming: Algorithms and Applications," Parallel Processing for Scientific Computing, Chapter 17, M. Heroux, P. Raghavan, and H. Simon, Eds., SIAM, Philadelphia, Pennsylvania, 2006.

FY2011 Proposed Work

We will continue leveraging our supercomputing resources by attempting to implement the grid planning model using MPI distributed-memory parallelism. Additionally we plan on engaging the model's stakeholders directly, by supporting their production runs using the existing framework from FY2010.

Energy Manipulation

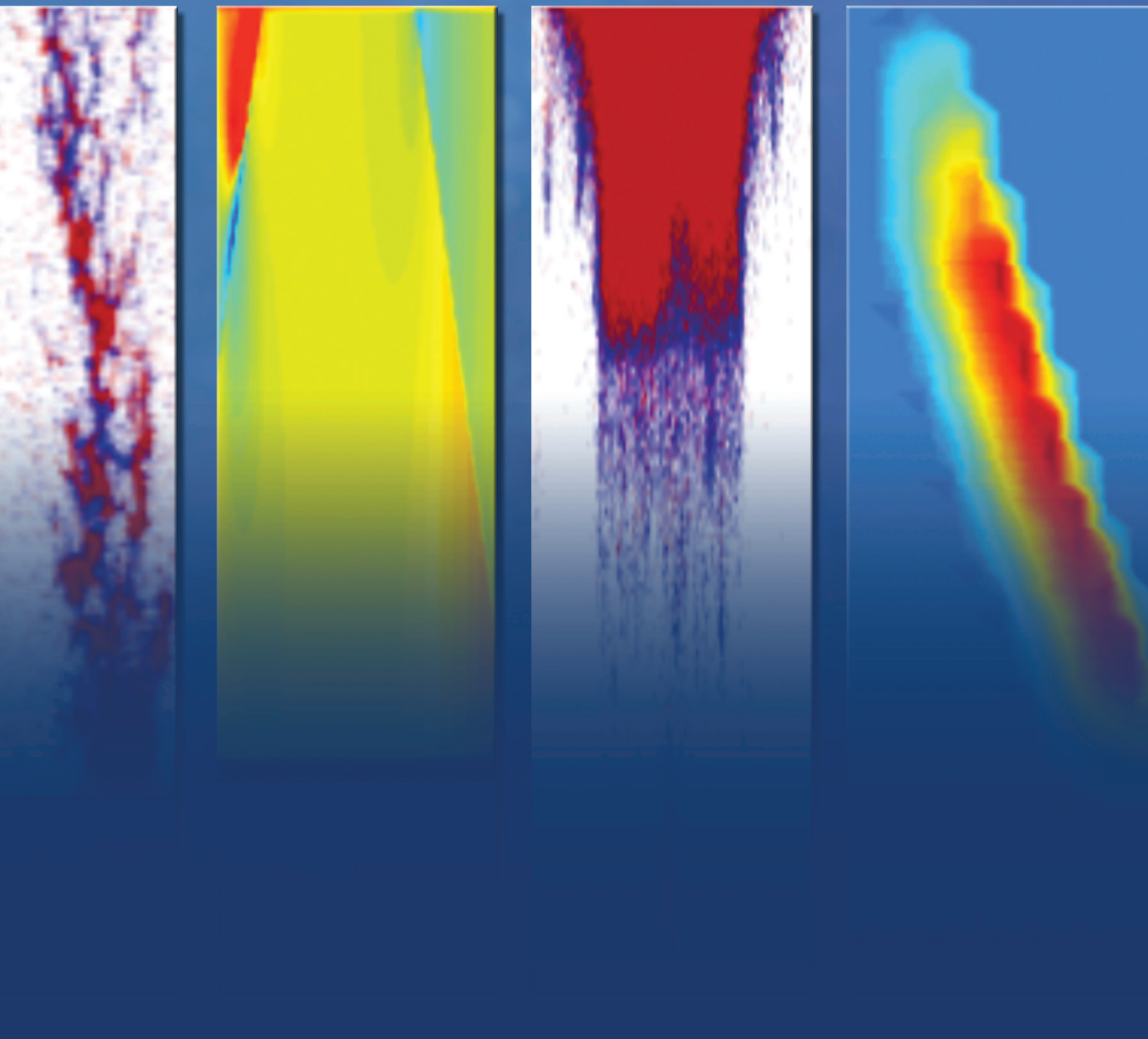

High Voltage Vacuum Insulator Flashover

For more information contact:

Timothy L. Houck
(925) 423-7905
houck1@llnl.gov

High-performance pulsed-power systems are used in numerous applications related to national security. The vacuum insulator is a critical component of such systems, often limiting peak performance. If designed incorrectly the insulator can be the weak link, leading to failure of the entire system. Scientific knowledge developed from simple experiments provides understanding of important physics involved in insulator performance, but is not readily transformed into a reliable tool for predicting operational performance. We are developing a computer model of electrical breakdown at the dielectric/vacuum interface. We are leveraging LLNL's advances in computational resources to bridge the gap between knowledge and application.

Project Goals

We wish to produce a computational methodology for designing high-voltage vacuum insulators for pulsed-power devices. We have demonstrated during this project that a few basic physics phenomena can explain the initiation of electrical breakdown across the dielectric/vacuum interface, known as vacuum insulator flashover. Varying the geometry, materials, and environment used in simulations shows how the different initiation mechanisms evolve. This tool will make it possible to study complex insulator designs in realistic operational conditions and to predict performance. We have proposed insulator designs and processing for the next generation of magnetic flux-compression generators.

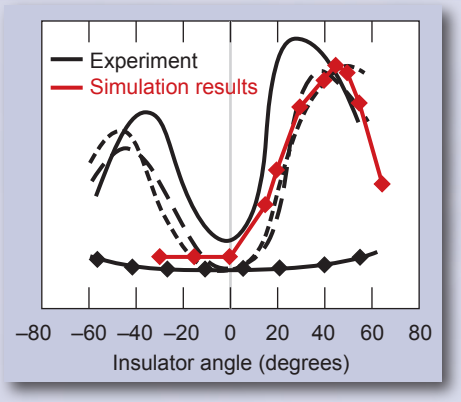

Figure 1. Comparison of empirical data with simulations. Vertical axis reflects ability to withstand flashover, either field strength or time to fail.

Relevance to LLNL Mission

This project directly supports the Energy Manipulation pillar of the Science, Technology, and Engineering foundation. Our computational model enhances LLNL's status as a world-class center for high-voltage vacuum insulator design, development, and testing. Improved vacuum insulators will have immediate impact on explosively driven flux compressors and compact accelerator designs.

FY2010 Accomplishments and Results

In FY2009 we concentrated on improving the algorithms related to the field and secondary electron emission models in the commercial Particle-In-Cell code, Vorpal. The prevailing theories assumed that an avalanche of electrons created from a few seed electrons impacting the insulator surface, causing additional (secondary) electron emission, was the initiating event for flashover. As we refined our model and ran more simulations, we discovered that the secondary electrons were not sufficient by themselves to cause flashover and, in the case of positive angled insulators, did not return to the surface. We submitted a Record of Invention (ROI), IL-12057, related to an insulator design and changed the protocol for insulator testing using knowledge that came from these studies.

In FY2010 we added a gas layer on the insulator surface to the simulations. The light or flash seen during the electrical breakdown of a vacuum insulator that led to the phrase "flashover" is due to the ionization of gas near the surface of the insulator. Whether this gas ionization was important to the initiation of breakdown or simply a result of the breakdown had not been determined. Our initial model used a static gas to simplify computations. Published data from insulator experiments provided an idea of the gas layer thickness while Paschen's Curve provided information on the gas density.

Our next step was to improve the gas collision algorithms used in the code. This involved adding elastic and inelastic scatterings to the ionization collision algorithm. We were then able to do simulations that mimic flashover behavior noted for positive angle insulators (Fig. 1).

Figure 2 depicts the orientation and particle orbits for two of the simulations. The positive angle orientation was expected to be the most difficult to model as the orientation of the electric field prevented secondary electrons from returning to the insulator in a true vacuum situation. However, a combination of electron scattering from gas molecules and electrodes, surface charging, and geometrical field enhancement led to localized electric fields near the surface that favored an electron avalanche or flashover. The angle-independent, fast flashover behavior for negative angles indicated that we needed a better gas model than the static layer that we imposed on the surface.

Our finishing work on the project was developing a dynamic gas where electron impact led to desorption of a neutral gas. Figure 3 illustrates the new gas model.

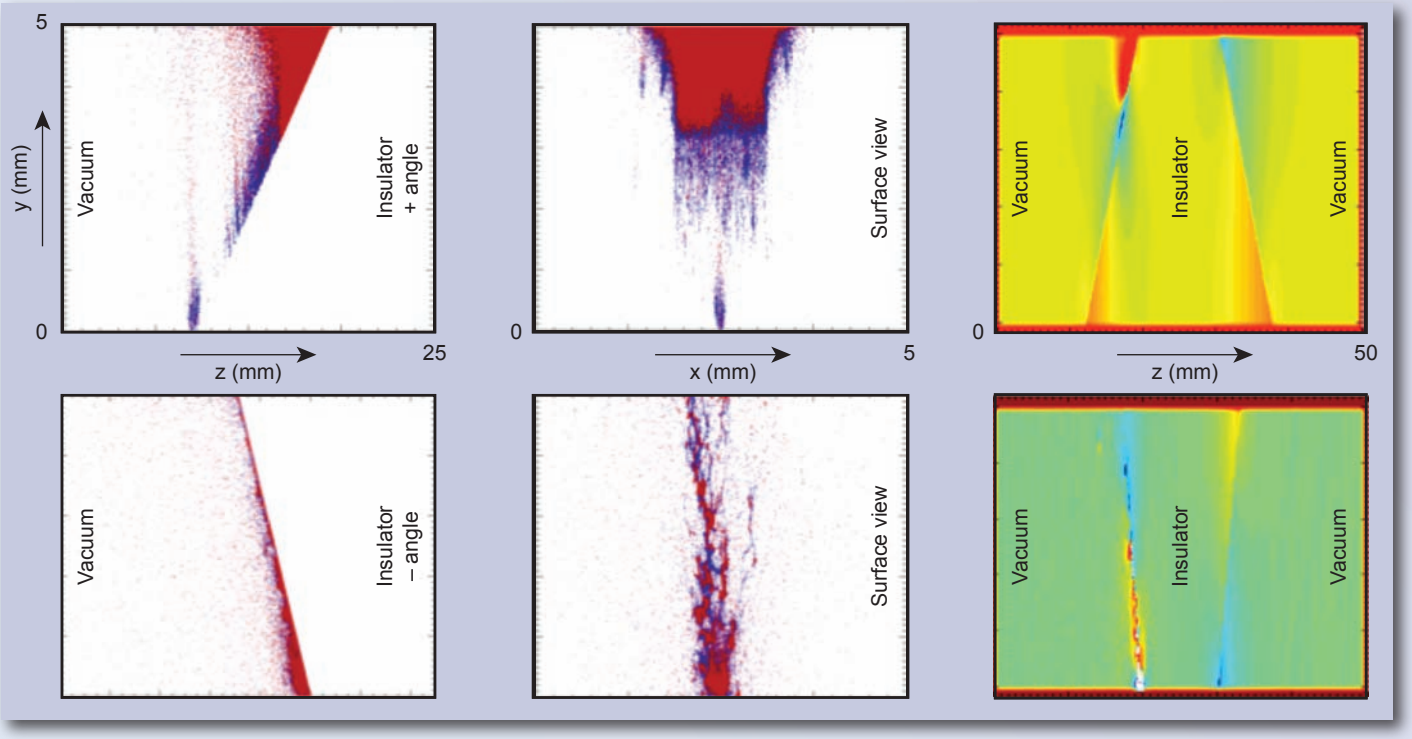

Figure 2. Simulation results for positive 55° (top) and negative 30° (bottom) angle insulators. The red dots represent ionized gas and the blue are electrons. The two views are looking across (left) and directly at (right) the insulator surface. The graph on right is a color contour of the electric field magnitude (red is low and blue is high). The anode is at the top and the cathode is the bottom for each plot.

The understanding we gained on the effect of a gas layer on flashover led to another ROI, IL-12236, related to processing the insulator to avoid gas desorption. We anticipate this work to continue with programmatic support.

Related References

1. Tang, J., *et al.,* "Process of Surface Flashover in Vacuum Under Nanosecond Pulse," *IEEE Trans. Plasma Sci.,* **38**, 1, January 2010.
2. Baglin, V., N. Hilleret, *et al.,* "The Secondary Electron Yield of Technical Materials and Its Variation With Surface Treatments," *Proceedings European Particle Accelerator Conference*, Austria, pp. 217–221, June 26–30, 2000.
3. Perkins, M. P., T. L. Houck, A. R. Marquez, and G. E. Vogtlin, "FDTD-PIC Modeling for Initiation of Vacuum Insulator Flashover," *37th IEEE International Conference on Plasma Science,* Norfolk, Virginia, 2010.
4. Anderson, R. A., "Anode-initiated Surface Flashover," *Conf. Electr. Insul. Dielec. Phen.,* pp. 173–179, 1979.
5. Perkins, M. P., T. L. Houck, A. R. Marquez, and G. E. Vogtlin, "Simulations for Initiation of Vacuum Insulator Flashover," *29th IEEE International Power Modulator and High Voltage Conference,* Atlanta, Georgia, 2010.

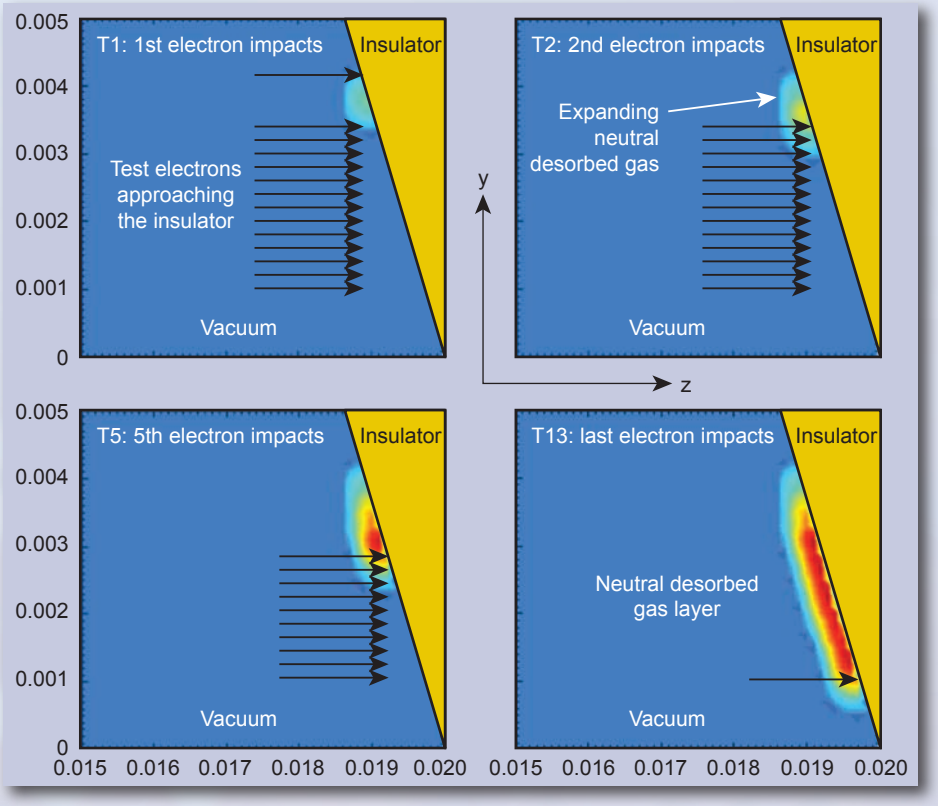

Figure 3. Simulation testing gas desorption model due to electron impact. A group of electrons enters from the left and strikes angled insulator surface.

Author Index

Manuscript Date April 2011
Distribution Category UC-42

Available from
National Technical Information Service
5285 Port Royal Road
Springfield, VA 22161

Or online at *www-eng.llnl.gov/pubs.html*

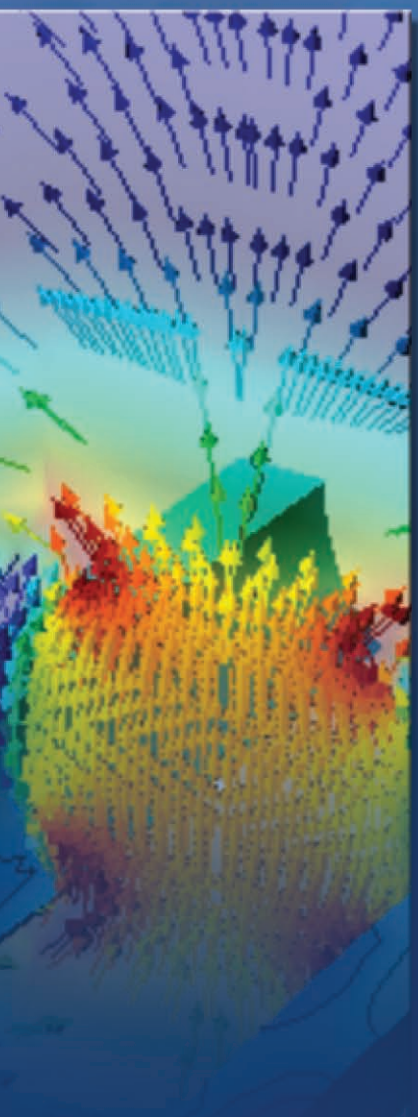

ENGINEERING

Lawrence Livermore National Laboratory

PO Box 808, L-151
Livermore, CA 94551-0808
http:www-eng.llnl.gov/